The Pennsylvania State University

The Graduate School

CEREBROSPINAL FLUID AND BRAIN TISSUE SEGMENTATION

IN HYDROCEPHALIC PATIENTS VIA THREE DIMENSIONAL

LEVEL SET METHOD

A Thesis in

Aerospace Engineering

by

Zeljko Raic

Submitted in Partial Fulfillment

of the Requirements

for the Degree of

Master of Science

December 2013

The thesis of Zeljko Raic was reviewed and approved* by the following:

Jacob W. Langelaan
Associate Professor of Aerospace Engineering
Thesis Advisor

Steven J. Schiff
Professor of Neurosurgery
Director of Penn State Center for Neural Engineering

George A. Lesieutre
Professor of Aerospace Engineering
Head of the Department of Aerospace Engineering

*Signatures are on file in the Graduate School.

Abstract

Volume segmentation of medical image data shows great promise in assisting physicians with diagnosis and treatment. This thesis applies an automated level set method in 3D for segmenting cerebrospinal fluid and brain tissue regions from CT scans of hydrocephalic patients. The level set algorithm used in this work is based on central voxel intensity of source data and mean curvature of the interface. Parameters of the level set equation are determined based on target region properties from CT scans and the algorithm is initialized using a signed distance transform with the standard Euclidean metric. We use the forward Euler method with upwind differencing to propagate the solution forward in time which combined with an imposed stability condition guarantees convergence. The segmentation results show less than 1% error in cerebrospinal fluid volume and 1.5% in brain tissue volume in comparison to those obtained via stereo investigator. Robustness of the level set method is evaluated by a sensitivity analysis of two initialization parameters which shows a linear relationship between the perturbation and error.

Table of Contents

List of Figures

List of Tables

Acknowledgments

There are two people whom I can never thank enough for all my successes and for all my future accomplishments that await. They are my mother and my father. They are responsible for the person I am today and I owe them everything for inspiring me, supporting me and allowing me to make my own decisions - though they were not always the right ones.

I could not have asked for a better advisor than Jack Langelaan. He is an excellent professor, a great mentor and the only person I know who can make explaining difficult concepts seem like a child's play. Thank you Jack for all your help, patience and understanding, without which this work would not have been completed. I would also like to thank Dr. Steven Schiff for his guidance and assisting with the development of this thesis. Thank you for all your insight Dr. Schiff. Every time I left one of our meetings, I did so having learned something new and valuable.

I would also like to thank my AVIA labmates: Nathan T. Depenbusch, Anjan Chakrabarty, Nick Grande, John Bird, Sean Marlow, Shawn Daugherty, Kwok Cheng, Dmitriy Makovkin and Ben Truskin. These individuals have helped me finish this work in countless ways over the last two years. I am grateful to you all for offering your support, providing feedback, engaging me in intellectual discussions and mainly for putting up with me because I know how difficult of a person I can be at times. Not only were they great labmates, they became great friends of mine. Nick, though you became my archenemy in jest, I never had the chance to really tell you how much I respect you and your viewpoints.

Dedication

This is for my mother, father and brother who have taught me to never give up, encouraged me when I've struggled and continue to love me unconditionally despite my many flaws.

Chapter 1

Introduction

1.1 Introduction

This thesis applies an automated level set method for segmenting medical images based on central voxel intensity of source data and mean curvature of the *interface*, i.e. the zero level set. The work focuses on segmenting Computed Tomography (CT) scan regions in hydrocephalus brain. Results are provided as well as a Graphical User Interface (GUI) platform. The motivation is to provide an accurate, automated and computationally efficient algorithm to assist physicians in the diagnosis and treatment of hydrocephalus brain. In principle no modification to the medical images is required, e.g. file type reformatting, data type casting, etc, and the algorithm presented herein may be easily reproduced and verified.

Traditionally a manual slice by slice process, brain segmentation, has benefited from advancements in computing hardware over the last two decades [1]. This has allowed for an automation that produces accurate results while alleviating undue pressure from this task. Proposed 3D brain segmentation algorithms therefore have to account for robustness, accuracy, computational efficiency as well as include an interactive, user-friendly GUI [1].

Current methods for representing 3D objects rely on use of voxels or a wireframe mesh. Difficulties linked with using voxels include low-level representation of surfaces and computational impediments associated with estimating voxels for concave objects [1]. Mesh representations on the other hand require assumptions concerning discretization and the topology of objects [1].

While various techniques currently exist for segmenting 2D images, there are many benefits to having an accurate algorithm capable of segmenting objects in 3D. These benefits include the ability to derive topological features including but not limited to edge tracking of non-contiguous regions within the brain, e.g. abnormal accumulation of cerebrospinal fluid (CSF), as well as provide important clues necessary for accurate diagnosis-clues which are inherently spatial-temporal. Segmenting 3D surfaces instead of contoured areas also provides the added benefit of volume visualization.

A classic example of CSF present in the brain is given in Figure 1.1 on page 3. The image shows a 2D CT brain slice of a ten month old hydrocephalic female. It is clearly visible that CSF areas occupy non-contiguous concave regions. These areas are normally difficult to segment by conventional algorithms due to splitting of topologies when considered in higher dimension, i.e. 3D. The desired result of the segmentation is to accurately identify the areas that are brain and areas that are CSF.

This thesis will:

- Apply the level set method for an accurate, automated and computationally efficient segmentation of medical images. In this application, CT scans of hydrocephalus brain are used and areas of brain and CSF are segmented in both 2D and 3D.

- Develop an algorithm for computing volume and surface area of segmented regions in 2D and 3D. These calculations will be compared against a ground truth data set that has been thoroughly vetted.

- Develop a robust, user-friendly GUI that maximizes automation thus allowing individuals with minimum training to successfully perform segmentation while achieving high level of accuracy. This process will remove the human inaccuracies induced due to fatigue and data overload.

(a) Original Scan

(b) CSF Segmentation

(c) Original Scan

(d) Brain Segmentation
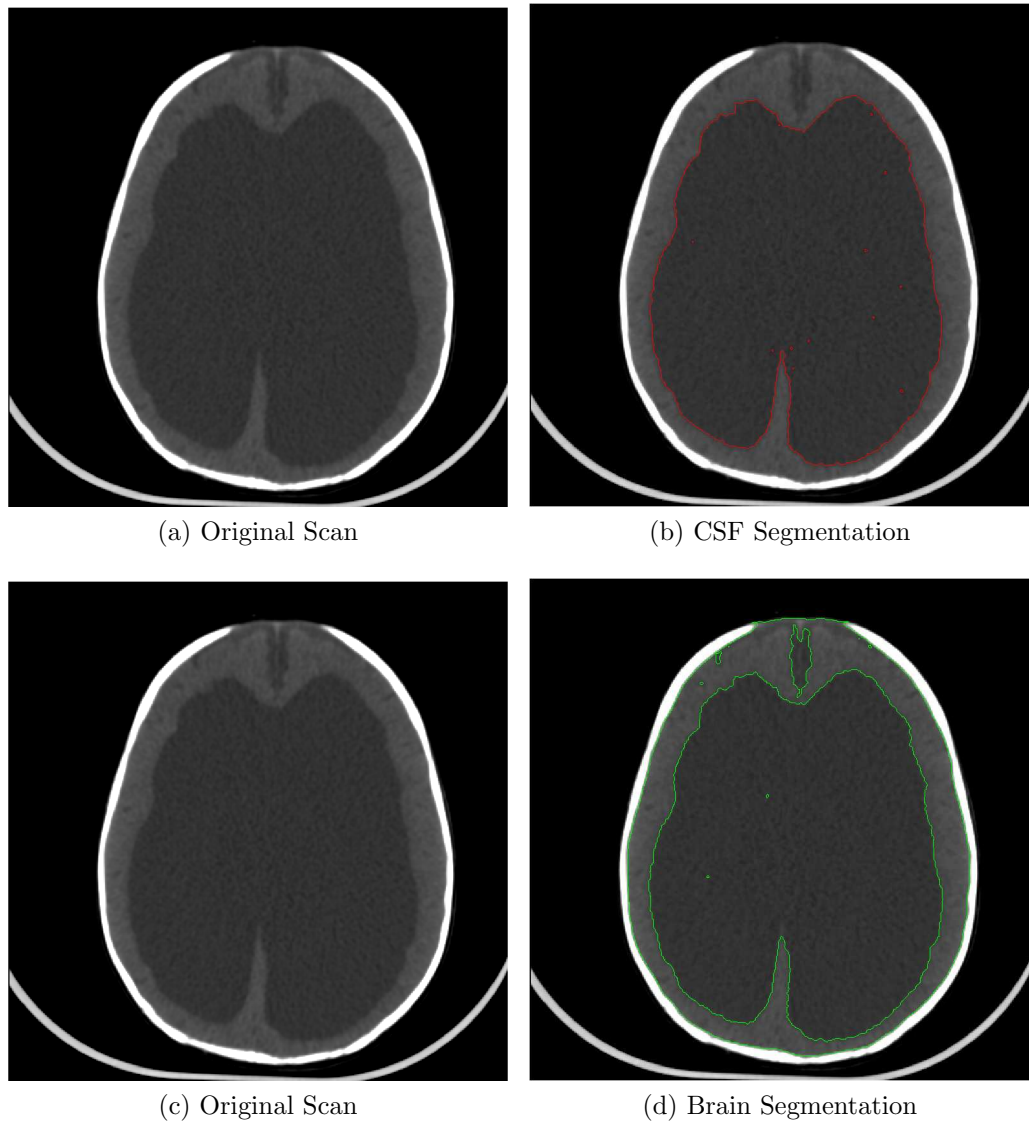
Figure 1.1: 2D CT scan of hydrocephalic brain with non-contiguous CSF regions. The CSF regions in this scan are outlined with a red line. Let it be noted with respect to completeness that CSF regions exist in this image that do not have a red line as an identifier. The brain tissue in this scan forms one contiguous area and its boundary is identified with green lines.

1.2   Motivation

1.2.1   CT Imaging

Majority of the research that is currently being done is focused towards normal adult Magnetic Resonance Imaging (MRI) scans [2]. Accurate segmentation of CT

scans in medical emergencies remains a vital task since majority of the developing countries do not have access to MRI technology [2]. In fact, MRI equipment is so scarce that even in the largest and fastest developing country, China, the ratio of MRI machines is one per million people, a significant difference from fifty machines per million people in the United States [3]. This trend repeats, when one looks at the distribution and sale of medical devices in general throughout the world. Four fifths of global revenue from medical devices comes from sales in Americas and Europe [4]. Though, complementary techniques, both CT and MRI scans have their own strengths and weaknesses. However, the deciding factor in developing countries is typically the availability and moreover the cost of having an imaging study performed. The national average price for a CT scan in the United States is $1,500 less than a MRI scan of the same body part. The cost difference is one of many benefits of choosing CT instead of MRI scans; several of these key advantages presented in [5] are listed below:

- CT scans are faster than MRI and allow for a quicker diagnosis.

- CT scans are less sensitive to patient motion during the imaging procedure.

- CT scans are more accepted by claustrophobic as well as very heavy patients.

- CT scans allow for a greater level of detail in the evaluation of cortical bone.

- CT scans provide accurate detection of metal foreign bodies.

- CT scans have higher sensitivity in detecting intra-cranial calcifications.

Medical CT images, in particular brain scans, are generally used in detection of bleeding, brain damage, skull fracture and sudden onset hydrocephalus [6]. Patients suffering from any of these symptoms are typically in a dire medical emergency and require fast diagnoses in an emergency setting. Attending physicians who treat hydrocephalus patients require fast and accurate segmentation results.

1.2.2   Hydrocephalus Brain

The term hydrocephalus implies a condition in which the primary symptom is the excessive accumulation of cerebrospinal fluid in the brain - a clear fluid that surrounds the brain and the spinal cord [7]. This excessive build up of CSF and the

subsequent blockage of its outflow in the ventricles and the subarachnoid spaces leads to an abnormal widening of ventricles which creates harmful pressure inside the skull while displacing brain tissue regions. Generally caused from head trauma, from congenital defects, from an overproduction or an impaired CSF flow, hydrocephalus brain condition places negative strain on the patient and can have detrimental long term impacts on physiological and psychological development. Learning disabilities are all too common in younger patients who develop hydrocephalus, especially in patients whose condition is congenital in nature. "Hydrocephalus is accompanied by pathological changes in brain morphology, including thinning of the cortex, increases in water content, and loss of myelin in the periventricular white matter"[8]. Disruptions in myelin with reductions in thickness of the cortical mantle, decreased brain mass and thinning of the posterior brain regions are among long-term consequences of hydrocephalus [9]. The effects of excessive CSF accumulation lead to motion and visual problems, short-term memory loss, loss of motor functions as well as lead to higher risk of developing epilepsy. Children suffering from congenital hydrocephalus or hydrocephalus induced from other medical conditions are at higher risk of developmental problems than adults with hydrocephalus. Young children, particularly infants, are better suited to deal with increased CSF buildup and subsequent widening of the ventricles than adults because the fibrous joints remain separated. Currently, physicians evaluating hydrocephalus focus their efforts and studies on the size of ventricles; however, their goal remains on treatment that would allow for healthy brain development [8]. The most common form of treatment for hydrocephalus involves the surgical placement of a cerebral shunt system that diverts the flow of CSF from the central nervous system so that it may be drained into other body cavities where it can be reabsorbed [7]. Clinical studies have shown that brain volume is more directly related to cognitive function than fluid volume in both hydrocephalic mice and young children [10] Accurately estimating brain volume is key in managing hydrocephalus and ultimately remains a vital quantity in the determining a proper treatment that would allow for normal brain development [8]. Singer et al. have shown that diagnostic CSF removal in patients has favorable and immediate volumetric changes of global brain tissue [11]. The report also presents a direct relationship between CSF removal and change in brain volume - change in volume that combined with

proper rehab would allow patients to overcome developmental problems. Patients with hydrocephalus and their loved ones tend to focus on the improvement in the quality of life as a measure of success in the management of hydrocephalus [12] [8]. Current research is beginning to focus on the importance of brain volume in establishing the optimal treatment and the role it plays in determining improvement in neurocognitive performance. In this thesis we use five CT data sets from five different hydrocephalic children with myelomeningocele.

1.2.3   Medical Image Segmentation in 3D

Segmentation of anatomical objects is a vital task in the analysis of medical images. At present, manual, two-dimensional segmentation continues to be the limiting factor for emergency diagnoses because accurate, automated and robust segmentation of three dimensional images remains a widely unsolved task [13] [14]. Furthermore, segmenting images in 3D, slice-by-slice, using 2D techniques is a laborious process and requires manual post-processing to connect the 2D images into a continuous surface. This reconstruction process often leads to inconsistencies which can be mitigated via a true 3D segmentation method that is more robust and ensures a globally smooth and coherent surface between slices [15]. Medical CT scans are typically processed two-dimensionally since they are obtained as a series of two-dimensional slices, or scans, of an organ or a region in the body. Reorganizing and segmenting the slices in 3D will enable for a practical visualization, localized pathology, diagnosis and treatment of anatomical objects [16] [14]. Furthermore the added benefit of segmenting in 3D allows physicians to diagnose and treat anatomical structures by interacting with them via visualization that is achievable through post segmentation reconstruction. Automated 3D, or volume, segmentation plays a significant role by facilitating extraction of anatomical or pathological structures and other regions of interest [17] [18]. Algorithms that operate on volumetric data provide a more complete and accurate segmentation than 2D based segmentation algorithms because volume segmentation accounts for splitting topologies and loculated CSF regions. Also, true 2D segmentation algorithms are limited to the information on the particular slice they operate on, i.e. no information is used from the slices directly above and below thus limiting the

algorithm's ability to segment the desired area. Volume based segmentation algorithms operate on voxels of data from which more information may be extracted due to the higher dimensionality. In this thesis we utilize scalar image intensity data obtained via 2-D CT scans of hydrocephalic patients.

1.2.4   The Level Set Method

Medical image segmentation based on the level set method has been extensively applied to visualization of 3-D anatomical features and boundary tracking of highly convex object surfaces. Examples of these segmentations include: aortic thrombus from abdominal and thoracic scans by Nakhjavanlo *et al.* in [19], brain tumor and tissue segmentation by Chen in [20], carotid arteries by Ukawatta *et al.* in [21] and countless others. A partial differential equation method, forming a subset of active contour models or geometric deformable models, the level set algorithm has been shown to efficiently solve the problem of volume segmentation in an implicit manner. Deformable models create a compromise between the constraints and the shape provided by the input data which resembles a Bayesian approach to image analysis [22]. The level set does not require any pre-processing nor post-processing, a hindrance of low-level segmentation methods that comprise pixel-based clustering, region growing, thresholding, and filter-based edge detection [15]. Additionally, these low-level techniques can make incorrect assumptions and generate infeasible boundaries by only considering local information [23]. Region based segmentation methods resulting in low quality pixel or voxel representations detract from a detailed analysis and visualization of the finished segmentation [24]. Parametric deformable models that are limited by topological adaptation as well as differences in the initial model's and the desired object's boundaries became obsolete with the introduction of level set method in 1988 [15]. The level set deformable models have the following advantages over parametric models in general and make them the ideal algorithm of choice for segmenting CSF and brain tissue regions in hydrocephalic patients:

- Ability to account for topological changes such as splitting and merging of complex surfaces.

- Performing stable numerical computations on a Cartesian grid without having to parametrize the surface contours.

- Very straightforward extension of the 2-D problem formulation to n-D.

To elucidate the first two bullet points, we note that the level set formulation that is presented in this thesis is written in an Eulerian frame, i.e. we fix the coordinate system in the physical domain. This method of describing the front propagation allows us the following advantages which in turn guarantee the first two bullet points: Eulerian framework does not require the interface, i.e. the level set to be simply connected, discrete mesh points do not move which avoid stability problems that arise in Lagrangian descriptions [25].

1.3   Problem Description

The problem at hand is composed of two different parts: First, to accurately and efficiently segment out regions of cerebrospinal fluid inside the brain as well as regions that are brain tissue. Second, to calculate the total volume that comprises CSF regions and the volume that corresponds to areas that are brain tissue. This problem is approached in three dimensions and CT scans of hydrocephalic patients were used as test data. It is assumed that no preprocessing of the data is required and that minimal user interaction is needed to initialize the segmentation.

1.3.1   Volume Calculation

Calculating brain and intra-brain CSF volumes resolves to a modest volume computation that takes into account the image properties of the CT scan. The problem becomes one of counting the number of voxels that correspond to a region that is being segmented. This is the last step in the segmentation process.

1.4   Review of Related Work

The applications of three-dimensional image segmentation are practically unlimited and currently constitute a major problem in medical image analysis. Furthermore, critical volume information from these analyses, particularly in medical
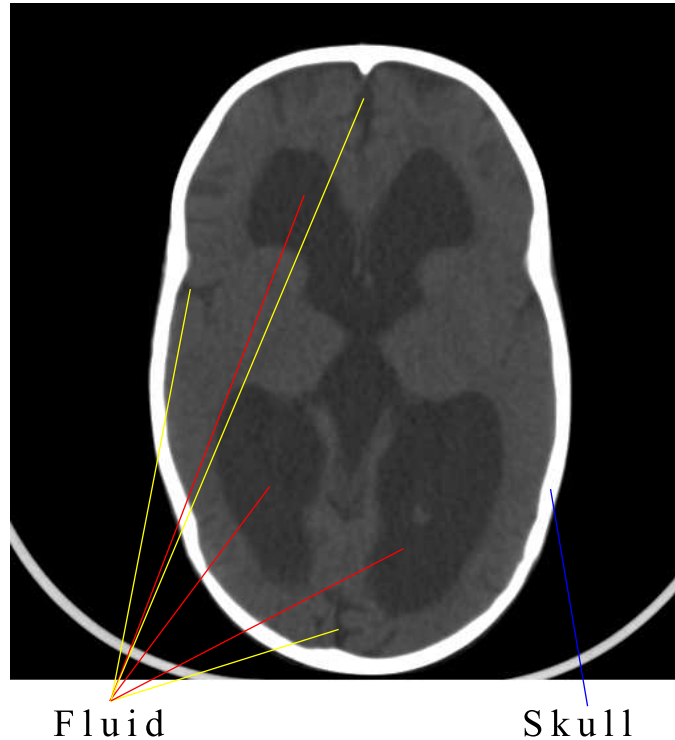
Figure 1.2: The CSF regions identified with yellow lines are considered to not be inside the brain and are not segmented. Only CSF regions that are not in contact with the skull are of interest, i.e. the areas identified with red lines, and are segmented by the algorithm. The skull boundary is identified with a blue line; the boundary, in this scan, is one contiguous region that shows to be white in color.

cases in which patients suffer from hydrocephalus, is vital to physicians in diagnosing and administering proper treatment by virtually interacting with anatomical structures. It is this motivation that drives much of the current research to the development of fast, accurate and robust methods for solving this problem.

1.4.1   Previous Work

In [1] we explored the use of a particle filter, a Bayesian estimator, for segmenting arbitrary subsets of $\Re^3$. The algorithm utilized a Coulomb's inverse-square law as the motion model for propagating particles and the standard Euclidean metric of the gradient vector as the observation which was used to assign particle weights based on the norm. Performance of the method was tested on computer defined

geometries and later on CT data obtained from patients with hydrocephalus. The algorithm showed promise in segmenting computer generated volumes; however, limitations were observed when applied to the CT data. The complex shape of the human brain, e.g. CSF regions and brain tissue regions, presented particles with areas of steep gradients, i.e. high curvature, which induced sample impoverishment and caused unwanted effects from the motion model.

1.4.2 Image Segmentation in 3-D

Modern science has allowed us to non-invasively map the anatomy of human beings through use of CT scans and other imaging modalities [17]. Volume segmentation provides a means of delineating and separating regions of interest that are often obscured during a regular scan due to highly complex internal anatomy. While a myriad of segmentation techniques have been proposed in literature, their use often varies depending on factors such as imaging modality and target region properties. Though no segmentation method can be applied to all types of data, there exist generalized techniques that are suitable for variety of sources. There exist many good papers in literature that provide a thorough overview of segmentation algorithms [17],[26], [27], [28], [29], [30], [31]. In [29] they categorize algorithms in two categories, signal and model based as shown in Figure 1.3. In this section we review algorithms and classify them in the following three categories: structural, stochastic and hybrid methods. Structural techniques rely on extracted information that describes structural properties of the region, stochastic techniques utilize statistical methods without regard to the structure of the region and are applied to discrete voxels, hybrid techniques comprise methods that contain characteristics of both structural and stochastic algorithms.

1.4.2.1 Structural Techniques

Algorithms discussed in this section rely on structural properties of a data set that is to be segmented. The methods that are reviewed are not all-encompassing and only cover generalized techniques.

Edge detection methods aim to delineate regions based on image intensity information. It was introduced as a 2D method by Canny in 1986 in his ground breaking
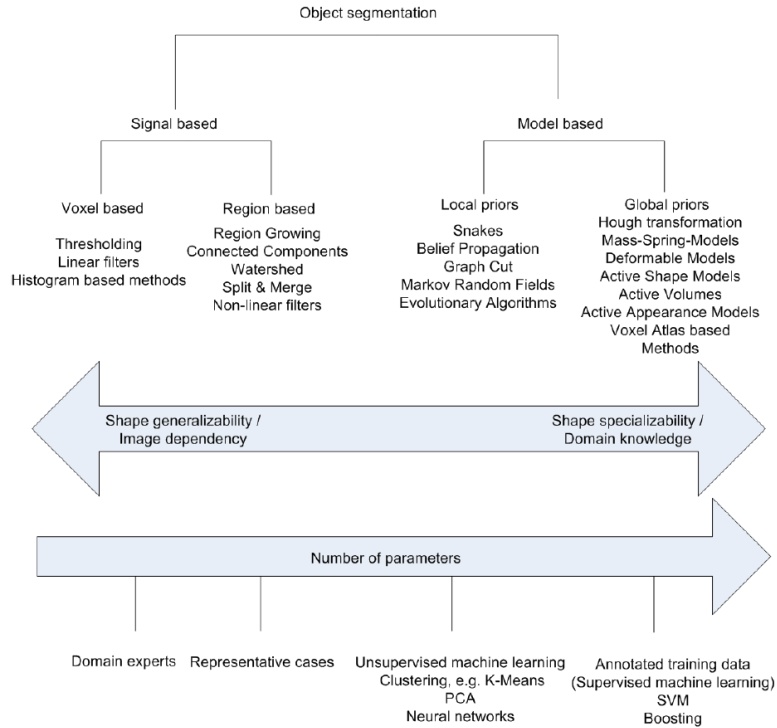
Figure 1.3: An alternative for classifying algorithms based on the amount of shape information used by the segmentation technique.

MS thesis [32]. By classical definition, an edge is detected when a differential operator finds the local maximum of the gradient magnitude. Numerous works have extended this definition to 3D using recursive filters, Sobel operators, surface interpolation [33], [34], [18]. Advantages of such methods include their ability to detect edges perfectly in data sets with contrast variance; however, they are highly susceptible to noise and make it extremely difficult to discern edges based on target regions [17].

Mathematical morphological theory, a branch of nonlinear processing, provides a method for image analysis using set transformations which extract shapes and surfaces via the concept of structuring elements [17]. This method utilizes translation invariant operators such as Minkowski sum, dilation, and its dual, erosion, to extract target regions by treating image data as sets. These techniques remedy the degraded performance of edge detection algorithms in presence of noise as shown in [35], [36], [37]; however, careful implementation and monitoring is needed to prevent undesired segmentation of source data. For example, subsequent applica-

tions of the erosion operator followed by a dilation can introduce holes and high frequencies in the segmentation [17]. These operators, unlike morphological opening and morphological closing, do not posses the property of idempotency which is helpful in establishing a stopping criterion once stability, or a desired segmentation has been reached [28].

Deformable, or active contour, models comprise techniques in which curves, surfaces or solids, defined within the source data domain, deform under internal and external forces. The purpose of the internal force is to maintain a smooth model during the deformation, while external forces drive the segmentation towards the target feature(s) [28]. This method of segmentation gained popularity after its introduction by Terzopoulos in 1988 and remains a widely studied topic as a fundamental tool in computer vision and image processing. In general, these methods can be subdivided into two categories based on their formulation: parametric and geometric. Representation of curves and surfaces is done explicitly in parametric form during deformation by parametric models. This allows for a direct interaction and shortens computational time [38]. This approach however, poses difficulties in the splitting and merging of model topologies which is easily handled via use of geometric deformable models. Geometric methods which are formulated using the theory of curve evolution and the level set method, operate by implicitly defining the model as a subset of a higher-dimensional function. Parametric models can further be subdivided into energy minimizing methods such as snakes and dynamic systems governed by a functional which evolve over time until forces reach an equilibrium. Geometric models, of which level set methods are most well known and studied, have the advantage of separating evolution from the parametrization thus allowing for topology changes to be handled automatically. One of key advantages of deformable models is that segmentation boundaries can achieve sub-pixel, or sub-voxel, accuracy because they are implemented in the continuous domain - a feature that is highly desirable in medical image segmentation. Their hindrance remains that at minimum user specified initial models must be initialized in the source data along with a selection of initial parameters. For further reading on theory, problem formulation and implementation of deformable models see [23], [39], [40] and [38]

1.4.2.2 Stochastic Techniques

Stochastic methods include algorithms that return segmented models based on statistical analysis only as in [41], [42], [43]. We do not include probabilistic deformable models in this category. Stochastic techniques include thresholding, classification and clustering to name a few. Thresholding is the simplest method in image segmentation that partitions an image into sub-regions based on pixel, or voxel, intensity. Binarization, using a single threshold, or multi-thresholding, using multiple thresholds, can be effective in segmenting volumes with high contrast differentials; however, this method is highly sensitive to noise and inhomogeneities. This is especially true when working with CT scans where anatomical objects are displayed with near identical characteristics, i.e. similar Hounsfield unit values [28]. Classifier methods, forming a subset of patter recognition techniques, attempt to partition a feature space obtained from source data using labels, classes, that are established *a priori* [38], [44], [17]. This feature space represents the co-domain of any function of source data. For example, the arbitrary feature function could include voxel intensity or the gradient at the voxel. These methods also require training data that are previously segmented as label references. Key drawbacks of classifiers include their inability to perform spatial modeling and extensive user interaction in acquiring training sets [38]. Unlike classifiers, clustering algorithms comprise unsupervised methods that do not require training data sets. Clustering is a processes by which objects, voxels, are placed together into groups, segmented regions, using desired target region properties. Because training data are not required, clustering algorithms in essence train themselves by iterating between segmenting the volume and characterizing properties of each class [17]. Like classifiers, clustering algorithms do not incorporate spatial modeling. Also, they require an initial segmentation or a set of initialization parameters.

1.4.2.3 Hybrid Techniques

Hybrid techniques include segmentation algorithms that feature properties that belong to both structural and stochastic methods. There exist many algorithms that fall into this category due to numerous attempts to combine desirable traits of two or more segmentation techniques. Two of the best known hybrid methods

include region growing and the split and merge algorithms. Region growing aims to group voxels into larger groups based on target region properties. The algorithm is initialized with a set of starting points, or seed voxels, which are grown by appending neighboring points if they conform to the target region properties [28]. Disadvantages of this method include a manual insertion of seed points, a potential for misleading results if connectivity information is not used properly and sensitivity to noise and partial volume effect which may cause holes and discontinuities in the final segmentation [28]. Region splitting and merging provides an alternative approach to the region growing method. This algorithm modifies the source data by organizing it into a pyramidal grid structure of regions where each region is further subdivided into groups of eight [17]. Successive regions are additionally subdivided into smaller disjoint groups of eight until a homogeneity criterion is satisfied by each region. Furthermore, any eight regions can also be merged together into a single larger region based on predefined criteria, typically by voxel intensity. Split and merge techniques have the benefit of not requiring any seed points; however, they call for organizing source data into pyramidal grids and run the potential of creating adjacent regions with identical properties during the splitting operation.

1.4.3 Segmenting CSF and brain tissue in hydrocephalic patients

Many of the current techniques in image processing were motivated by the needs of the medical community. Vast advances in computing technology have also galvanized the development of complex algorithms that could not have been implemented until the last two decades. The problems concerning delination, visualization and registration of anatomical structures remain at the the forefront of research in medical imaging. Accurately segmenting human anatomy assists physicians in pre-operative planning, diagnosis and treatment selection phases of patient care. In patients with hydrocephalus, quantifying cerebrospinal fluid volume can mean the difference between life and death. Patient responses to current treatments, shunt implants and endoscopic third ventriculostomy, continue to be sub-optimal. In order to compensate for this, improvements in therapy protocols

need to be made by increasing predictive capability of computational models of the mechanics of hydrocephalic brains [45]. Furthermore, brain tissue volume changes over long periods of time in patients with chronic hyrdocephalus can provide insight into quality of life development and long term care requirements. In this section we provide a literature review of brain tissue and CSF segmentation.

1.4.3.1 Cerebrospinal Fluid Segmentation

Segmentation cerebrospinal fluid has important applications in neuro-imaging such as assisting in the analysis of morphological differences and changes due to disease severity and neurological disorders [46]. In [47], Tsunoda et al. investigate the effect of CSF volume measurement in assessing treatment measures of patients with normal pressure hydrocephalus. Segmentation techniques offer tremendous advantages over invasive tests such as intracranial pressure measurement, CSF tap test and RI cisternography. Lack of scientific reporting on accurate measurement of intraventricular and intracranial CSF volume is limiting the understanding of the relationship between ventriculomegaly and clinical outcome. Postoperative analysis of CSF volume changes can provide valuable information in patients with neurodegenerative disorders as shown in Hodel's studies [48], [49]. These measures have become a topic of much study as evidenced in [37], [2], [8], [45]. The importance of quantifying CSF volume is not limited to patients with hydrocephalus; individuals who have suffered strokes or have been diagnosed with neurological diseases such as Alzheimer's stand to benefit as well [50], [51]. Vast literature exists which covers segmenting CSF; we only emphasize such importance in individuals with hydrocephalus and consider particulars of medical research outside of the scope.

1.4.3.2 Brain Tissue Segmentation

The brain is the most complex organ in human anatomy. Brain tissue segmentation is essential in study of disorders like Alzheimer's, [52], and continues to provide us with the understanding of its processes and functionality. Additionally, segmentation can also be utilized as a preprocessing step in applications such as voxel-based morphometry. Detailed reviews of such algorithms is described by Tsang and Gor-

thi in [53] and[54] respectively. Tsang provides a thorough comparison of the two most widely used software packages in the neuroimaging community, SPM5 and version 4 of FMRIB. His analysis uses the latest version of the software, a variety of independent data sets for benchmark testing and most popular metrics in literature. Gorthi contributes with a convergence study of energy minimization methods for Markov Random fields in assessing brain tissue. Continued innovation seeks to improve on the existing techniques by making algorithms more robust, consistent and accurate [9], [55], [56].

1.4.4 3-D Level Set Methods

Motivated by the need to track the motion of a front whose speed depends on local curvature in problems such as crystal growth and flame propagation, the level set method was first introduced by Osher and Sethian in [57] in 1988. This theory expanded on previous work by Sethian in [58], [59] which uses an Eulerian formulation for front propagation. In numerous works since, [60], [61], [62], [63], [64], [65], [66], Sethian and Osher have added to this technique which continues to be one of the most studied areas in image processing. The trivial extension from 2D to 3D has allowed researchers to focus on developing faster, more robust and computationally efficient techniques from the theory of Sethian and Osher without having to devote effort on extending the geometry [67], [68], [69], [70]. The vast literature that exists on level set methods is left for review for the more motivated reader.

1.5 Contributions

The primary contributions of this thesis are described below:

- Accurate three dimensional segmentation of cerebrospinal fluid volume and brain tissue volume in hydrocephalic patients.

- The development of a generalized GUI application that utilizes a three dimensional level set algorithm for segmentation of medical images.

- Performance verification using five ground truth CT data sets of hydrocephalic patients that have been vetted with a stereoscope investigator along with a sensitivity analysis of level set parameters used to initialize the algorithm.

1.6   Reader's Guide

The remainder of this thesis is organized in the following manner:

- **Chapter 2** defines the problem of segmenting medical images in 3-D, specifically cerebrospinal fluid and brain tissue regions in hydrocephalic patients. The five CT data sets used in simulations are also presented.

- **Chapter 3** describes the governing equations of the 3-D level set method along with a justification for its use. Level set parameter selection and a stopping criterion are presented also.

- **Chapter 4** describes the framework, computational platform and the results of the level set simulations. Also presented are results of the sensitivity analysis of the level set parameters along with a comparison of the simulation results with ground truth data obtained via stereoscope investigator.

- **Chapter 5** concludes this work and offers suggestions for future research.

Chapter 2

Medical Image Segmentation

This chapter provides the necessary equations and methods used in developing the problem formulation that is used in this thesis. The generalized problem statement is explained in Section 2.1 and is expanded on mathematically in Section 2.2. Next, the dimensionality of the problem is followed in Section 2.3. The method by which the medical data was obtained is given in Section 2.4. Included is an explanation of the different scales used in viewing the medical images. Particular difficulties associated with the method of collection that were encountered in this thesis are given in Section 2.5. The importance of proper initialization is also explained. This chapter concludes by presenting in Section 2.6 the data sets that are used in this thesis along with a table of properties.

2.1 Problem Statement

The objective of the current research is to make use of intra-brain CSF volume and brain tissue volume data to aid in the diagnosis and treatment of hydrocephalus brain. A 3-D level set algorithm will be used to segment the regions that correspond to intra-brain CSF and brain tissue. This type of segmentation method does not require any pre nor post-processing, is applicable to different image modalities - in this case CT, and is highly automated in that it requires only 3 parameters for initialization.

Thus, the problem at hand is to delineate regions of CSF and brain tissue, in 3-D, given CT scans of hydrocephalic patients taken in 2-D. At the same time, this

segmentation must not identify any anatomical features other than the ones that are desired.

Level Set method involves propagating a zero level set surface through deformation over a moving front that corresponds to the desired features that are to be extracted, e.g. regions of CSF and brain tissue. The nature of the deformations is determined by the problem statement and they often include a forcing function that uses initialization parameters to propagate the zero level set. The premise of the segmentation algorithm and parameter determination is introduced now, but will be discussed in more detail in Chapter 3.

In the context of medical imaging, level set methods assume that properties of scan data are known *a priori* and are critical during the initialization phase of the segmentation. The level set algorithm can then be initiated to trace out desired regions from the scan data.

2.2   Image Segmentation Problem

In this thesis we use the classical definition of image segmentation as a process during which an image is partitioned into non-overlapping, constituent regions which are homogeneous with respect to some characteristic. The ultimate goal is that by locating objects and boundaries, the image representation would be changed to provide an easier way for visualizing and communicating information to the viewer [71]. Pham, Xu and Prince provide a generalized framework for the classical problem of image segmentation in [26], as well as Pal in [27], and we adopt this formulation in this thesis.

Let Ω be the domain of an image to be segmented. The problem that remains is to choose the sets $S_k \subset \Omega$ whose union is the entire image. The sets then clearly must satisfy the following condition:

$$\Omega = \bigcup_{k=1}^{N} S_k \tag{2.1}$$

The sets, S_k, are chosen, or rather segmented, based on distinct anatomical features or pre-determined regions of interest [26]. Each S_k is connected and satisfies the following property $S_k \cap S_j = \emptyset \ for \ k \neq j$. The sets, S_k, however may be

grouped in a manner where they form a subset, U, of Ω themselves such that S_k for $k = 1, 2, 5, 7, 11$ corresponds to a particular anatomical feature. In this case, the subset, U, could represent areas of loculated intra-brain CSF. This assignment of designation to each region is a process known as labeling and is usually a trivial step in medical imaging because it is done by a trained technician or a physician [26]. An example of a partial decomposition of an image into sets is given in Figure 2.1 on page 20. The subset U of Ω that is outlined in red traces out regions that correspond to image features which form a spiral pattern.

In this thesis we emphasize the distinction between segmentation and feature detection. Though the two processes are closely related, the key difference is that feature detection deals with establishing a presence of an image property while segmentation assumes that the property is known *a priori* [18] [72]. Furthermore, segmentation focuses on precisely locating regions of the image that possess the property of interest. Feature detection methods, e.g. edge, texture, make assumptions that are too elementary for identifying anatomical structures in medical imaging. For example assuming that the edge gradient is stronger than noise, that edge direction and edge strength varies slowly along the edge is too simple to accurately detect object boundaries [18].
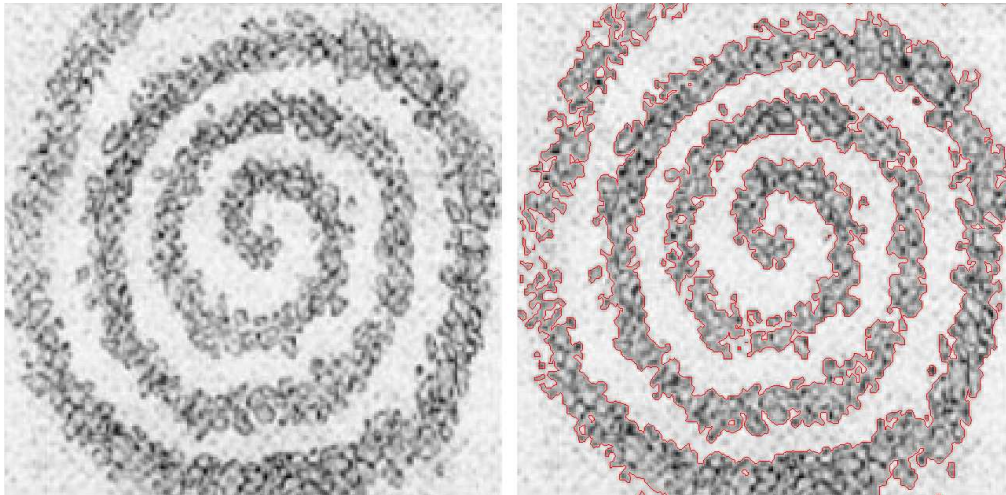

Figure 2.1: The spiral pattern in the image on the left is chosen for segmentation. The red regions, or sets, in the image on the right show the final segmentation of the spiral pattern.

2.3 Dimensionality

The motivation for 3-D medical image segmentation was given in section 1.2.3 and its relation to the problem statement is discussed in this section. The term dimensionality refers to the image domain, 2-D or 3-D, that the segmentation method operates in. While the 3-D level set method incorporates image intensity along with spatial information, i.e. gradient, obtained from the voxel data, segmentation methods that solely utilize intensity information are independent of the image domain [26]. In this thesis we organize 2-D CT scans into a 3-D representation by stacking the scans in a 3-D matrix with respect to the order in which the scans were taken.

2.4 Modality

In this thesis we apply a segmentation algorithm to medical images obtained via X-ray computed tomography procedure. Though the level set method presented in this thesis is applicable to other modalities, e.g. MRI, ultrasound, PET, etc, we specifically focus our efforts on CT scans as motivated in section 1.2.1. While producing images at resolutions equal to or better than MRI, CT scanning also reduces issues inherent to projection radiography techniques [26].

A procedure that combines computer processed X-ray slices to produce tomographic images of anatomical objects, CT scans are well suited for quick examinations of individuals who have suffered internal injuries, for detecting tumors, calcifications, edema and many other underlying conditions. Figure 2.2 on page 23 shows a CT scan of a hydrocephalic patient. The pixel contrast range in the image has been rescaled in order to better visualize the CSF and brain tissue that is present in the image. Pixels in images produced via CT are displayed in terms of relative radiodensity. Radiodensity refers to an object's ability to block the passage of electromagnetic radiation, in this case X-ray, through itself. Pixels are displayed according to the mean attenuation of the tissue; the values ranges from -1024 to $+3071$ on the Hounsfield scale. The Hounsfield unit (HU) scale is a linear transformation, equation 2.2, of the original attenuation coefficient into one where radiodensities of distilled water and air at standard atmospheric conditions,

temperature and pressure, are defined as 0 and -1000 HU respectively [73].

$$HU = 1000 \times \frac{\mu_X - \mu_{water}}{\mu_{water}} \qquad (2.2)$$

Due to the wide dynamic range of the HU scale it is impossible to visualize all of the anatomical features without modifying the grayscale of the image [74]. Suppose a CT scan with a dynamic range of over 2000 HU needs to be compressed to the range of a display device, 0 to 255 for an 8-bit, then the resulting image and its grayscale become so compressed that almost no intensity variation remains. CT scans typically contain normalized units of measurement, contrast or pixel intensities and in order to account for the wide HU range a modified grayscale given in equation 2.3 is used when writing CT scan data to digital image files [74]. In the equation, L and W refer to the display window level and display window width and I_{max} is the maximum intensity of the display device. Figure 2.2 shows the mapping of the original intensity scale between the specified bounds to the full scale of the display device.

$$p_w(x,y) = \begin{cases} 0, & p(x,y) \leq L - \frac{W}{2} \\ \frac{p(x,y) - \left(L - \frac{W}{2}\right)}{W} I_{max}, & L - \frac{W}{2} < p(x,y) \leq L + \frac{W}{2} \\ I_{max}, & p(x,y) > L + \frac{W}{2} \end{cases} \qquad (2.3)$$

When it is desired to convert from this modified grayscale to the HU scale a linear transformation, based on CT machine settings, must be applied to the data to obtain the corresponding HU values. Equation 2.4 on page 22 gives the relationship between the HU and the modified grayscale.

$$HU = m \times R_S + R_I \qquad (2.4)$$

The conversion values R_S and R_I are referred to as *Rescale Slope* and *Rescale Intercept* respectively and are stored as image properties in the digital CT scan.

Table 2.1 on page gives HU values of common anatomical regions of interest (ROI) in CT imaging [73]. These values are approximate and though CT scans generally retain their quality, they are susceptible to degrading artifacts which
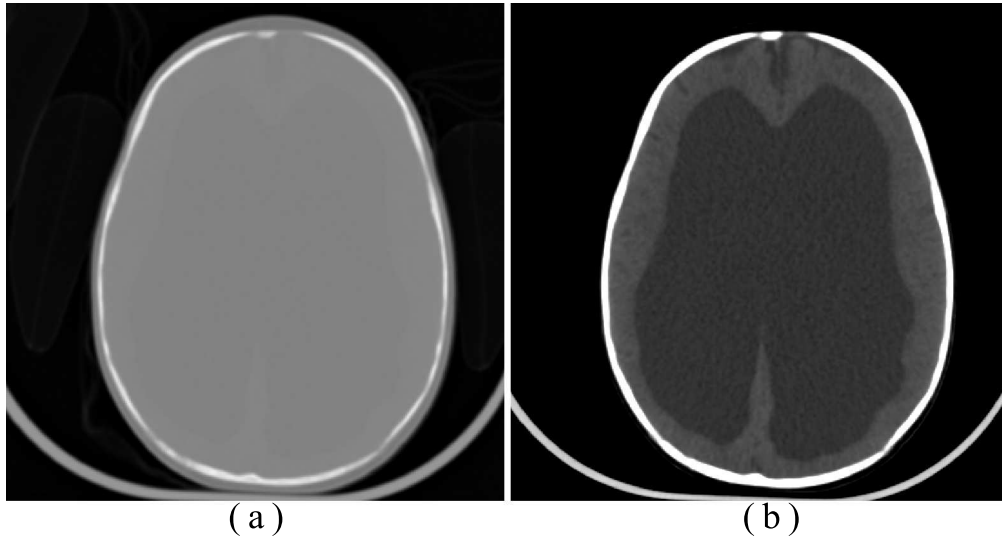
(a)   (b)

Figure 2.2: Mapping from HU scale to modified grayscale. (a) Hydrocephalic brain viewed under the full dynamic range of the image (2030 HU). (b) Hydrocephalic brain shown with a window width, $W = 138$ and window level, $L = 89$.

include shading, beam hardening and partial volume averaging.

Table 2.1: Hounsfield unit value of common organic substances

Substance	Hounsfield Unit
Air	-1000
Fat	$-100 \; to \; -50$
Water	0
CSF	15
Blood	$+30 \; to \; +45$
Grey Matter	$+37 \; to \; +45$
White Matter	$+20 \; to \; +30$
Bone	$> +700$

2.5 Shading Artifact and Partial Volume Effect

In this thesis we emphasize the absence of any pre-processing of CT scans during the segmentation. This section introduces several key artifacts that are often encountered in CT imaging and serves to justify the use of level set algorithm as well as the importance of solving this problem without previously minimizing any induced artifacts. The term *artifact* refers to any systematic discrepancy between the CT HU value in the reconstructed image and the true attenuation coefficient of the object [75]. We include the effects of partial volume averaging (PVA) in this discussion for completeness and recognize that PVA can be a contributing cause of image artifacts rather than an artifact in itself. When compared to conventional radiography, CT images are inherently more prone to artifacts due to the number of independent detector measurements required for reconstruction of an image [74]. The origins of image artifacts are generally based on principles of physics, patient behavior, technological limitations or technological misuse.

Shading artifacts typically occur during scans when materials such as metal or bone, obscure X-rays that are passing through as well as in the neighborhood of objects with high contrast. These artifacts which may present as either bright or dark areas, can cause unpredictable CT HU value shifts that may lead to a misdiagnosis. Figure 2.3 shows an example of an image containing a shading artifact. This CT slice was taken near the base of the skull - an area with bone and soft tissue regions where most shading artifacts occur.

Figure 2.4 on page 26 shows the same CT slice with the full dynamic HU range as well as the modified grayscale, $W = 138 \ L = 89$. As one can see, the shading artifact can not be identified with a naked eye in either of the two images. This is a huge problem that can effectively render an automated segmentation level completely useless.

The recognition and avoidance of artifacts in medical imaging is an extensive and well developed field of research. In this thesis we focus our efforts on minimizing the effects of such artifacts on the segmentation process by clever use of initialization parameters. Because we do not pre-process our image to treat the artifacts we consider any in-depth discussion out of the scope of this study. For further readings see citehsieh, [75], [76], [77].

Shading Artifact

Figure 2.3: Example of a CT scan with shading artifact. The image shown has a window width, $W = 7$ and window level, $L = 35$.S

Partial volume averaging (PVA) or partial volume effect causes CT numbers that are representative of the average attenuation of anatomical features within an image. This occurs when a dense object protrudes into the scanning plane of the CT machine and interferes with oncoming X-ray beams. Due to the divergence of the X-ray beam profile in the normal direction of the scanning plane, the magnitude of PVA becomes angularly dependent with respect to the location of the intrusive

(a)   (b)
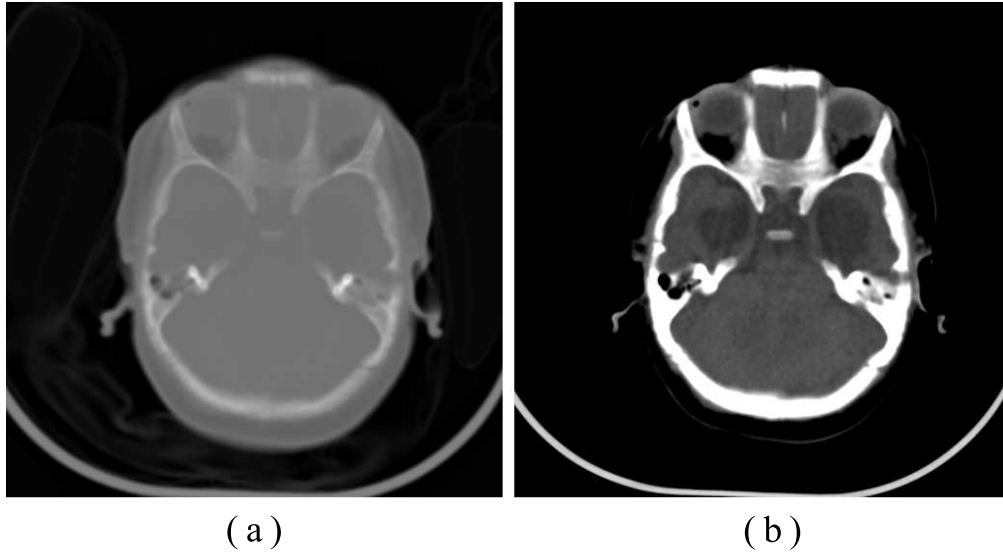
Figure 2.4: Mapping from HU scale to modified grayscale. (a) Hydrocephalic brain viewed under the full dynamic range of the image (2364 HU). (b) Hydrocephalic brain shown with a window width, $W = 138$ and window level, $L = 89$.

object as shown in Figure 2.5 from [74] on page 26. Also, the likelihood of PVA occurring during a scan increases as CT scan slice thickness gets larger [74] [75]. This issue may obviously be mitigated by using a thin acquisition section width; however, doing so increases the presence of photon noise and the radiation dose that the patient is exposed to [74].
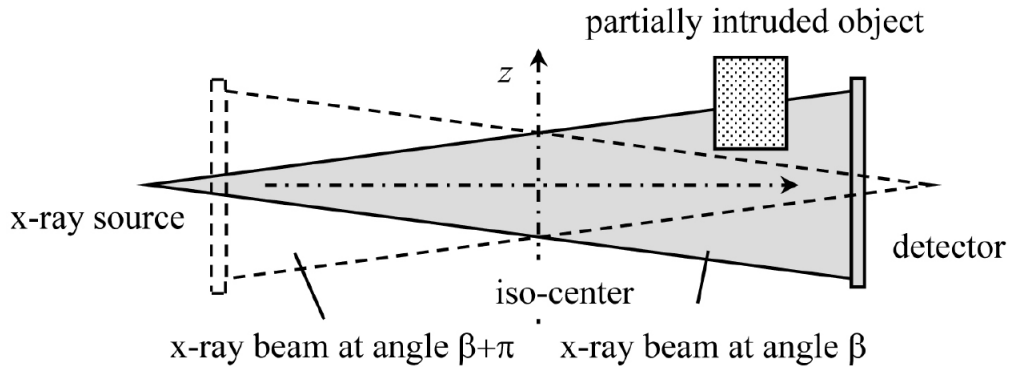
Figure 2.5: Example of cause of partial volume averaging. The projection data set contains inconsistencies due to the object that is located off the iso-center line.

Figure 2.6 on page 27 shows a slice with partial volume averaging of the intra-brain cerebrospinal fluid and the surrounding brain tissue. This example shows

the severity of the problem that can be caused by PVA. Delineating intra-brain CSF regions in this image becomes difficult if not impossible for a computer based segmentation technique without intervention from a human observer.
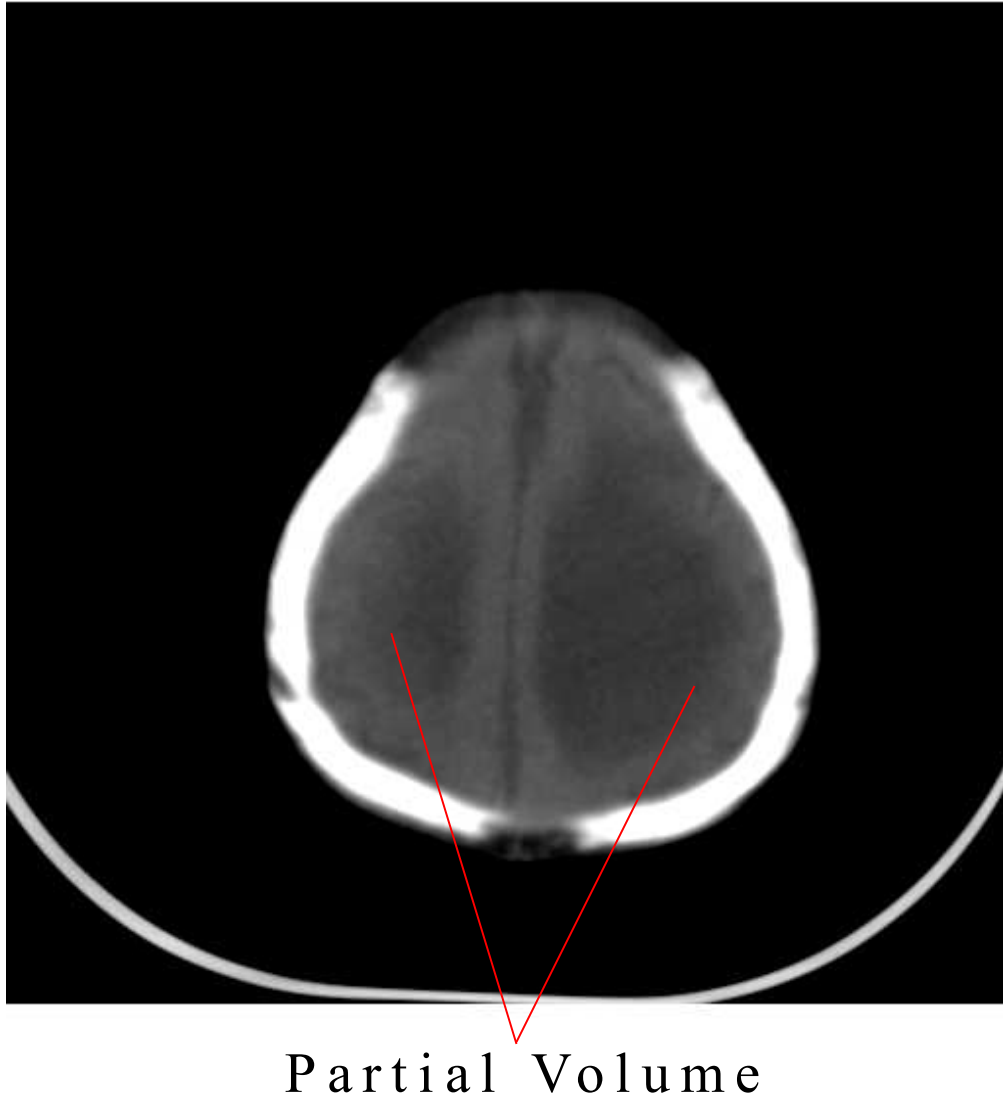

Figure 2.6: Example of partial volume effect in a hydrocephalic brain scan shown with a window width, $W = 138$ and window level, $L = 89$.

2.6   CT Data

The five CT data sets that are used in this thesis have been de-identified and labeled in accordance with the protocols approved by the Institutional Review Board of Penn State University. These de-identifed data sets were provided to us in DICOM format for use in validating the level set segmentation algorithm. In Table 2.2 on page 28 we summarize the properties of the DICOM images. Columns labeled *Resolution* and *Thickness* refer to the dimensions of the CT slices in the horizontal and vertical plane respectively. The column labeled *Pixel Spacing* refers to the dimension of the pixel in the horizontal plane. Uniform *Pixel Spacing* was used during the CT procedure for all of the data sets for purpose of preserving the aspect ratio of the anatomical features. Columns labeled R_I and R_S were discussed in Section 2.4 and their relation to the HU scale is given in Equation 2.4 on page 22.

Table 2.2: CT data set properties

Data Set	Slices	Resolution	Thickness	Pixel Spacing	R_I	R_S
18	20	512x512	8	0.4296875	+1	-1024
19	16	512x512	8	0.3984375	+1	-1024
21	27	512x512	5	0.37109375	+1	-1024
27	25	512x512	5	0.3515625	+1	-1024
28	26	512x512	8	0.359375	+1	-1024

2.7   Level Sets for 2D Segmentation

In this section we will give three simple examples of segmenting objects in 2D. The equations for the 2D level set that are used in this segmentation are presented in A.1 on page 82. Because of the trivial extension from 2D to higher dimensions, the 3D level set equations will be derived in Chapter 3 in full. This section serves

to give the reader a basic overview of how the level set operates from initialization to end using without presenting any of the mathematical foundation.

In the first example, four squares are segmented using the 2D level set. The image in Figure 2.7 was computer generated. We begin the segmentation by initilizing the level set parameters. The regions we choose for segmentation are the four squares in the image. Figure 2.8 shows the initialization mask that was used for the level set. The circular mask was used for simplicity and any arbitrary shape would have sufficed. Figure 2.9 shows the progression of the level set through 1200 iterations from initialization to the complete segmentation. Figure 2.10 shows the completed segmentation of the four squares. This examples forces the algorithm to segment "sharp" corners, or areas that would otherwise be considered points of singularity due to the nature of the derivative at such locations. The level set is able to navigate the "sharp" turns without difficulty.

The second example shows a segmentation of two computer generated circle approximations. This example tests the level set algorithm's ability to delineate between the edge boundary and its surroundings which have been transformed using a standard Gaussian blur filter. The second circle has been created by blurring the edge boundary of the first one. The algorithm's goal is to accurately trace the edge of the original circle within the blurred area. This will test how well the algorithm performs in areas that suffer from partial volume averaging and other image defects. Figure 2.11a on page 34 show the original computer generated circle as well as a copy of the circle with a Gaussian blur filter applied to its edges. The finished segmentation shows that the level set algorithm was able to accurately trace out the edge of the circle that was concealed under a Gaussian blur. This example is replicated in 3D in Chapter 3.

In the last example, we present a segmentation of a normal mouse brain. The mouse brain data was provided courtesy of Dr. Steven Schiff, Director of Penn State Center for Neural Engineering. The original data was provided as a bitmap image file sized 256x320. The data was modified by padding the horizontal dimension with rows of zeros so that each image would be 320x320 pixels in size. This was done in order to simplify the level set algorithm and the vectorized code that was designed to operate on "square" matrices. The mouse data contained 90 CT slices, each 0.20 millimeters in thickness. The slices are numbered in ascending
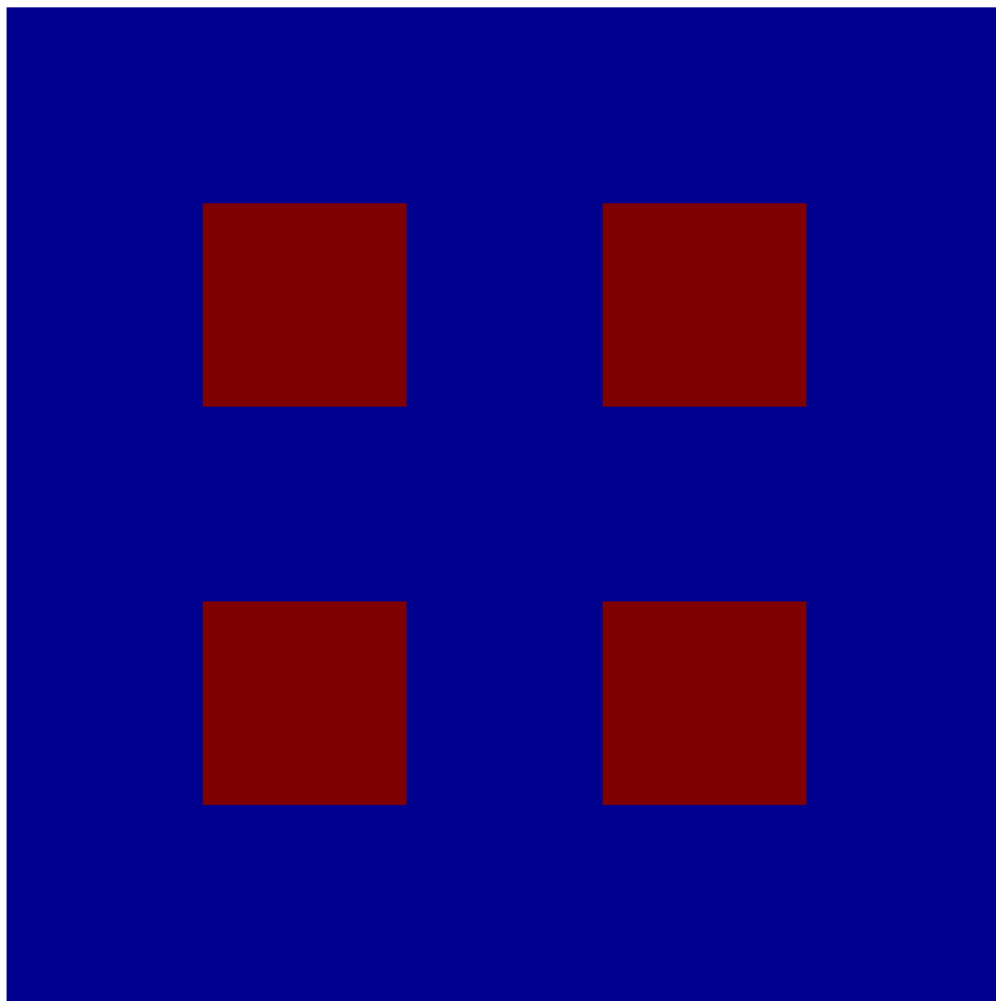
Figure 2.7: Example of a simple geometrical feature to be segmented in 2D. The image is 250x250 pixels and each square is 50x50 pixels.

order with the first slice starting at the base of the skull. Figures 2.12 on page 34 and 3.4 on page 41 correspond to the 28th and 40th slice respectively and show the segmentation results with a side-by-side comparison of the original image on the left. In this example we test the algorithm's ability to trace out complex geometries and its general capability of segmenting near human like brain anatomy. In figure 3.4 the scan shows regions of the brain that contain several loculated CSF regions within the brain tissue.

These three examples show the capabilities of the level set in 2D and the degree of accuracy of the finished segmentations. The 2D algorithm was also used to tune
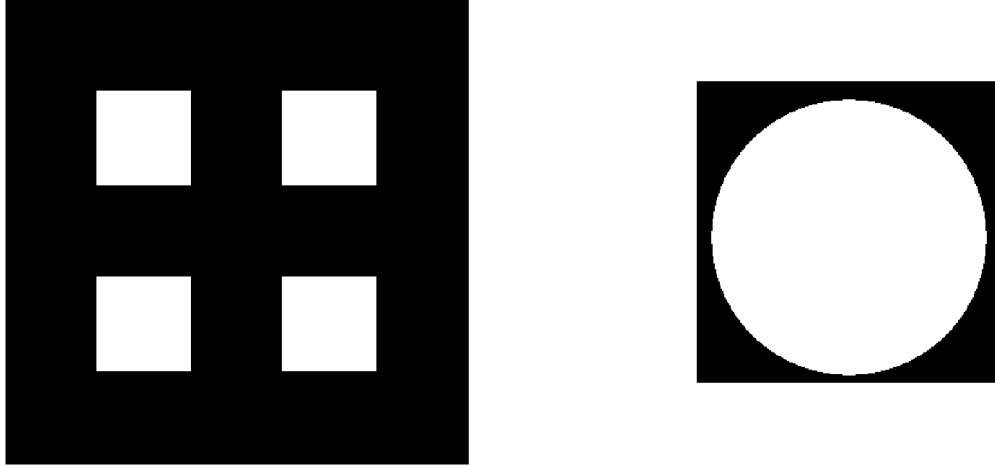
Figure 2.8: The four squares to be segmented are shown in white in the image on the left for clarity. The border between the white and black areas on the right is the mask used to initialize the level set method. A circular mask was picked at random and any arbitrary shape could be used instead.

the parameters of the level set that were later used in the 3D algorithm. This procedure will be discussed in further detail in the next chapter. The primary goal of this section was to establish and test the ability of the level set to segment regions of "high" difficulty which will be encountered while delineating CSF regions and areas of brain tissue in 3D.

2.8   Summary

This chapter established the primary equations, models and methods that will be employed elsewhere in this thesis. In this chapter we defined the problem statement, the methodology and the primary difficulties that were faced during the segmentation process. The CT data sets that were used are presented in this chapter along with their properties. Section 2.7 introduced the capabilities of the level set algorithm in 2D by presenting three example problems and the finished segmentations. Comments are made regarding the level set method and the initialization procedure that will be followed in Chapters 3 and 4 where the problem solution and the simulation results are presented respectively.

(a) 1 iteration

(b) 200 iterations

(c) 500 iterations

(d) 700 iterations

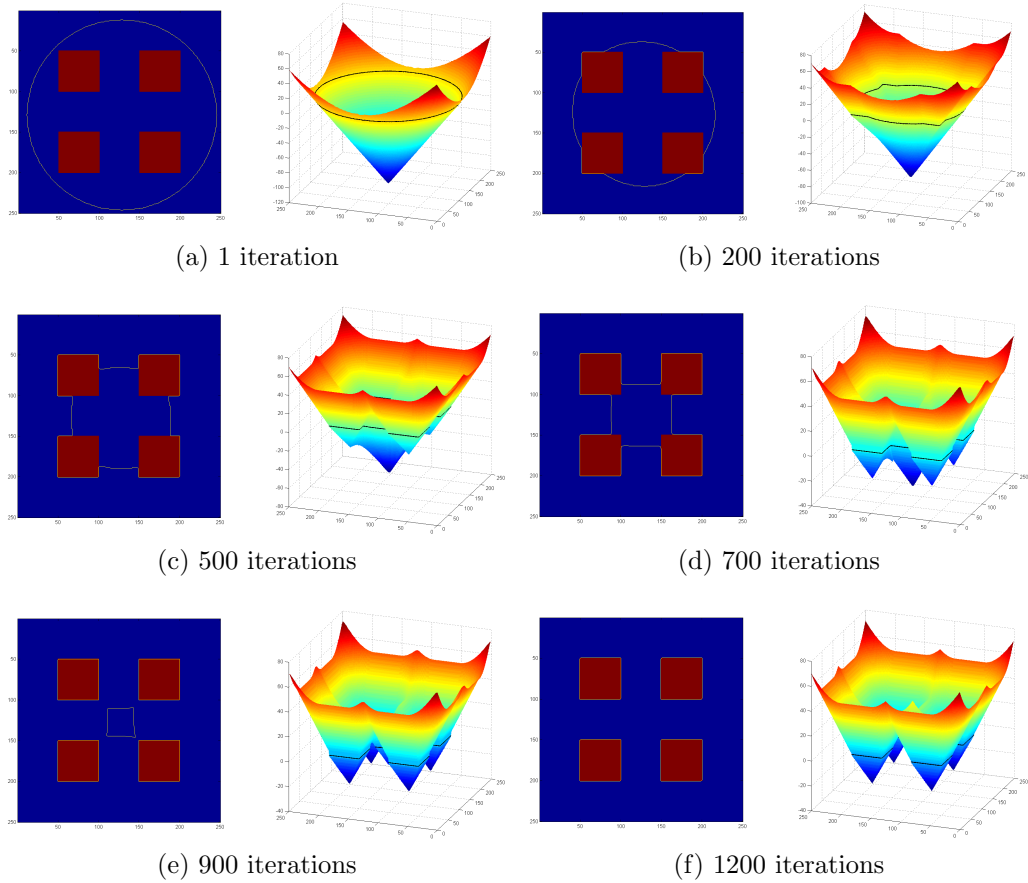(e) 900 iterations

(f) 1200 iterations

Figure 2.9: In 2.9a the yellow line shows the initial mask in the image on the left. The conical surface on the right in all the images is the 3D implicit surface that is being manipulated by the level set. The implicit surface and its importance will be discussed in further detail in Chapter 3. In 2.9e the level set has extracted the desired features; however, the algorithm is not complete until the stopping criterion is triggered in 2.9f.
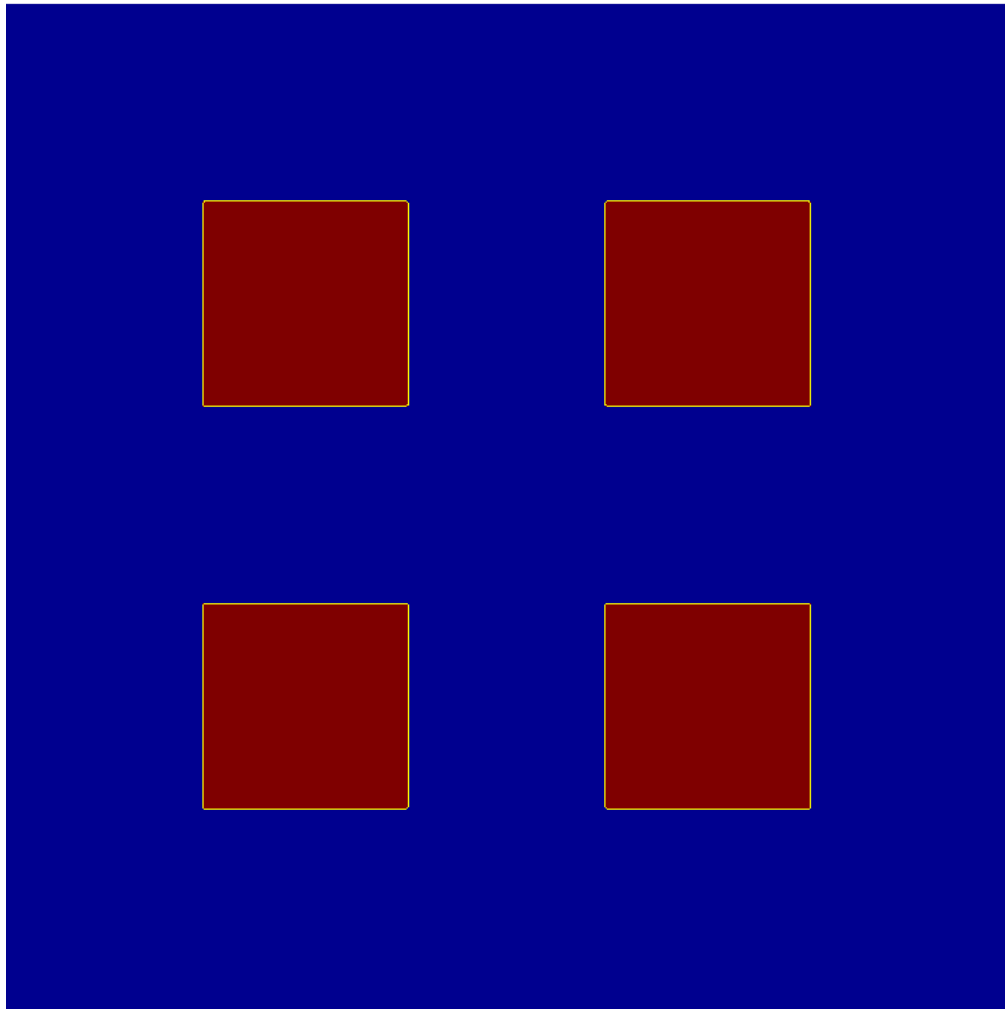
Figure 2.10: The difference in the thickness of the yellow lines (segmentation boundaries) is due to the conversion from one picture format to a LaTeX friendly version. The level set algorithm successfully segmented the edges of the squares in each of the four cases.

(a) Original image to be segmented.

(b) Finished segmentation.
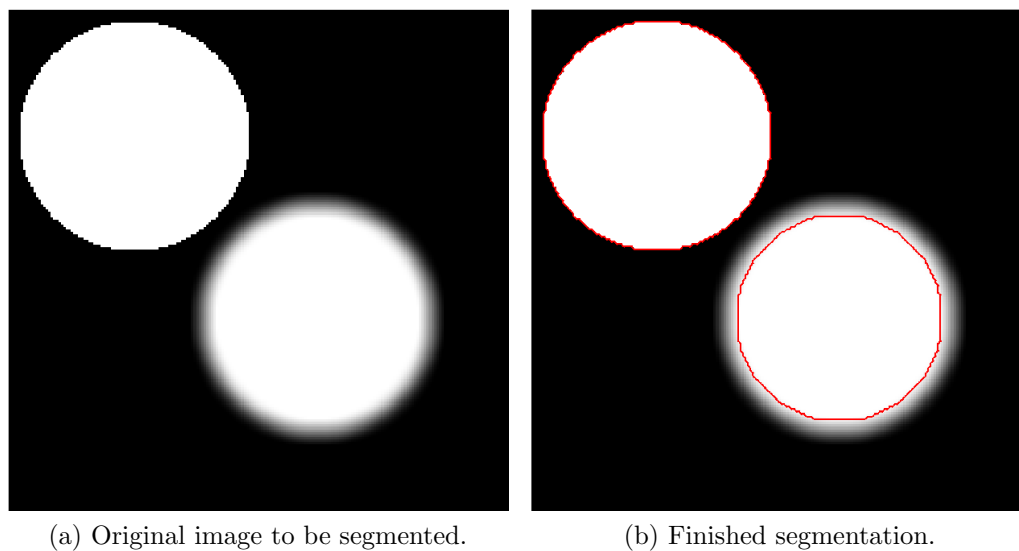
Figure 2.11: The image on the left shows a circle and a copy of it with a Gaussian blur applied. On the right, the finished segmentation is shown of both circles. The level set algorithm successfully tracked the edge of the circle that was transformed under a Gaussian kernel.

(a) Original image to be segmented.

(b) Finished segmentation.
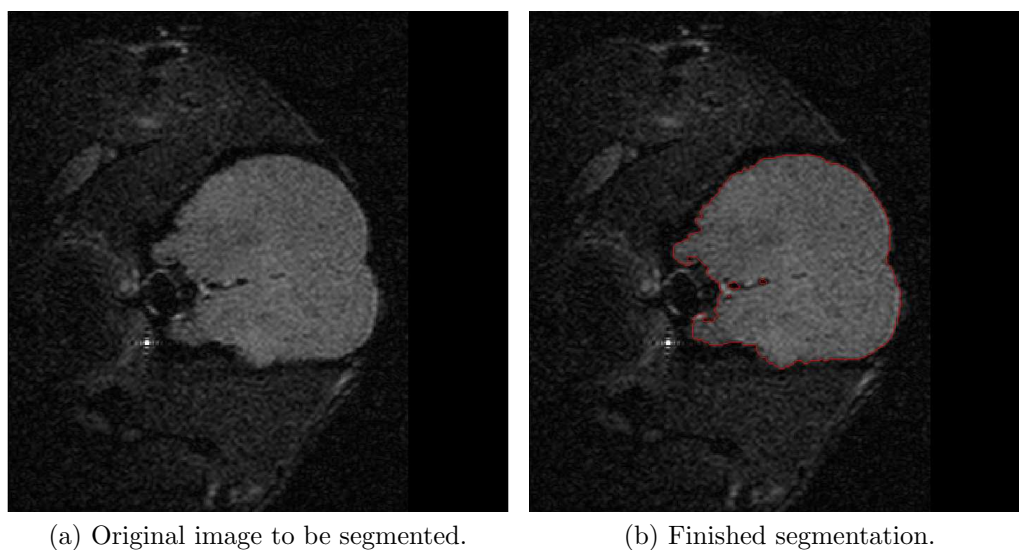
Figure 2.12: The 28th CT slice is shown on the left with a finished segmentation of the brain tissue next to it. This slice shows the algorithm accurately tracing out both concave and convex regions without any discrepancy.

(a) Original image to be segmented.   (b) Finished segmentation.
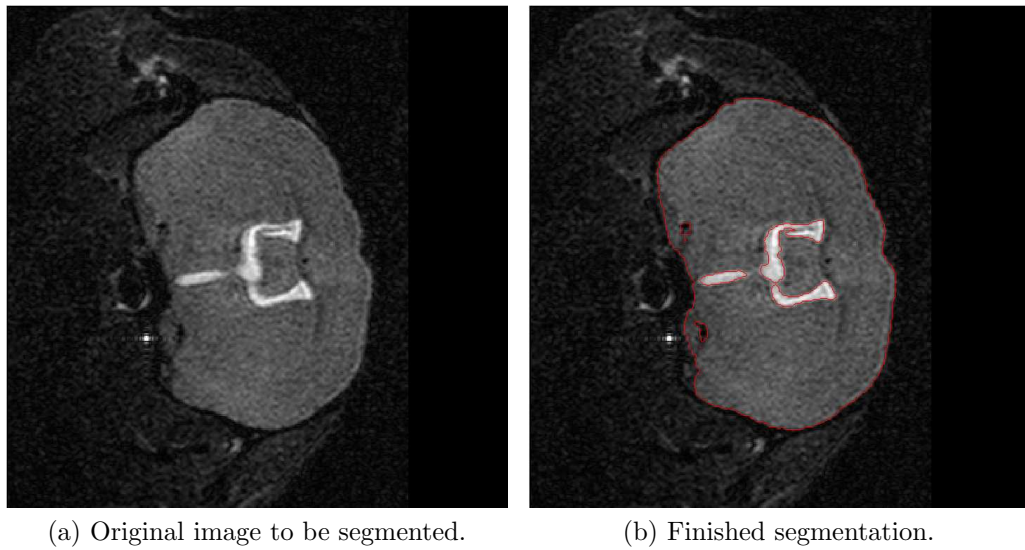
Figure 2.13: The 41st CT slice is shown on the left with a finished segmentation of the brain tissue and CSF regions on the right.

Application of a 3D Level Set Method

We start this chapter with a discussion on implicit surfaces. The compact and the expanded forms of the general level set equation for image segmentation that are used in this work are introduced along with an explanation of each parameter. The concept of a signed distance transform used to initialize the algorithm provides an understanding of the relationship between implicit surface definition and the level set. A numerical scheme for evolving the level set forward in time based on the sign of the spatial derivative is discussed as well as the stability of the algorithm. Equations for the difference of normals method are provided for calculating the mean curvature of the interface. We close the chapter with an example volume segmentation and introduce a definition for the stopping criterion used to determine when to stop evolving the interface.

3.1   Introduction

Suppose that the real line is divided into three distinct sets using the points $x = -1$ and $x = 1$. And using these points, we further define three separate subdomains as $(-\infty, -1)$, $(-1, 1)$ and $(1, \infty)$. Let us refer to $\Omega^- = (-1, 1)$ as the *inside* partition of the domain and $\Omega^+ = (-\infty, -1) \cup (1, \infty)$ as the *outside* partition of the domain. The border, $\partial \Omega$, between the *inside* and the *outside* is made up of the two points

$\partial\Omega = \{-1, 1\}$ and is referred to as the *interface*. In $\Re^3$ the *inside* and *outside* regions are one-dimensional objects, however the interface is zero-dimensional. In general, for subdomains that are n-dimensional the *interface* will always be of dimension n-1, or it's said to have codimension one.

In order to have an *explicit* interface representation, one simply lists the points that belong to the interface, e.g. $\partial\Omega = -1, 1$. On the other hand, an *implict* representation describes the interface as an isocontour of some function $\phi(x)$. For example, the zero isocontour of $\phi(x) = x^2 - 1$ is the set of all points such that $\phi(x) = 0$. This set contains only two points, $\partial\Omega = \{-1, 1\}$. This illustration can be visualized in Figure 3.1 from [60]. Note that the zero isocontour is used to represent the lower dimensional interface; however, it should be said that there is nothing significant about $\phi(x) = 0$. This was chosen arbitrarily and is used in general due to the well known fact that two different functions ϕ and $\hat{\phi}$ have identical properties up to a scalar translation for some $a \in \Re^3$.

Extending this concept to two spatial dimensions implies that the interface is a curve that separates $\Re^2$ into multiple subdomains of nonzero area. Let it be noted that we limit our interface curves to those that are closed for purposes of clarity, i.e. we need to be able to discern between interior and exterior regions without ambiguity. Figure 3.2 from [60] shows the zero isocontour and the interior and exterior regions of $\phi(x) = x^2 + y^2 = 1$. The zero isocontour in this example is a unit circle defined by $\partial\Omega = \{\vec{x} | |\vec{x}| = 1\}$.

This concept of implicit surface representation is easily extended to 3D where the interface is a surface that separates $\Re^3$ into nonzero volumes. This is vital to understanding dynamic implicit surfaces and their relation to the level set method. In two dimensions, explicit interface definition can be tedious but not impossible since all one needs to do is specify all the points that lie on the curve. For the example in Figure 3.2, the interface can be defined as $\partial\Omega = \{\vec{x} | |\vec{x}| = 1\}$. This becomes an impossible task in three dimensions and two dimensions when one begins to consider that complicated two-dimensional curves do not have simple analytical descriptions [60].
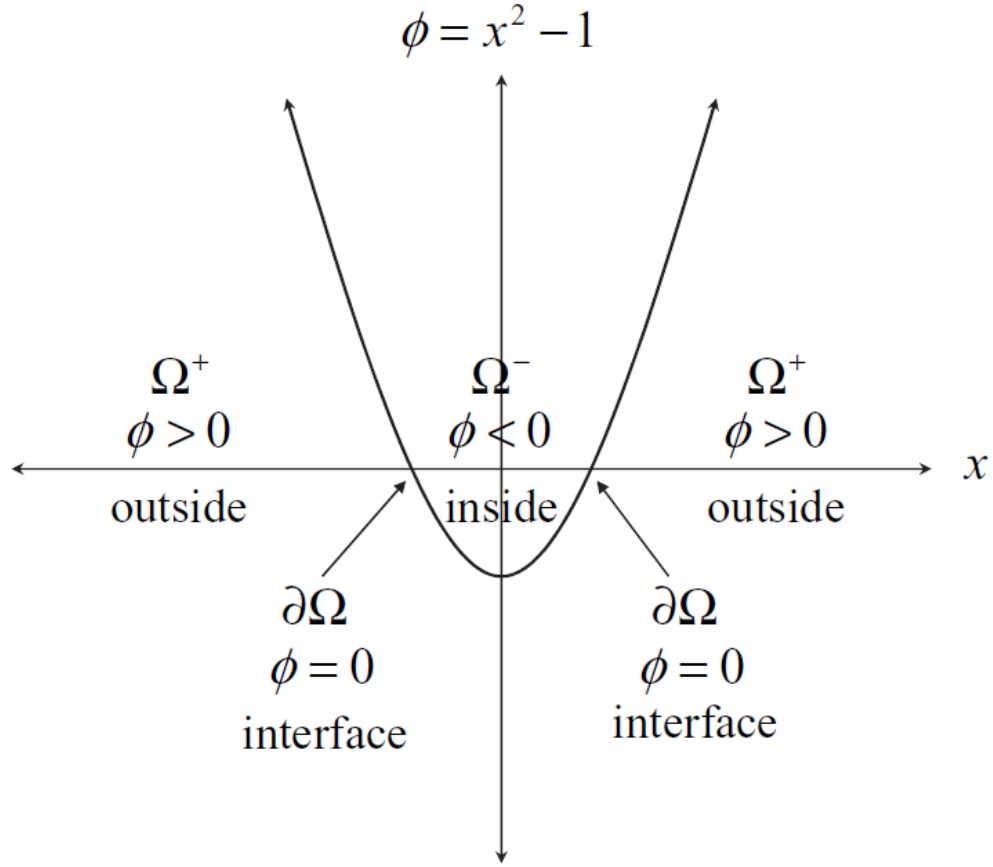
$$\phi = x^2 - 1$$

Figure 3.1: Implicit function $\phi(x) = x^2 - 1$ defining the regions Ω^- and Ω^+ as well as the boundary $\partial\Omega$.

3.2 Extending Level Sets to 3D

The level set method evolves a contour (in two dimensions) or a surface (in three dimensions) implicitly by manipulating a higher dimensional function called the level set function $\phi(x, t)$ [70]. This contour or a surface is analogous to the *interface* we discussed in 2.7 and corresponds to the zero level set $\Gamma(x, t) = \{\phi(x, t) = 0\}$. The case for using the level set method was made in 1.2.4 and one of the most important traits is evidenced in Figure 3.3. Here it can be seen that topological changes, e.g. merging and splitting of contours are done implicitly and without detriment to the stability of the algorithm. Originally introduced by Osher and Sethian in [57], the level set method has become widely used across many fields such as image processing, computer graphics and computational fluid dynamics.
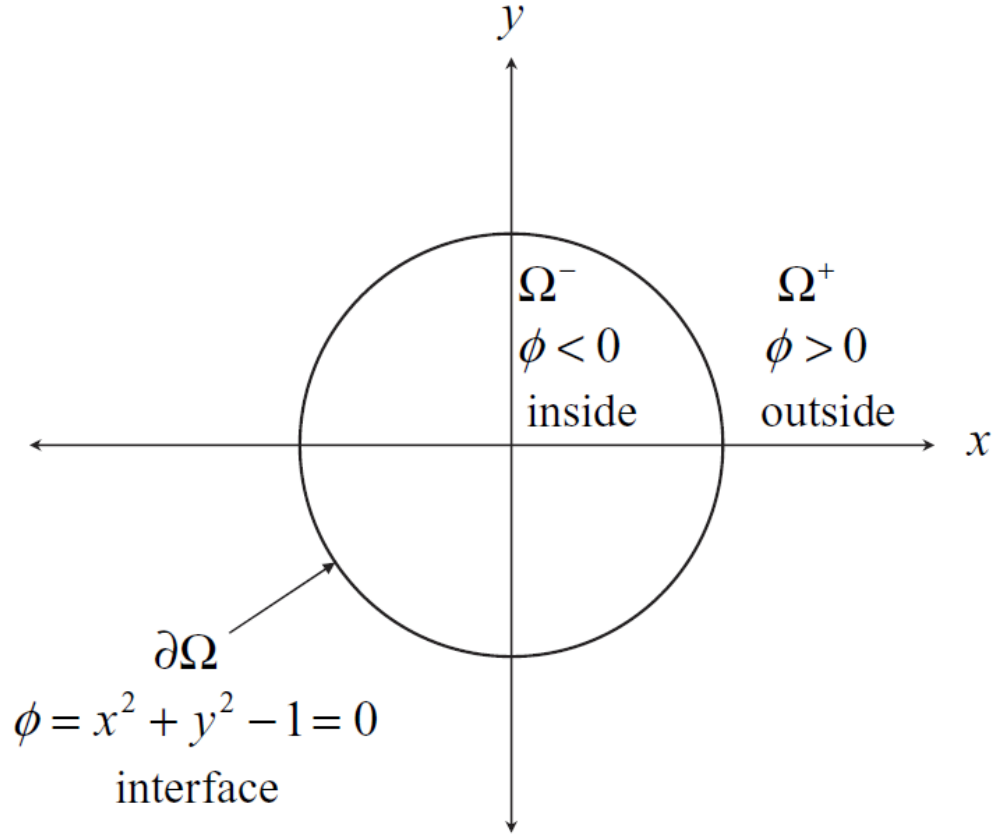
Figure 3.2: Implicit function $\phi(x) = x^2 + y^2 - 1$ defining the regions Ω^- and Ω^+ as well as the boundary $\partial\Omega$.

The level set methods add to the implicit surface construct by introducing *dynamics* to the system. This idea was motivated by the Hamilton-Jacobi approach to the numerical solutions of a time-dependent equation for a changing implicit surface [60]. The evolution or rather deformation of this implicit surface is controlled by a level set equation - which takes the form of a basic convection equation. The implict surface is deformed in an externally generated "velocity" field. The general form of the level set equation is given in Equation 3.1. The solution to this partial differential equation is computed iteratively.

$$\frac{\partial\phi}{\partial t} = -|\nabla\phi| \cdot F \tag{3.1}$$

In Equation 3.1, F is the forcing function, or the "velocity" term that is used to evolve the implicit surface over time. F can take many forms and is dependent
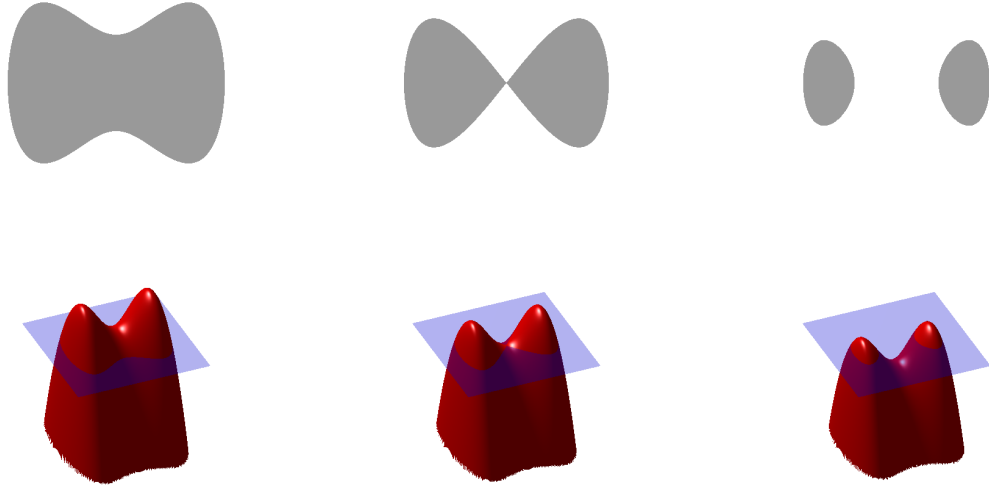
Figure 3.3: The evolving surface can be seen on the bottom along with the zero level set interface on the top which splits as the surfaces deforms.

on the nature of the problem. By carefully making our choice of F, we can guide the level set towards a desired segmentation based upon our problem formulation [70]. In attempting to avoid problems with instabilities, deformation of surface elements and having to account for topological repair of interfaces, ϕ is used to represent both the itnerface and to evolve the interface [60]. The level set equation in this paper is used under the assumption that the velocity term, F is defined on the entire implicit surface and not just the zero level set for purposes of simplicity when we define the term on the Cartesian grid. This term as stated above is chosen based upon the problem statement. For example, when the zero level set represents the interface between two different fluids, the velocity term is calculated using the two-phase Navier-Stokes equations [60].

3.3   Image Segmentation using Level Sets

In image processing applications, F is usually constructed using the pixel intensity and curvature information from the data set. Not including the curvature term would create contour leaking across anatomical boundaries because there would be no force to smoothen high curvature areas. When the implicit surface evolves across anatomical objects, the curvature term imposes a "smooth" condition on the surface based upon the geometry of the segmentation and the initial parame-

ters. Segmenting objects in general is often difficult, especially for those with high curvature regions because in order to compensate for such features, the curvature term has to be set to a low value [70]. This illustrates the opposite extreme of not including a curvature term altogether in the forcing function, F.
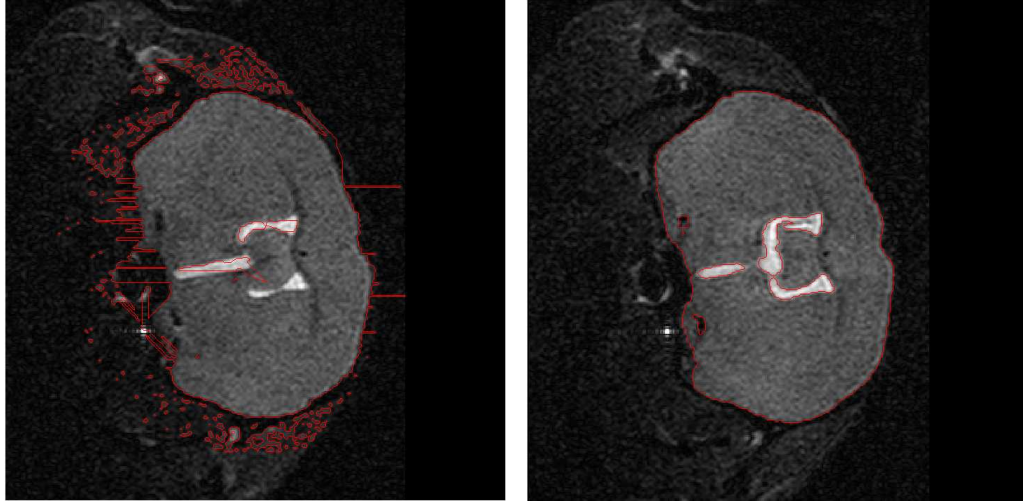
(a) Example of contour leaking $\alpha = 1$.   (b) Ideal segmentation without leaking $\alpha = 0.5$.

Figure 3.4: This example shows how contour leaking presents itself in the segmentation when the curvature term is set to 0, i.e. when $\alpha = 1$.

In this work we adopt the forcing term, F, developed in [78], [22], [79] and [70] which is dependent solely on data and curvature functions with a weighting parameter between the two. This is a typical formulation used in segmenting volume image data with level sets. Equation 3.2 shows the expanded form of the level set equation introduced in 3.1.

$$\frac{\partial \phi}{\partial t} = -|\nabla \phi| \left[\alpha D(I) + (1 - \alpha) \nabla \cdot \frac{\nabla \phi}{|\nabla \phi|} \right] \tag{3.2}$$

In 3.2 the data function $D(I)$ forces the implicit surface to expand or contract towards target features in the source data, I, while the mean curvature term $\nabla \cdot (\nabla \phi / |\nabla \phi|)$ keeps the level set function smooth. We introduce a weighting parameter, $\alpha \in [0, 1]$, that controls the smoothness of the implicit surface and therefore the interface. Using a combination of a data-fitting speed function and a curvature term is essential to applying level sets to volume segmentation [79].

Majority of level set data terms, D, from literature reduce to well known algorithms such as flood fill or edge detection when the free parameter $\alpha = 1$ [79]. This data function acts as the primary force that evolves the implict surface over the iteration time span. In making a choice for this D we require a model that will expand or contract based on the pixel intensity of the source data. In this work we adopt a well known speed function used by Lefohn, Whitaker and Cates in [79] and [80] which is shown below in Equation 3.3 and plotted in Figure 3.5 on page 42.

$$D(I) = \epsilon - |I - T| \qquad (3.3)$$

This speed function depends only on the central intensity value, T, of the input, or source, data I and the intensity deviation, ϵ around T. This means that the implicit surface as well as the interface contour will expand if a pixel, in 2D, or a voxel, in 3D, has an intensity value within the $T \pm \epsilon$ range, otherwise it will contract to exclude said pixel or voxel. Using this gradual forcing function implies that the effects of D subside as the as the implict surface approaches the boundaries of regions whose central intensity values lie within the $T \pm \epsilon$ range [79].
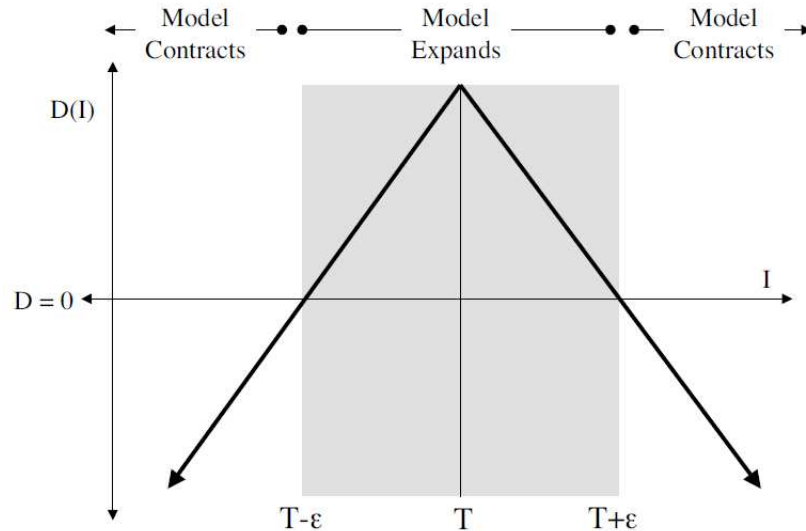
Figure 3.5: The speed function model based on image intensity causes the implict surface to expand and contract based on the initialization parameters, T and ϵ.

To control this algorithm, a user is only required to specify three parameters, T, ϵ and α along with an initial mask which will be discussed in section ??. This

mask can take any geometry; however, it must belong to the same n-dimensional space from which the source data is sampled, e.g. a square mask for 2D images or a spherical mask for volume data. The level set stops once it has been determined that ϕ has converged or after a certain number of iterations. We employ a stopping criterion for the level set algorithm that is discussed in section 3.8.

3.4 Signed Distance Transforms

In section 3.1 we defined the implicit functions with $\phi(x) \leq 0$ in the interior region Ω^-, $\phi(x) \geq 0$ in the exterior region Ω^+ and $\phi(x) = 0$ on the boundary $\partial\Omega$, or the interface. In this section we discuss the signed distance function, a subset of implicit functions, and its role in the level set algorithm. In this paper we use the standard definition of the signed distance function (SDT) requiring it to be positive on the interior, negative on the exterior and zero on the boundary as well as the having its gradient satisfy the eikonal equation, i.e. $|\nabla\phi| = 1$.

The SDT assigns a numerical value for every pixel, or voxel, within a binary image containing one or more objects which represents the infimum, or minimum distance if the metric space is Euclidean, between the the said pixel and the one closest to the boundary of the object(s) [70]. In this work we will restrict ourselves to working over $\Re^3$ and thus the mathematical definition of the distance function will take the form given below in Equation 3.4.

$$d(r, S) = \min|r - S| \text{ for all } r \in \Re^3 \tag{3.4}$$

The eikonal equation is true only in the general sense since it does not hold for points that are equidistant from at least two points on the interface. This causes the distance function to have a singularity point at the interface where $d = 0$ is a local minimum [79]. This, however, does not cause issues in general because the monotonic nature of the SDT across the interface allows it to be differentiated with greater confidence.

The SDT used in this algorithm comes from Matlab's *bwdist* function which computes the Euclidean distance transform of the binary image. This allows us to assign distance values as positive for pixels, or voxels, outside of the implicit sur-
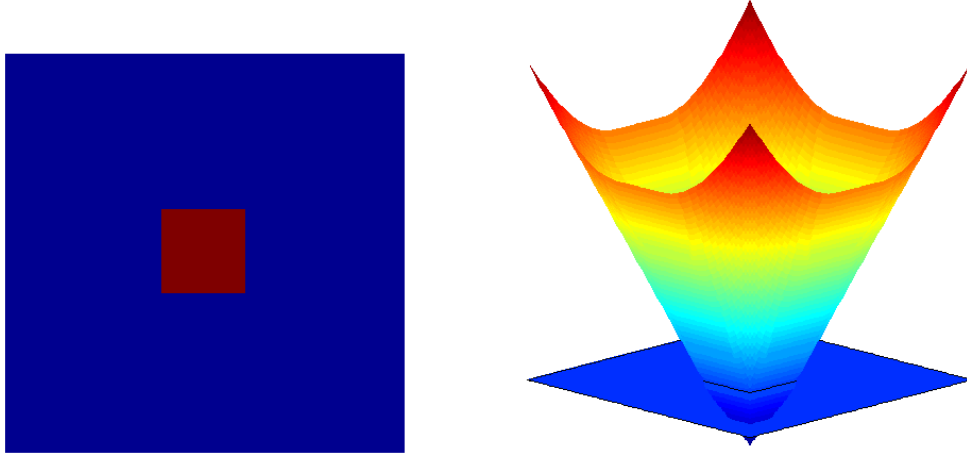
Figure 3.6: In the figure on the left we show an arbitrary initial mask, a square, in red. The signed distance transform of the mask is shown on the right along with the zero level set $\phi(x) = 0$.

face and negative for those that are located inside. The distance values obtained via the *bwdist* function represent the Euclidean distance; however, other common metrics could be used instead such as the Chebyshev distance or the Manhattan distance.

The SDT is used to transform an initial mask in order to initialize the level set equation as well as to reinitialize it after a select number of iterations in order to retain a constant gradient magnitude. This is chosen carefully because if reinitialization occurs after a low number of iterations then the level set will simply oscillate in place, comparable to being stuck in a minimum; however, if the number of iterations is too high then the risk of numerical instabilities occurring increases [80]. The level set algorithm thus requires two sets of data: an initial mask and source data, which contains the regions that will be segmented.

In section 2.7 we used $\phi(x) = x^2 - 1$ as an implicit representation of $\partial\Omega = \{-1, 1\}$. The equivalent SDT representation of the same points is $\phi(x) = |x| - 1$ and is shown below in Figure 3.7.

The SDT $\phi(x) = |x| - 1$ has the same $\partial\Omega$, Ω^-, and $\partial\Omega^+$ as the implicit function $\phi(x) = x^2 - 1$ including the additional eikonal condition $\nabla\phi(x) = 1 \ \forall \ x \neq 0$. At $x = 0$ the derivative is undefined; however, on the Cartesian grid this kink get numerically "smeared" out and the derivative will have a finite value [60].
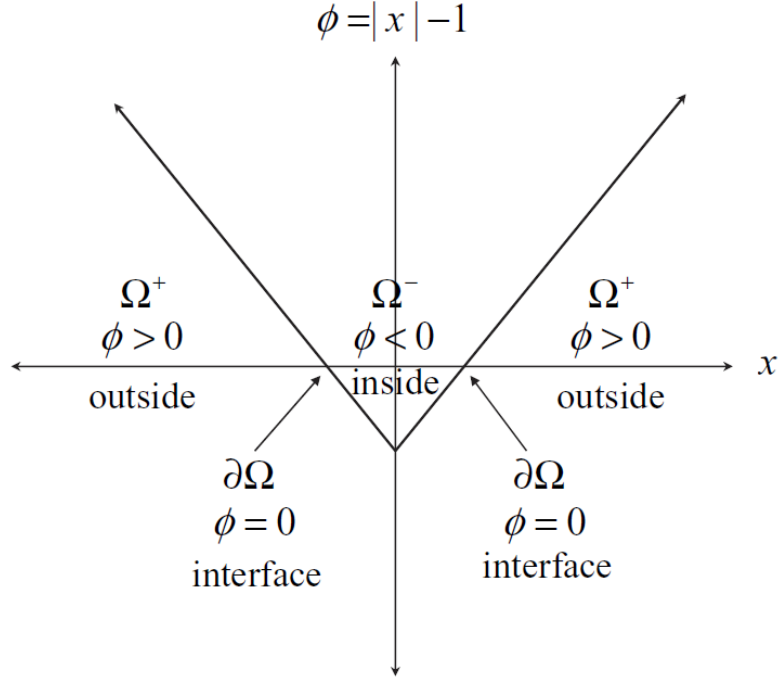
$$\phi = |x| - 1$$

$$\Omega^+ \qquad \Omega^- \qquad \Omega^+$$
$$\phi > 0 \qquad \phi < 0 \qquad \phi > 0$$
outside $\qquad$ inside $\qquad$ outside

x

$$\partial\Omega \qquad\qquad \partial\Omega$$
$$\phi = 0 \qquad\qquad \phi = 0$$
interface $\qquad\qquad$ interface

Figure 3.7: The signed distance transform function $\phi(x) = |x| - 1$ is shown which is a representation of the implict function $\phi(x) = x^2 - 1$.

3.5 Upwind Differencing

In equation 3.1, once ϕ and F are are defined at every grid point we can begin to apply a numerical scheme to evolve ϕ forward in time thus moving the implicit surface and the interface. Let us represent a point in time, t^n, and let $\phi^n = \phi(t^n)$ define values of ϕ at that point. In order to update ϕ, we first have to find new values at every grid point after some time increment, δt has elapsed. Using this notion we define new values of ϕ by $\phi^{n+1} = \phi(t^{n+1})$ where $t^{n+1} = t^n + \delta t$.

Using this notion we employ a first-order accurate method for time discretization of the level set equation using the forward Euler method from [60] given below in equation 3.5.

$$\frac{\phi^{t+\Delta t} - \phi^t}{\Delta t} + F^t \cdot \nabla\phi^t = 0 \tag{3.5}$$

Here ϕ^t represents the current values of ϕ at time t, F^t represents the forcing function at time t, and $\nabla\phi^t$ represents the values of the gradient of ϕ at time t. Great care must be taken in general when numerically discretizing partial differential

equations such as this one, especially with regard to the spatial derivatives of ϕ as in this case. Consider the expanded form of equation 3.6 below where $u, v\, w$ represent directional components of the velocity term F along the traditional axes.

$$\frac{\phi^{t+\Delta t} - \phi^t}{\Delta t} + u^t\phi_x^t + v^t\phi_y^t + w^t\phi_z^t = 0 \tag{3.6}$$

For simplicity, let us consider the one dimensional formulation of equation 3.7 at an arbirary point x_i

$$\frac{\phi^{t+\Delta t} - \phi^t}{\Delta t} + u_i^t(\phi_x)_i^t = 0 \tag{3.7}$$

where $(\phi_x)_i$ is the spatial derivative of ϕ at the point x_i. Using the method of characteristics tell us whether to employ the forward or the backwards differencing technique for propagating ϕ based on the sign of u_i at the point x_i. For example, if $u_i > 0$ the values of ϕ are moving from left to right, we have to look to the left of x_i to determine the correct value of ϕ at the end of the time step which requires backwards differencing. The opposite is true if $u_i < 0$ in which case forward differencing should be used to correctly approximate the value of ϕ_x. This method of choosing how to approximate the spatial derivatives based on the sign of u_i is known as *upwind differencing*, or *upwinding*.

We know that by combining the forward Euler method with the upwind differencing scheme we have a *consistent* finite difference approximation to the level set equation 3.1. This in turn guarantees us convergence, along with an imposition of a stability condition, in accordance to the Lax-Richtmyer equivalence theorem which states that a finite difference approximation to a linear partial differential equation is convergent [60]. Comments on the stability condition that is enforced will be made in section 3.7.

Extending this notion of upwinding to three dimensions and assuming an isotropic resolution from [81], [57], [64],[25] and [79] gives us the derivatives below that are required to propagate the level set equation. D_i, D_i^+ and D_i^- terms are used to abbreviate the second-order central, forward and backwards difference techniques respectively [70].

$$D_x = (\phi_{i+1,j,k} - \phi_{i-1,j,k})/2 \qquad D_x^+ = \phi_{i+1,j,k} - \phi_{i,j,k} \qquad D_x^- = \phi_{i,j,k} - \phi_{i-1,j,k}$$

$$D_y = (\phi_{i,j+1,k} - \phi_{i,j-1,k})/2 \quad D_y^+ = \phi_{i,j+1,k} - \phi_{i,j,k} \quad D_y^- = \phi_{i,j,k} - \phi_{i,j-1,k}$$
$$D_z = (\phi_{i,j,k+1} - \phi_{i,j,k-1})/2 \quad D_z^+ = \phi_{i,j,k+1} - \phi_{i,j,k} \quad D_z^- = \phi_{i,j,k} - \phi_{i,j,k-1}$$

$$(3.8)$$

$\nabla\phi$ is approximated using the upwind scheme.

$$\nabla\phi_{\max} = \begin{bmatrix} \sqrt{\max(D_x^+,0)^2 + \max(-D_x^-,0)^2} \\ \\ \sqrt{\max(D_y^+,0)^2 + \max(-D_y^-,0)^2} \\ \\ \sqrt{\max(D_z^+,0)^2 + \max(-D_z^-,0)^2} \end{bmatrix} \tag{3.9}$$

$$\nabla\phi_{\min} = \begin{bmatrix} \sqrt{\min(D_x^+,0)^2 + \min(-D_x^-,0)^2} \\ \\ \sqrt{\min(D_y^+,0)^2 + \min(-D_y^-,0)^2} \\ \\ \sqrt{\min(D_z^+,0)^2 + \min(-D_z^-,0)^2} \end{bmatrix} \tag{3.10}$$

Finally, depending on whether $F_{i,j,k} > 0$ or $F_{i,j,k} < 0$, $\nabla\phi$ is

$$\nabla\phi = \begin{cases} ||\nabla\phi_{\max}||_2 & \text{if } F_{i,j,k} > 0 \\ ||\nabla\phi_{\min}||_2 & \text{if } F_{i,j,k} < 0 \end{cases} \tag{3.11}$$

$$\phi(t + \Delta t) = \phi(t) + \Delta t F |\nabla\phi| \tag{3.12}$$

3.6 Curvature

The mean curvature of the interface is defined as the divergence of the normal vector $\vec{N}$ below in equation 3.13

$$\kappa = \nabla \cdot \vec{N} \tag{3.13}$$

so that $\kappa > 0$ for *convex* regions, $\kappa < 0$ for concave regions and $\kappa = 0$ over a plane. Though finite differencing could be used to compute the derivatives of the components of the normal vector, $\vec{N}$, it is generally easier to do so based on the values of the current level set derivatives as shown below.

$$
\begin{aligned}
D_x^{+y} &= (\phi_{i+1,j+1,k} - \phi_{i-1,j+1,k})/2 & D_x^{-y} &= (\phi_{i+1,j-1,k} - \phi_{i-1,j-1,k})/2 \\
D_x^{+z} &= (\phi_{i+1,j,k+1} - \phi_{i-1,j,k+1})/2 & D_x^{-z} &= (\phi_{i+1,j,k-1} - \phi_{i-1,j,k-1})/2 \\
D_y^{+x} &= (\phi_{i+1,j+1,k} - \phi_{i+1,j-1,k})/2 & D_y^{-x} &= (\phi_{i-1,j+1,k} - \phi_{i-1,j-1,k})/2 \\
D_y^{+z} &= (\phi_{i,j+1,k+1} - \phi_{i,j-1,k+1})/2 & D_y^{-z} &= (\phi_{i,j+1,k-1} - \phi_{i,j-1,k-1})/2 \\
D_z^{+x} &= (\phi_{i+1,j,k+1} - \phi_{i+1,j,k-1})/2 & D_z^{-x} &= (\phi_{i-1,j,k+1} - \phi_{i-1,j,k-1})/2 \\
D_z^{+y} &= (\phi_{i,j+1,k+1} - \phi_{i,j+1,k-1})/2 & D_z^{-y} &= (\phi_{i,j-1,k+1} - \phi_{i,j-1,k-1})/2
\end{aligned}
\tag{3.14}
$$

With the *difference of normals* method from [79] and [82], we compute curvature using the derivatives from above and the two normals $\mathbf{n}^+$ and $\mathbf{n}^-$.

$$
\mathbf{n}^+ =
\begin{bmatrix}
\dfrac{D_x^+}{\sqrt{(D_x^+)^2 + \left(\frac{D_y^{+x}+D_y}{2}\right)^2 + \left(\frac{D_z^{+x}+D_z}{2}\right)^2}} \\[2em]
\dfrac{D_y^+}{\sqrt{(D_y^+)^2 + \left(\frac{D_x^{+y}+D_x}{2}\right)^2 + \left(\frac{D_z^{+y}+D_z}{2}\right)^2}} \\[2em]
\dfrac{D_z^+}{\sqrt{(D_z^+)^2 + \left(\frac{D_y^{+z}+D_x}{2}\right)^2 + \left(\frac{D_y^{+z}+D_y}{2}\right)^2}}
\end{bmatrix}
\tag{3.15}
$$

$$
\mathbf{n}^- =
\begin{bmatrix}
\dfrac{D_x^-}{\sqrt{(D_x^-)^2 + \left(\frac{D_y^{-x}+D_y}{2}\right)^2 + \left(\frac{D_z^{-x}+D_z}{2}\right)^2}} \\[2em]
\dfrac{D_y^-}{\sqrt{(D_y^-)^2 + \left(\frac{D_x^{-y}+D_x}{2}\right)^2 + \left(\frac{D_z^{-y}+D_z}{2}\right)^2}} \\[2em]
\dfrac{D_z^-}{\sqrt{(D_z^-)^2 + \left(\frac{D_y^{-z}+D_x}{2}\right)^2 + \left(\frac{D_y^{-z}+D_y}{2}\right)^2}}
\end{bmatrix}
\tag{3.16}
$$

Using $\mathbf{n}^+$ and $\mathbf{n}^-$ to compute divergence, mean curvature is finally computed as shown below.

$$H = \frac{1}{2} \nabla \cdot \frac{\nabla \phi}{|\nabla \phi|} = \frac{1}{2}((\mathbf{n}_x^+ - \mathbf{n}_x^-) + (\mathbf{n}_y^+ - \mathbf{n}_y^-) + (\mathbf{n}_z^+ - \mathbf{n}_z^-)) \qquad (3.17)$$

3.7 Stability

Because we know that our solution is both consistent and stable, thereby guaranteeing its convergence, we can allow certain "kinks" in our algorithm because these errors will not be amplified as the solution is advanced forward numerically. The stability condition we use in the level set algorithm stems from the Courant-Friedreichs-Lewy (CFL) position which states that numerical waves should propagate at least as fast as the physical waves, i.e. $\Delta x / \Delta t > |u|$ [60]. With a simple manipulation, we obtain the CFL time step restriction of

$$\Delta t < \frac{\Delta x}{\max\{|u|\}} \qquad (3.18)$$

where $\max\{|u|\}$ is chosen as the largest value over the interface. This stability condition can be enforced by choosing a CFL number α such that $0 < \alpha < 1$.

$$\Delta t \left(\frac{\max\{|u|\}}{\Delta x} \right) = \alpha \qquad (3.19)$$

3.8 Stopping Criterion

The level set algorithm employs an automatic stopping criterion, δ, which terminates the segmentation algorithm. This δ was designed as a simple condition which is given below in equation 3.20.

$$\delta = \left| \left(\frac{V_i - V_{i-500}}{1000} \right) \right| < 1 \qquad (3.20)$$

Here V_i is used to represent the segmented volume at the ith iteration and we are further restricting that ϕ is evolved for a minimum of 500 iterations before δ is checked for the first time. This ensures that any circumstances during the incipient stage of the segmentation do not falsely trigger the stopping criterion because the volume quantity changes radically as the forcing function deforms the

implicit surfaces severely during the initial few hundred iterations as can be seen in Figure 3.8.
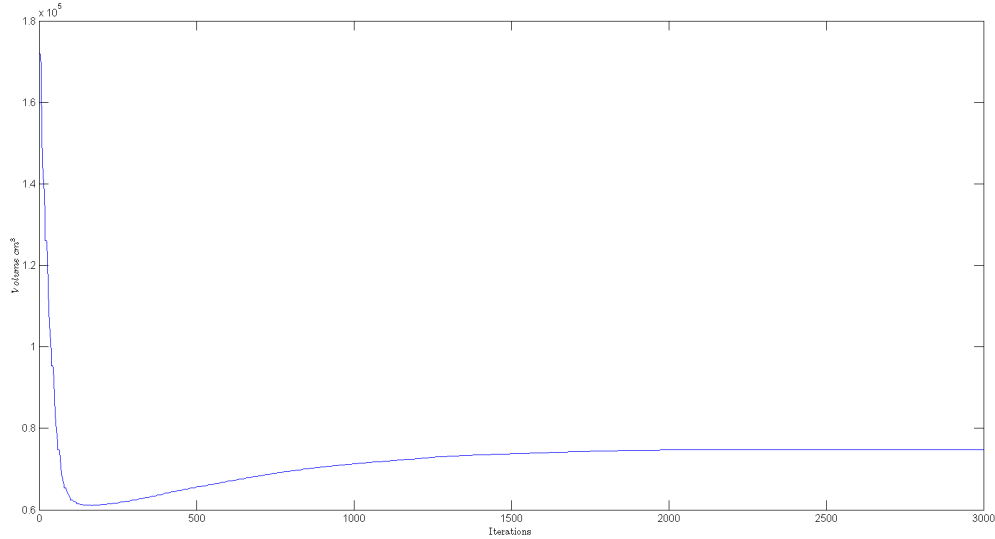
Figure 3.8: This figure shows CSF volume versus iteration for data set 27. The stopping criterion, δ is activated at iteration 1974; however, an extended iteration axis is shown to emphasize the accuracy of the stopping criterion.

The stopping criterion was chosen experimentally and provides a good trade off between accuracy and computational time since δ ensures that a volume change of less than one cubic centimeter occurs over 500 iterations.

3.9 Volume Segmentation Example

In this section we will show a simple example of a volume segmentation using the level set method. This will serve to aid in understanding of how the level set functions and bridge the gap between the equations that were presented earlier in this chapter and the process of segmenting CSF and brain tissue that will be described in section 3.10.

The example begins with creating a sphere approximation in Matlab of radius, $r = 45.5$. The sphere as it shall be referred to from here on is shown in Figure 3.9. We initialize the level set with a cube mask of size 50x50x50 and set the following parameters: $T = 1$, because the sphere was created using a logical statement, $\epsilon = 0.02$, because only the non-zero voxels were contained by the sphere, $\alpha = 0.5$,

because even though the sphere should ideally be the smoothest object - it was only a computer generated approximation. The stopping criterion was turned off during this simulation because the algorithm was noticed to have converged within 300 iterations.
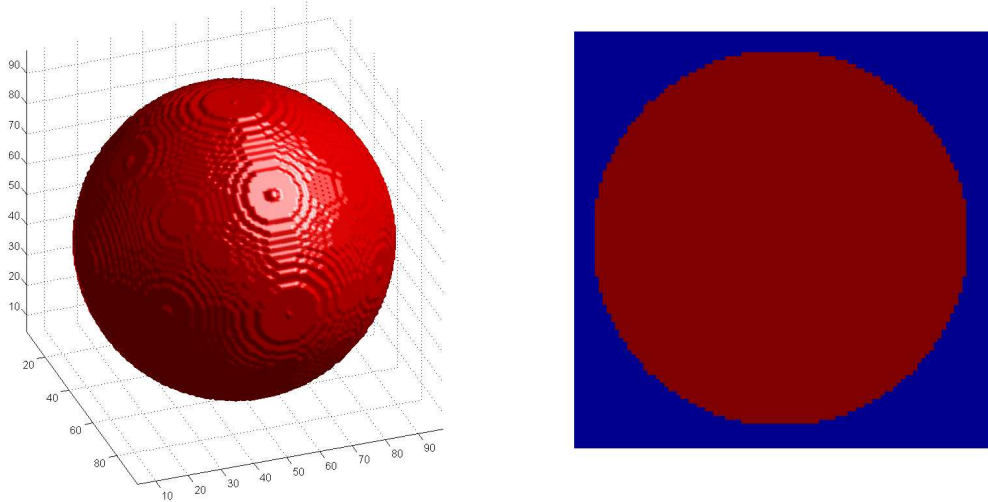
Figure 3.9: The figure on the left shows a computer generated sphere approximation of radius, $r = 45.5$, and an image of its projection onto a 2D plane on the right.

The finished segmentation results are provided below in Figures 3.10 and 3.11. Using the equation for the volume of a sphere we calculate the volume of the computer generated sphere to be 394569 voxels. Given that the sphere is merely an approximation, the actual number of voxels was calculated to be 407597 within the computer generated construct. The segmented result was 395327 voxels in size which translates to a 3% error when compared to the actual number of voxels in the computer generated sphere and 0.19% error in comparison to the theoretical volume.

3.10 CSF and Brain Tissue Segmentation

In this section we will cover the process for segmenting CT brain scans in 3D. The anonymized data is loaded into Matlab and arranged in a 3D array in ascending order starting with the scan corresponding to the base of the patient's head. Data
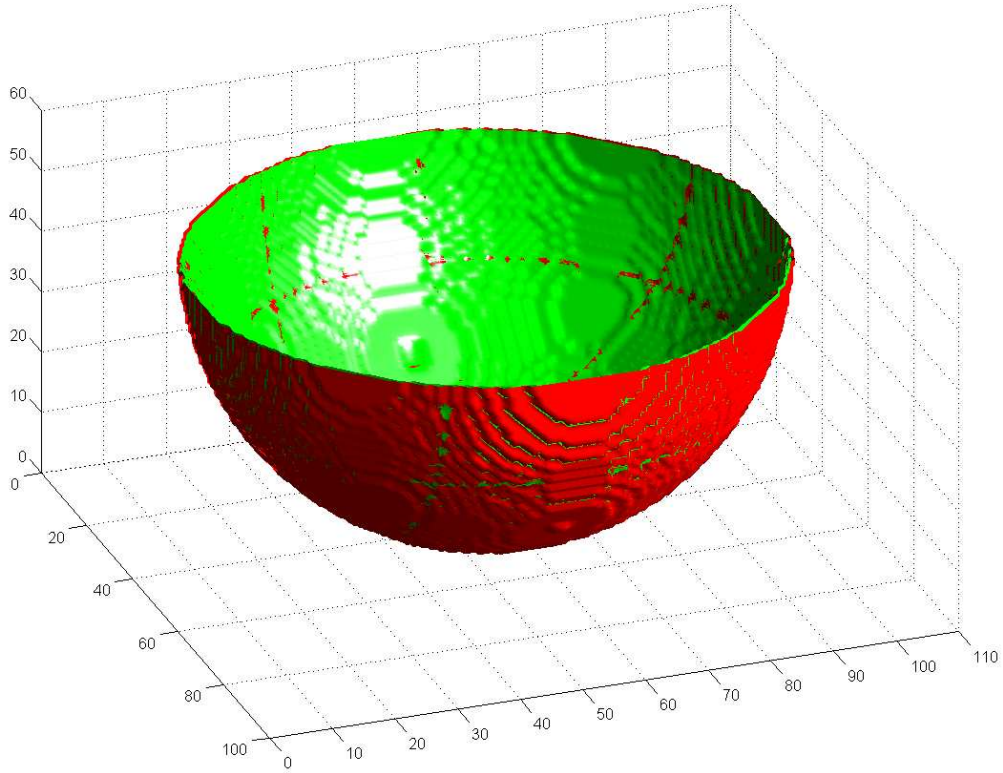
Figure 3.10: The image shows the generated sphere (red) and the segmented result (green) with the top half cut away for purposes of clarity. The errors between the segmented result and the source data can be seen in regions where the green and red areas intersect.

properties such as image size, pixel spacing, etc. were given in Table 2.2 on page 28. We segmented five different data sets of patients with hydocephalus.

The algorithm initialization parameters T, α and ϵ were chosen in the following manner. Central voxel intensity, T, was obtained through a series of data samples using Matlab's *imtool* GUI. Voxel intensities were obtained on three different planes, $X - Y$, for each of the data sets for both the CSF and brain tissue. The planes chosen for this sampling correspond to the quarter, half, and three-quarter locations on the vertical axis, Z, for all of the data sets. On each plane, ten voxels total were chosen, five for CSF and five for brain tissue, corresponding to known regions of CSF and brain tissue. The voxel samples were then averaged amongst the three planes to obtain a central voxel intensity value, T, that was used to initialize the level set method. Voxel intensity deviation, ϵ was calculated based on
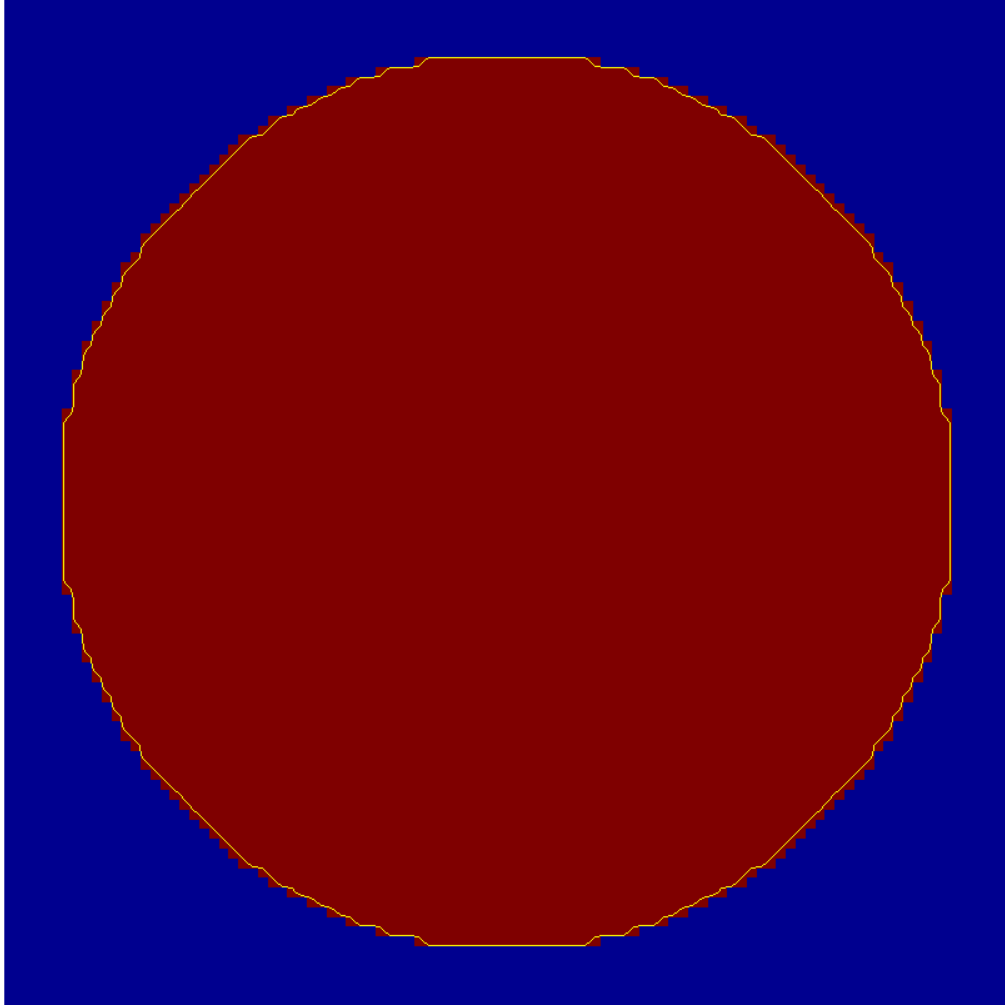
Figure 3.11: Aerial view, $X - Y$ plane, is shown in this image. When this view is projected to 2D, the area corresponding to the source data is 6621 voxels in size. The segmented area comprises 6505 voxels which represents a 1.75% error.

the difference between the CSF and brain tissue central intensities, T_{csf}, T_{bt} for a particular data set. The free parameter $\alpha = 0.5$ was used for all of the simulations because it provided a balance between the speed function and curvature. Table 3.1 on page 54 shows the initial parameters for the data sets. The differences in the initialization parameters, T, ϵ, for the five data sets result from variations in CT machine settings during the calibration procedure [83]. Slight variance exists between the five data sets which can be attributed to a number of factors such as: poor maintenance and irregular calibration, the data sets were not all produced using the same CT scanner and inconsistent tissue attenuation amongst patients.

Sensitivity analysis in section 4.4 was preformed to address this issue.

This method of choosing initialization parameters, T and ϵ, is validated with statistical analysis. Consider that the speed function model we used is analogous to a one-dimensional, two-class statistical classifier. Following the argument presented in [79] it becomes clear that generating a mean and a variance from a region of points to initialize T and ϵ is not only logical, but justified.

Table 3.1: Initialization parameters

Source	T_{csf}	ϵ_{csf}	T_{bt}	ϵ_{bt}	α
18	1030	10	1077	37	0.5
19	1030	10	1070	30	0.5
21	1031	11	1070	30	0.5
27	1027	7	1060	20	0.5
28	1033	9	1055	18.5	0.5

The initial mask that was used for segmenting CSF and brain tissue for all of the data sets was a rectangular prism with dimensions 200x200x15 because all of the data sets had the same dimensions along the x and y axes and typically contained 20 or more slices per data set. Sections 3.10.1 and 3.10.2 discuss the target regions and desired properties associated with segmenting CSF and brain tissue respectively.

3.10.1 Segmenting Cerebrospinal Fluid

In hydrocephalic patients one often encounters loculated CSF volumes. Figure 1.2 on page 9 gives an example of such a patient. The problem of segmenting CSF volumes in this thesis is restricted to delineating CSF that are not in contact with the skull. The only regions of CSF that are of interest are those that are within the brain and examples of such regions can be seen in Figure 1.2 on page 9. An example of a scan in which loculated regions are present within the brain is shown in Figure 3.12 on page 55. The areas identified as CSF in the scan are the only

CSF regions that are of interest and are sought to be segmented. Intra-brain fluid is important in diagnosis and treatment of hydrocephalus as well as determining quality of life and predicting brain development [2]. Because non intra-brain fluid is present in the images, i.e. fluid that is touching the skull, this makes the problem of accurately segmenting intra-brain fluid regions inherently difficult.

Figure 3.12: The four loculated regions of CSF that are not in contact with the skull are of interest, i.e. the areas identified with red lines, and are segmented by the algorithm. The skull boundary is identified with a blue line; the boundary, in this scan, is one contiguous region that shows to be white in color.

3.10.2   Segmenting Brain Tissue

Brain tissue volume is becoming more important in determining healthy brain treatment and cognitive development as referenced in subsection 1.2.2. Figure 3.13 on page 57 shows an example of a hydrocephalus brain. The problem at hand is to accurately trace out region(s) that are brain tissue. The difficulties associated with this task include non brain tissue areas in the lower part of the brain that have the same CT contrast values as brain tissue, protruding brain tissue in patients whose fontal bones have not fused together and presence of brain tissue inside CSF regions.
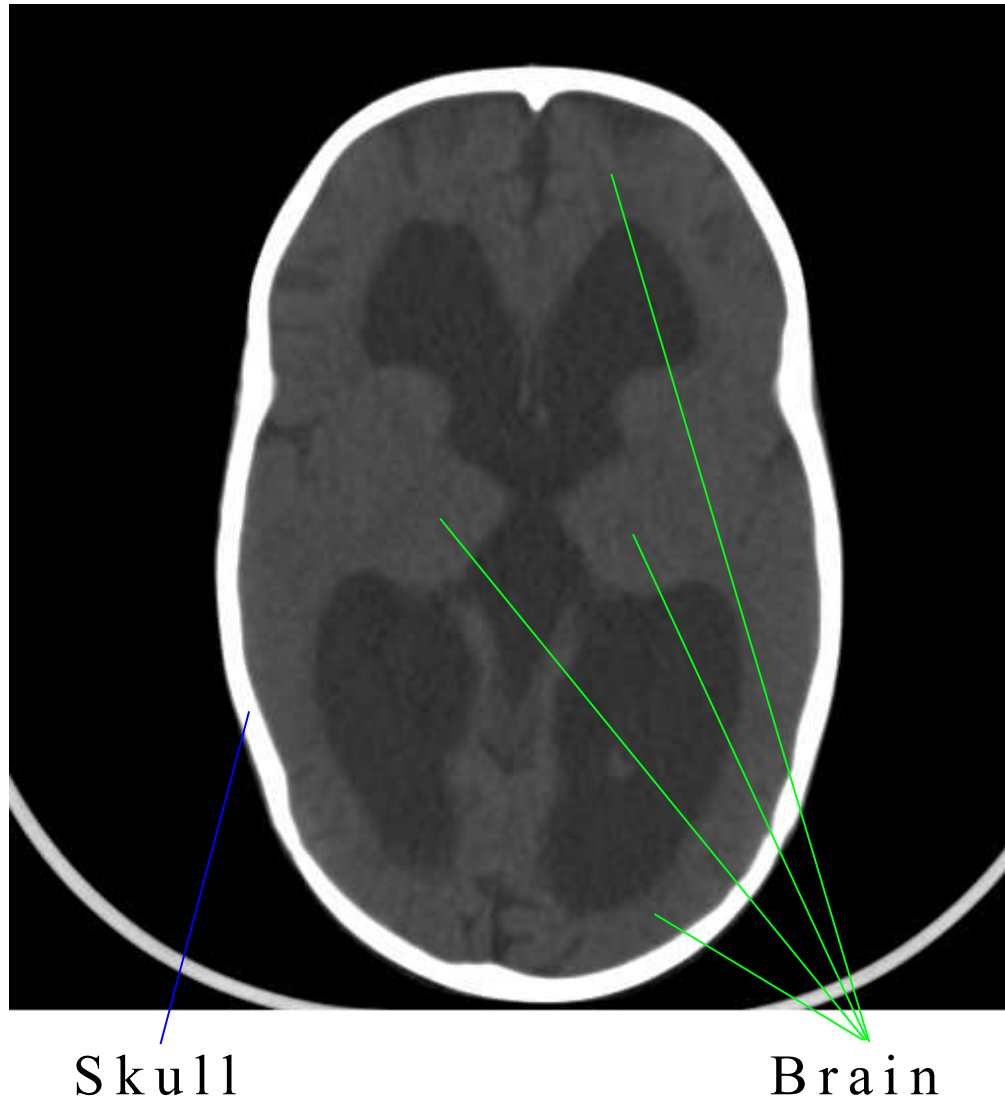
Figure 3.13: The brain tissue is identified with green lines and forms one contiguous area. The skull boundary is identified with a blue line; the boundary, in this scan, is one contiguous region that shows to be white in color.

Chapter 4

Results

4.1 Introduction

In this chapter we provide the results of the level set simulations for 5 different data sets. Volume segmentations of both CSF and brain tissue are included also. The results are compared against the ground truth values obtained via stereo investigator are provided courtesy of Dr. Steven Schiff, Director of Penn State Center for Neural Engineering. A sensitivity analysis is also included for the initialization parameters for one of the data sets. We conclude this chapter with a discussion of the segmentation results.

4.2 Computation Environment

The level set algorithm was developed in the Matlab R2010b environment; however, due to computing restrictions such as processing power and available physical memory, the computations were run on the Penn State Lion-X Series Clusters, specifically XI, XF and XJ clusters. These were chosen based upon observations of the period of time that elapsed while each batch job waited in queue to begin running. For each non-interactive batch job, or simulation, the following cluster parameters were used: 1 node consisting of 4 processors and 4GB of physical memory per process. Details on the Lion-X Cluster environment are not provided here and are considered to be outside the scope of this work.

4.3 CSF and Brain Tissue Volume Results

Complete CSF and brain tissue results are provided for each slice only for data set 21 in 4.3.1 on page 59. Data set 21 was chosen because we have worked with it the most throughout this thesis during the algorithm development and testing phases. The results for the remaining four data sets as well as data set 21 are summarized in Table 4.1 below. Subscripts *LS* and *SI* refer to the level set segmentation and the ground truth value obtain by the stereo investigator respectively. Stereo investigator is a tool used in stereology which allows a user to segment medical images by hand thus providing an accurate and unbiased area or volume for a desired target region. Typically, these devices combine a microscope and a computer with preloaded software that displays the image data using various options, filters and magnification levels. Percent error was calculated in the last column instead of percent difference because we consider the stereo investigator results to be exact.

Table 4.1: CSF and brain tissue volumes

Data Set	$Brain_{LS}$ (cm^3)	$Fluid_{LS}$ (cm^3)	$Brain_{SI}$ (cm^3)	$Fluid_{SI}$ (cm^3)	$Error_{Brain}$ $(\%)$	$Error_{Fluid}$ $(\%)$
18	1176.31	352.56	1151.20	349.40	2.18	0.90
19	682.63	823.41	693.25	830.00	1.53	0.79
21	1164.89	898.53	1145.00	806.00	1.74	0.82
27	961.73	71.56	961.63	70.63	0.01	1.32
28	753.84	335.58	744.38	338.18	1.27	0.77

4.3.1 Data Set 21

The results shown in Figure 4.1 on page 63 correspond to the zero level set interface of the brain tissue and CSF respectively for source data set 21. The surface interfaces shown in this figure suffer from poor resolution in the Z axis,

i.e. large slice thickness during CT scans, which gives the isosurfaces a "stepped" appearance.

Figure 4.2 on page 64 shows the CSF and brain tissue segmentations nested together. Volume visualization such as this can provide physicians additional information that will assist in diagnosing patients as discussed in [84] and [85].

Another way of visualizing the finished segmentation is by projecting the zero level set of the interface, $\phi = 0$, onto the 2D plane that corresponds to each CT slice. Again, the slices are numbered in ascending order starting at the base of the skull. The projections for the brain tissue and CSF segmentations are given in Figures 4.-2 on page 69 and 4.-6 on page 74 respectively.

4.4 Sensitivity Analysis

In this section we present the results of the sensitivity analysis. We tested the level set algorithm by simulating perturbations to the initial parameters, T and ϵ. The initial parameters were perturbed in the following manner: central voxel intensity, T, was offset by 0.5%, 1% and 1.5% from the original values of 1030 and 1077 for CSF and brain tissue respectively; intensity deviation, ϵ, was offset by 5%, 10% and 15% from the original values of 10 and 37 for CSF and brain tissue respectively. The percent offsets were determined based on the contrast intensity histogram and visual observations using Figure 4.-5 on page 75. The results are provided in Tables 4.2 and 4.3 below.

Table 4.2: Volumes for ϵ sensitivity analysis for data set 18

	0%	5%	10%	15%
CSF	898.53	910.24	915.47	926.54
Brain Tissue	1164.89	1221.53	1261.16	1332.10
$Error_{csf}$	0.82	0.47	1.05	2.27
$Error_{bt}$	1.74	6.68	10.14	16.34

Table 4.3: Volumes for T sensitivity analysis for data set 18

	0%	0.5%	1%	1.5%
CSF	898.53	913.23	927.51	941.68
Brain Tissue	1164.89	1198.92	1130.14	975.595
$Error_{csf}$	0.82	0.80	2.37	3.994
$Error_{bt}$	1.74	4.71	1.30	15.79

The sensitivity analysis performs as expected for the voxel intensity deviation parameter ϵ. Our hypothesis was that the volumes would increase with the degree of perturbation for both CSF and brain tissue. The same hypothesis does not hold for the central voxel intensity parameter, T, at least not for brain tissue. One explanation for this could be that the segmented region boundary between the outter edge of the brain tissue and the skull moves outwards, i.e. the interface expands, after the first perturbation. Then, the subsequent perturbations in T cause the segmented area to shrink because the interface between the brain tissue and the skull expands slower than the interface between the brain tissue and the CSF contained within, i.e. a smaller volume is segmented instead. There is roughly an increase of 1% error for every perturbation when segmenting CSF and 5% for brain tissue. This analysis was done to simulate effects of having untrained individuals perform the initialization part of the level set algorithm.

4.5   Discussion

This chapter presented the results of the level set simulations for CSF and brain tissue in five individuals with hydrocephalus. These results were compared to ground truth CSF and brain tissue volumes obtained via stereo investigator. The percent errors between our results and the stereo investigator show that the level set algorithm is an accurate and reliable method for determining CSF and brain tissue volumes. The level set method is however limited by the forcing function that we employ and thereby is unable to differentiate between regions with same

central voxel intensity as desired target regions. The inaccuracies stemming from this are further inflated by image artifacts such as streaking and partial volume averaging that appear in all the data sets in CT scans closest to the base of the skull.
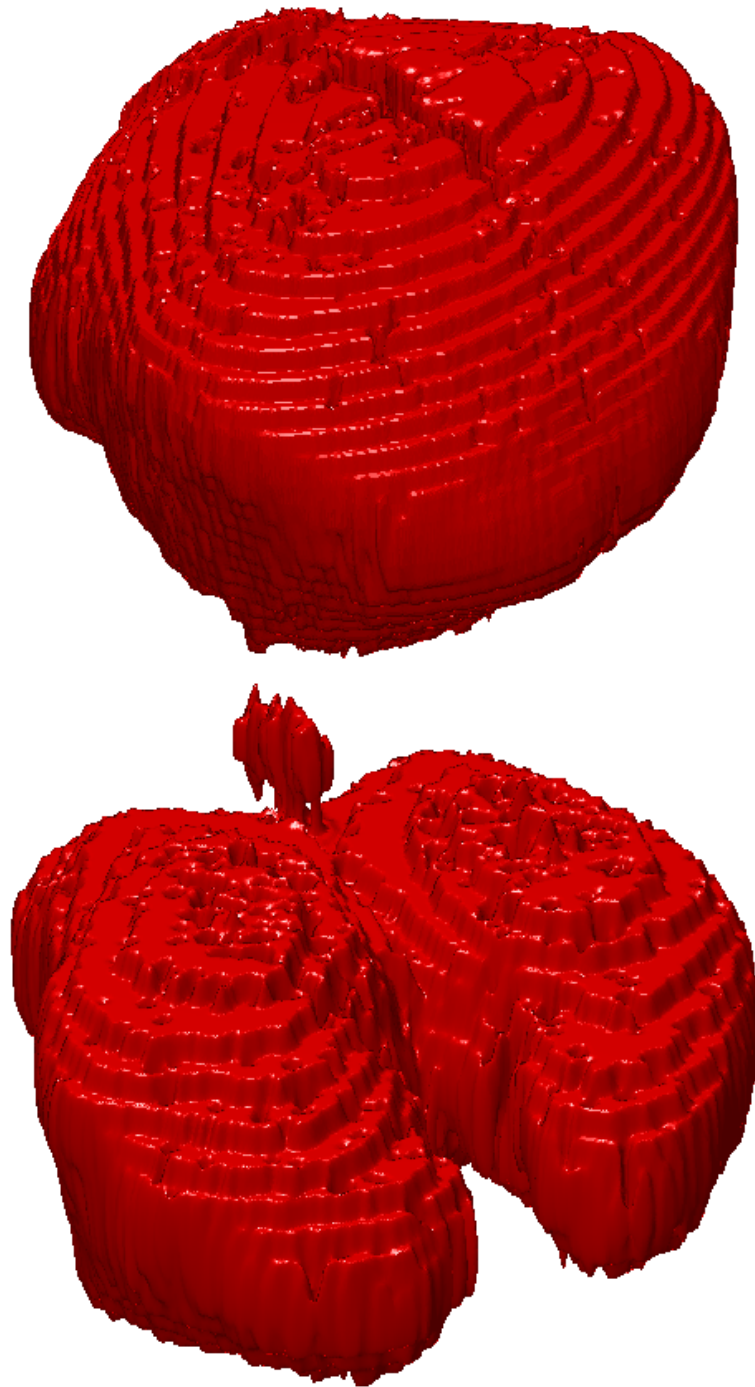
Figure 4.1: Top image shows various crevasses within the brain tissue where pockets of fluid and other non tissue regions exist. The brain tissue has a total volume of 682.63 cm^3. In the bottom image a region of loculated CSF can be seen between the two large, connected "hemispheres" of CSF. The fluid has a total volume of 823.41 cm^3.
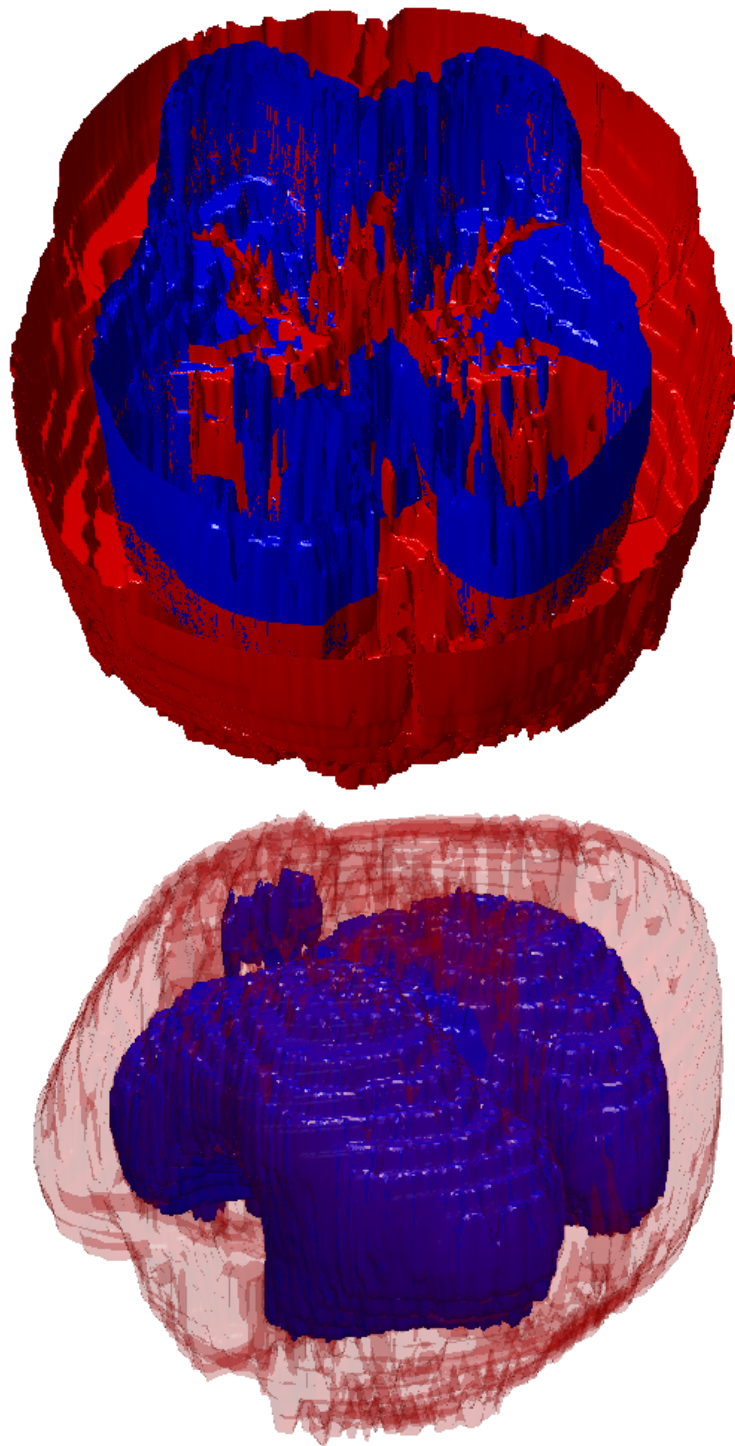
Figure 4.2: In the top image, regions of brain tissue, red, can be seen within the fluid volume in blue. In the lower image, the brain tissue has been set transparent in order to visualize the CSF region within. This highlights the severity of the conditions that some patients suffering from extreme hydrocephalus endure.
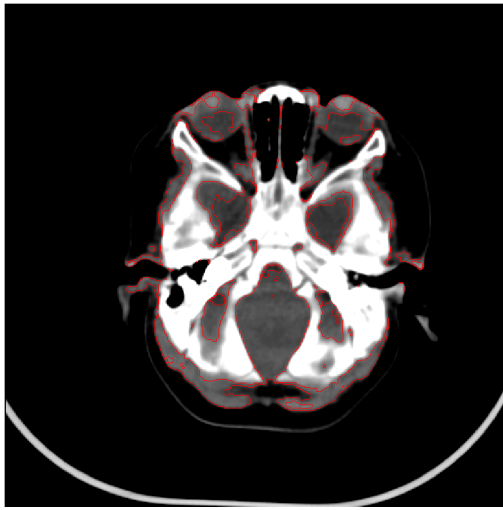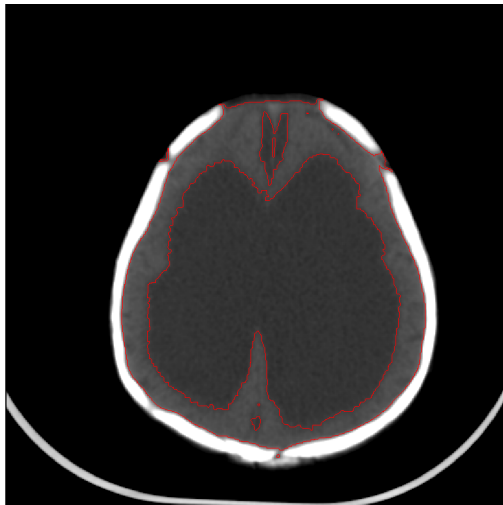
(iii) $Z = 1$
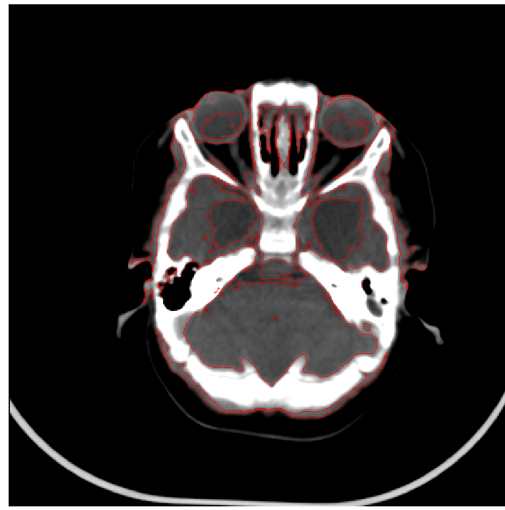
(iv) $Z = 2$
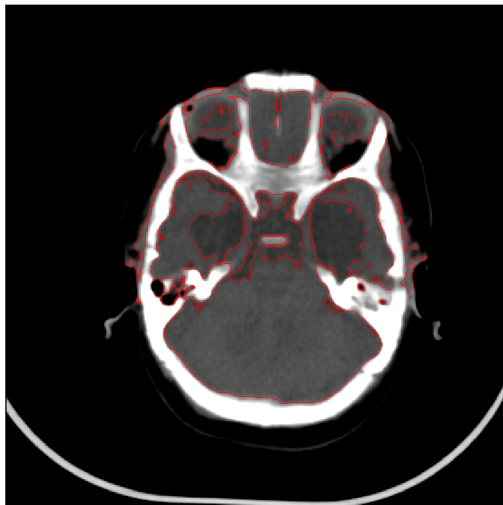
(v) $Z = 3$
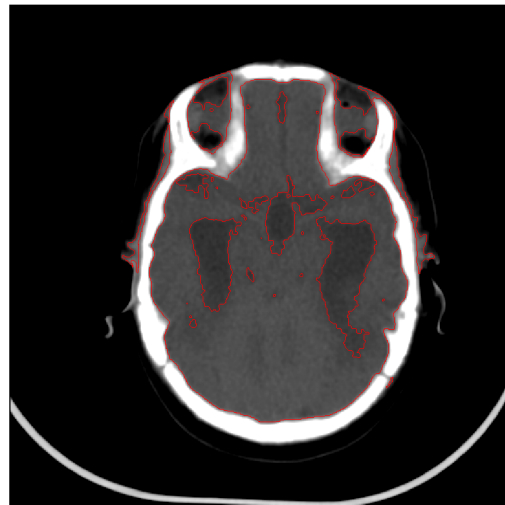
(vi) $Z = 4$
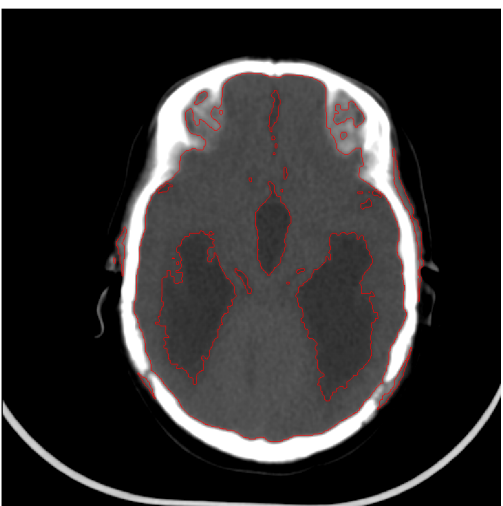
(vii) $Z = 5$
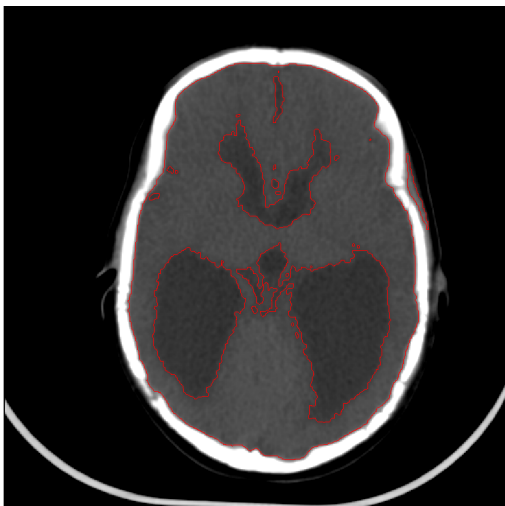
(viii) $Z = 6$
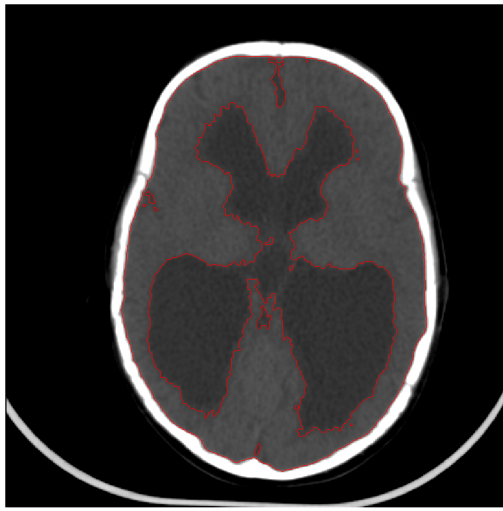
(ix) $Z = 7$
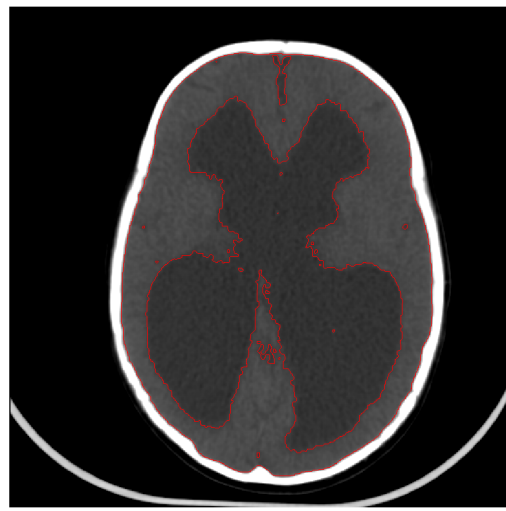
(x) $Z = 8$
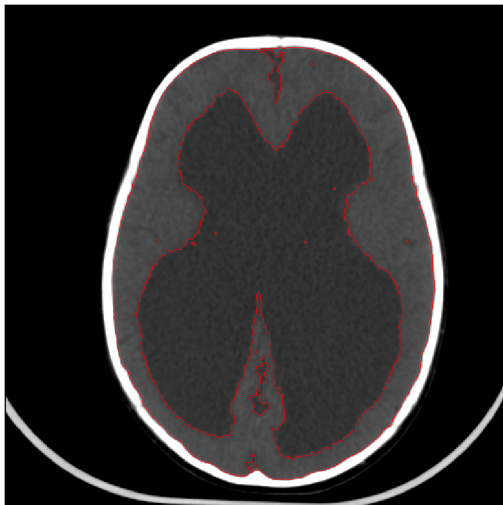
(xi) $Z = 9$
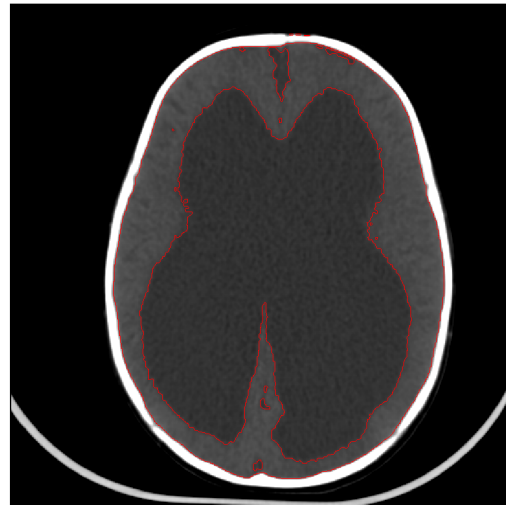
(xii) $Z = 10$
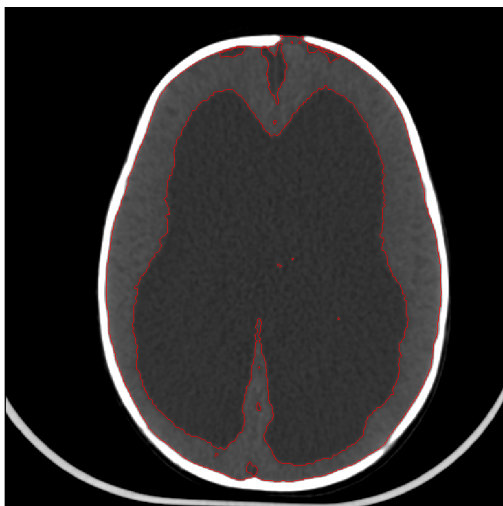
(xiii) $Z = 11$
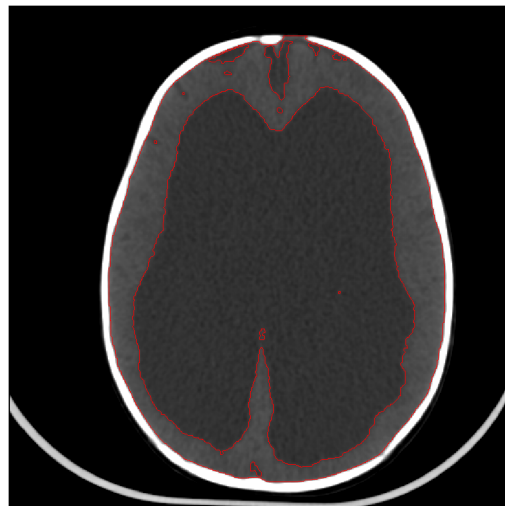
(xiv) $Z = 12$
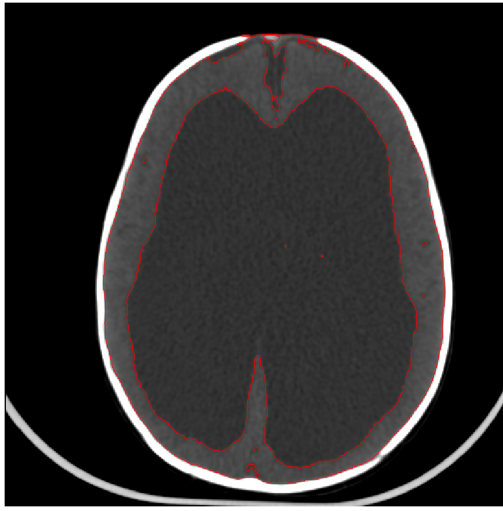
(xv) $Z = 13$
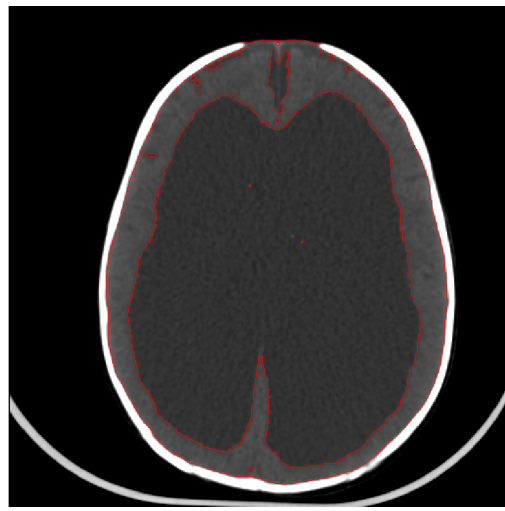
(xvi) $Z = 14$
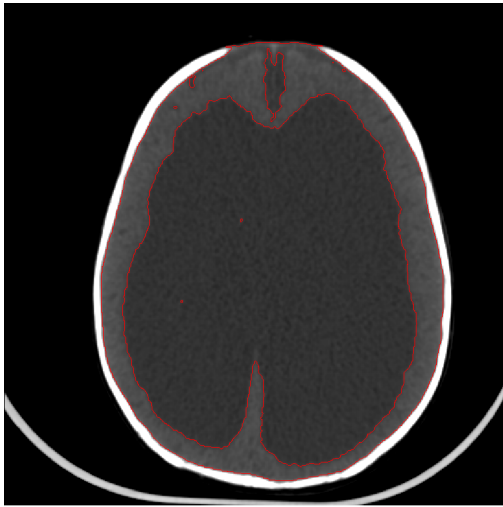
(xvii) $Z = 15$
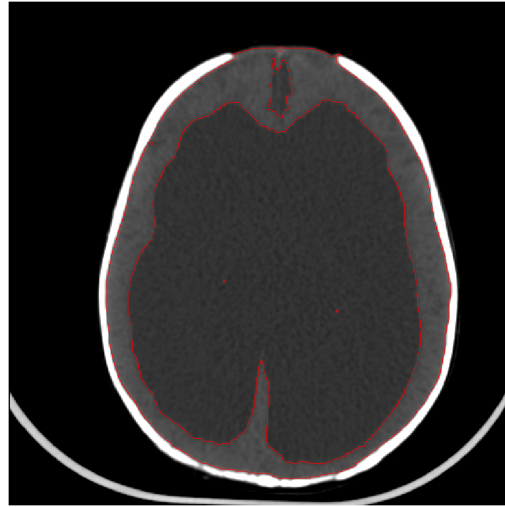
(xviii) $Z = 16$
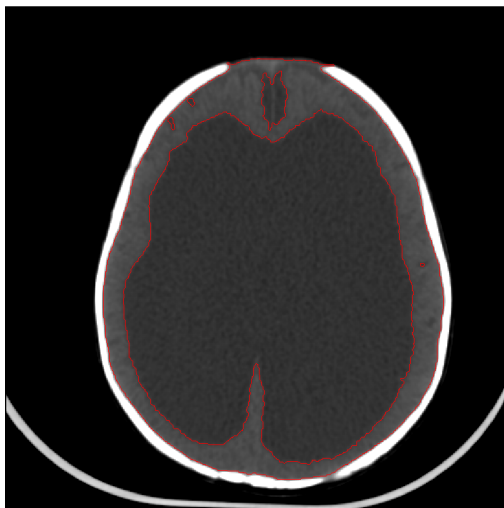
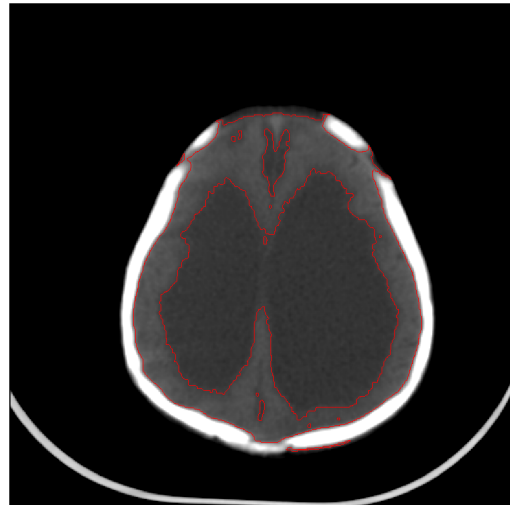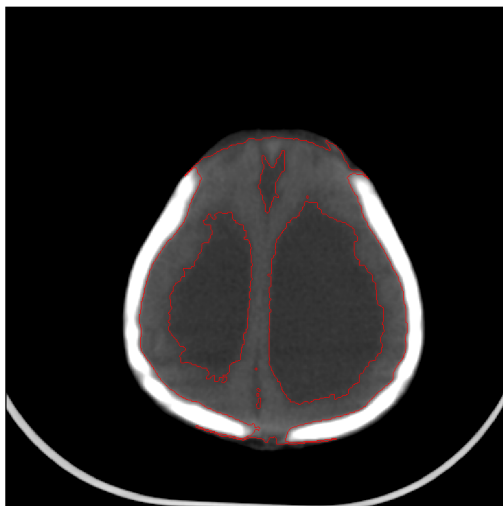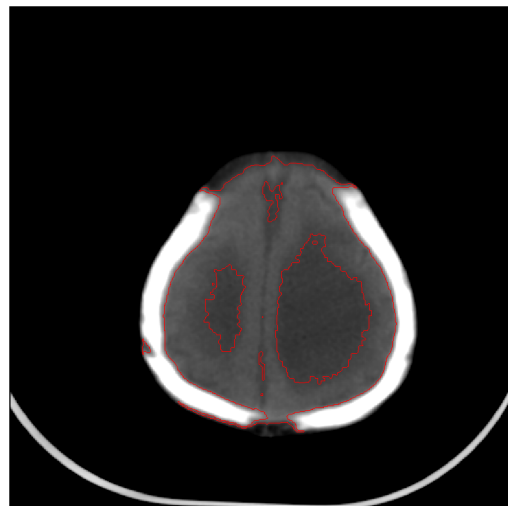(xix) $Z = 17$
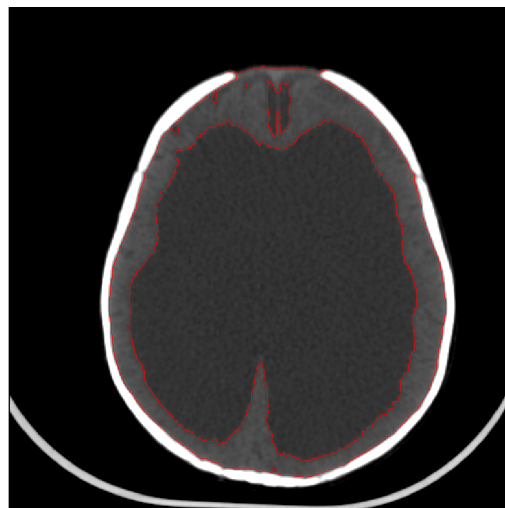
(xx) $Z = 18$
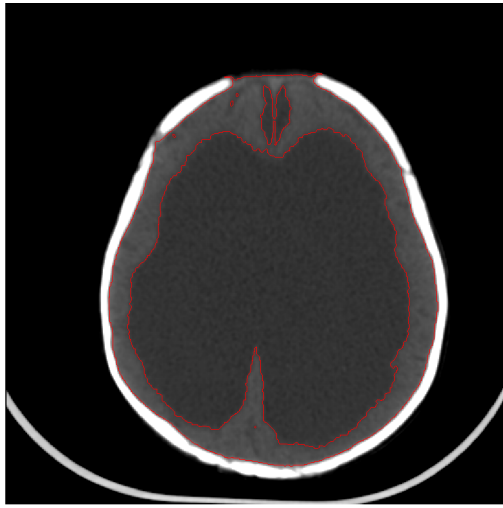
(xxi) $Z = 19$
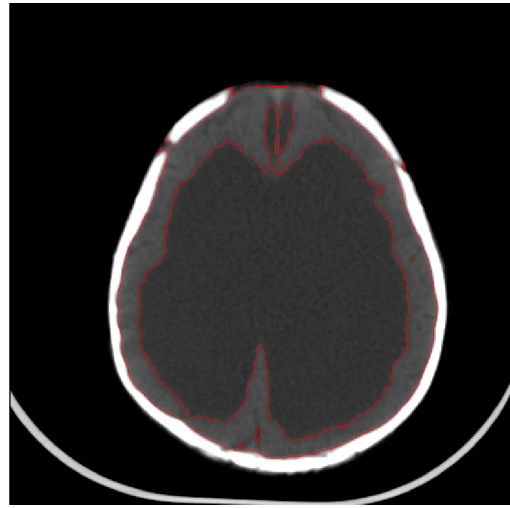
(xxii) $Z = 20$

(xxiii) $Z = 21$

(xxiv) $Z = 22$

(xxv) $Z = 23$

(xxvi) $Z = 24$

(xxvii) $Z = 25$
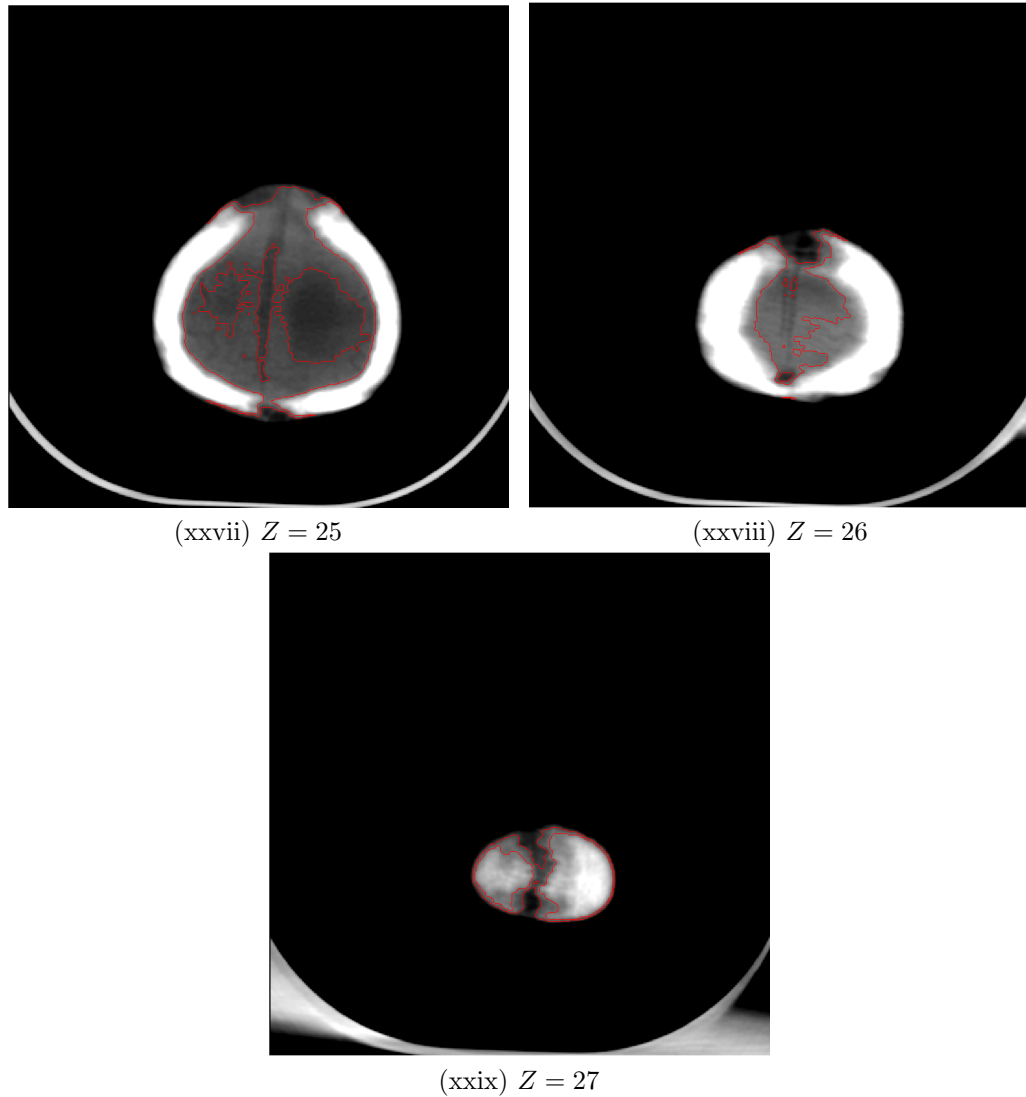
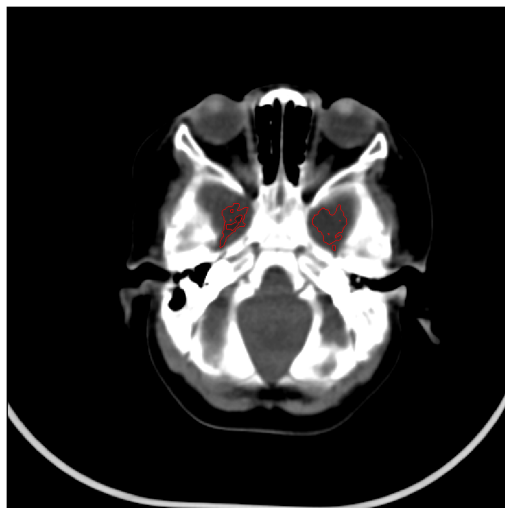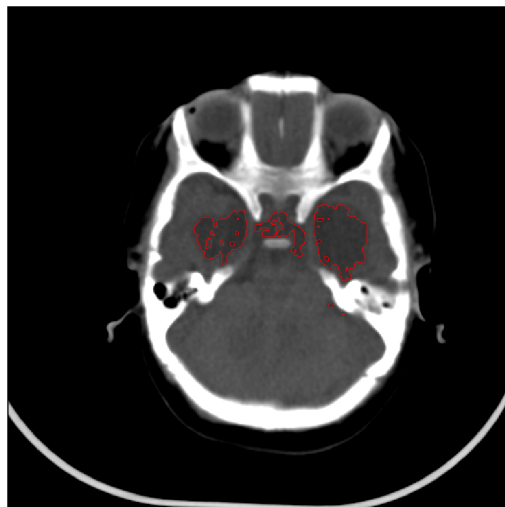(xxviii) $Z = 26$

(xxix) $Z = 27$

Figure 4.-2: Viewing the completed segmentation as a series of projections gives a better insight as to the difficulties the level set algorithm has with tracing out areas of the brain. As seen in the lower slices, particulary Figures 4.2iii- 4.2vii the level set has difficulty of separating non-brain tissue areas that have the same central pixel intensity range, $T \pm \epsilon$. This is due to the streak effect being present in these scans as well as neighboring tissue with similar Hounsfield unit value as brain matter.
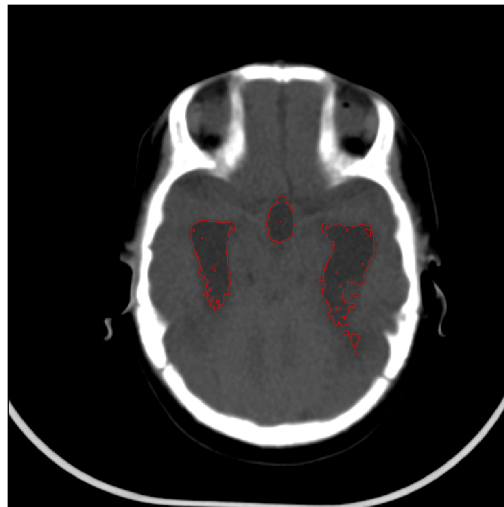
(xxx) $Z = 1$

(xxxi) $Z = 2$

(xxxii) $Z = 3$

(xxxiii) $Z = 4$

(xxxiv) $Z = 5$
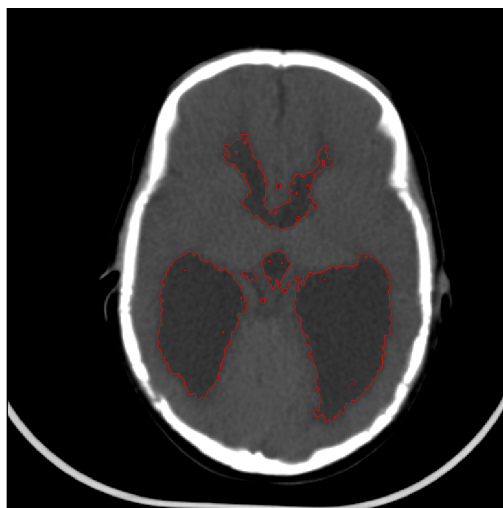
(xxxv) $Z = 6$
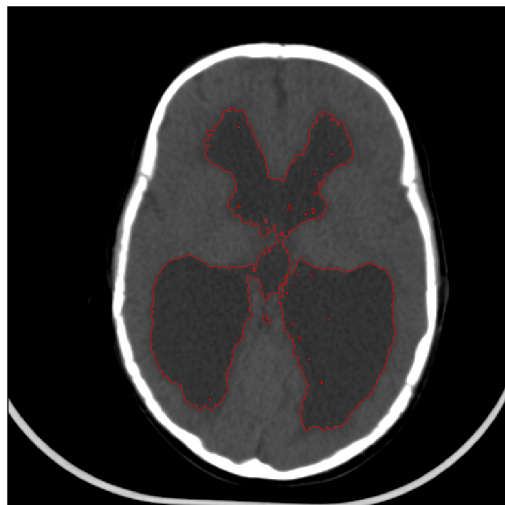
(xxxvi) $Z = 7$
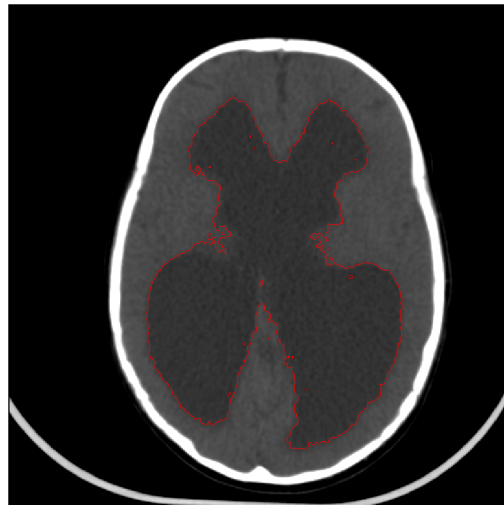
(xxxvii) $Z = 8$
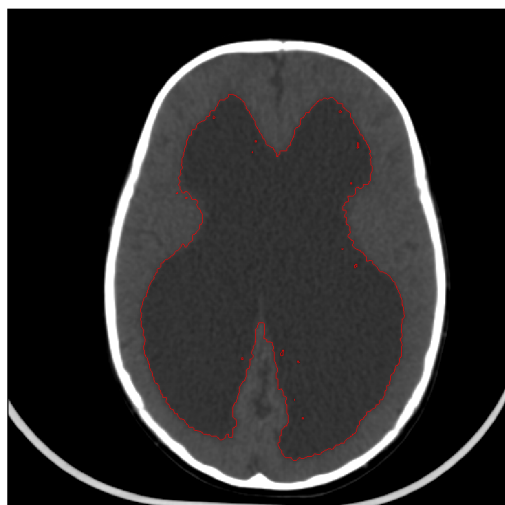
(xxxviii) $Z = 9$

(xxxix) $Z = 10$

(xl) $Z = 11$
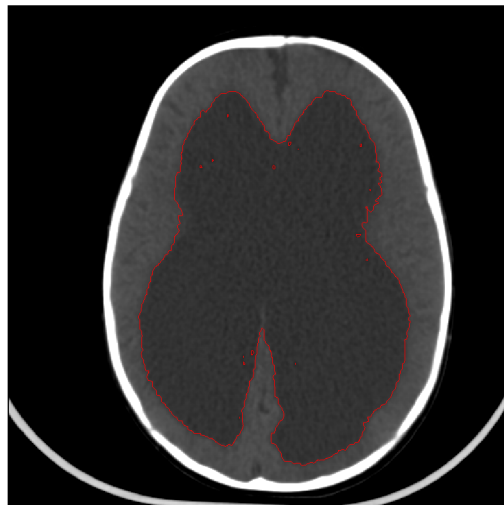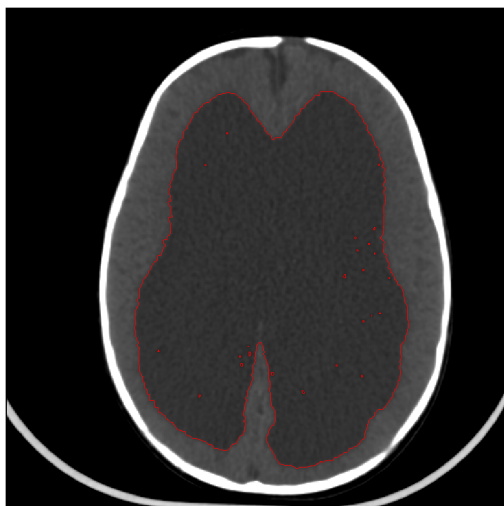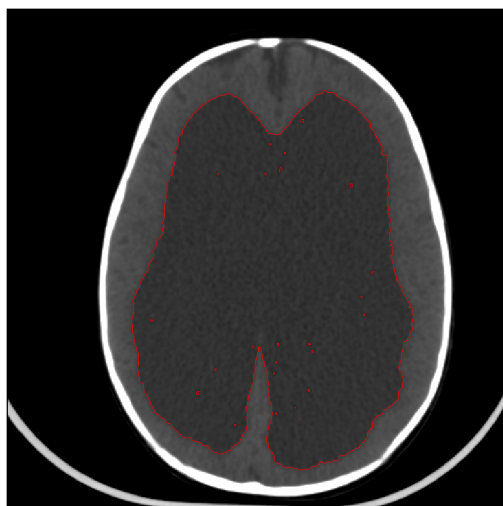
(xli) $Z = 12$
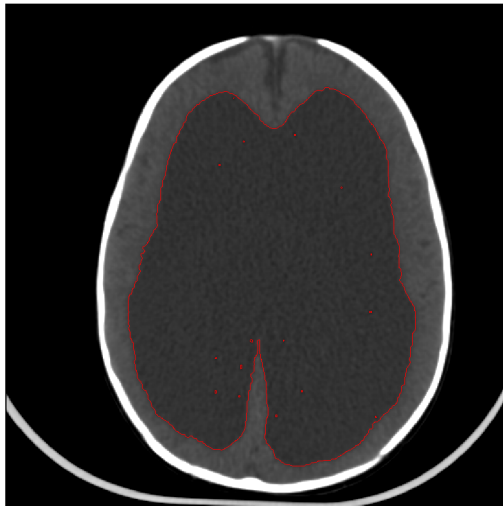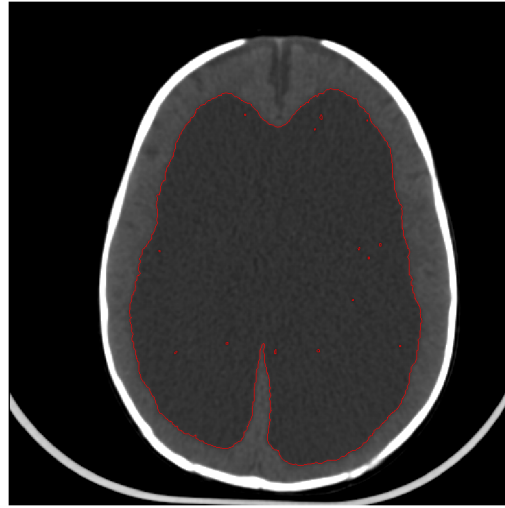
(xlii) $Z = 13$

(xliii) $Z = 14$
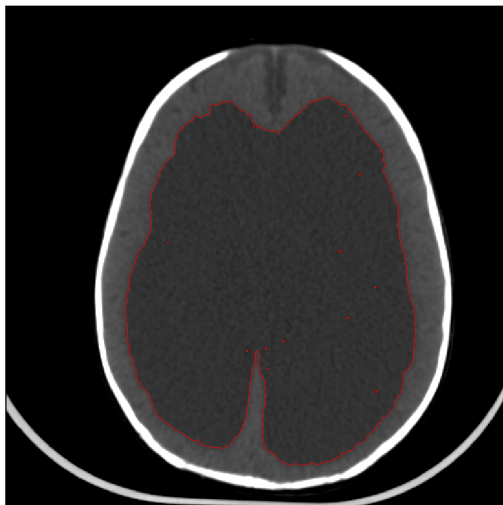
(xliv) $Z = 15$
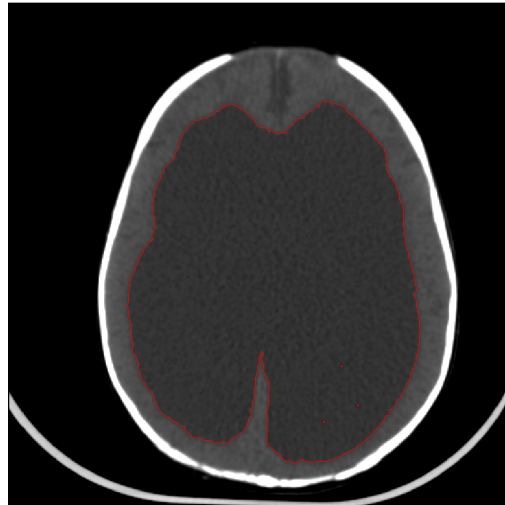
(xlv) $Z = 16$
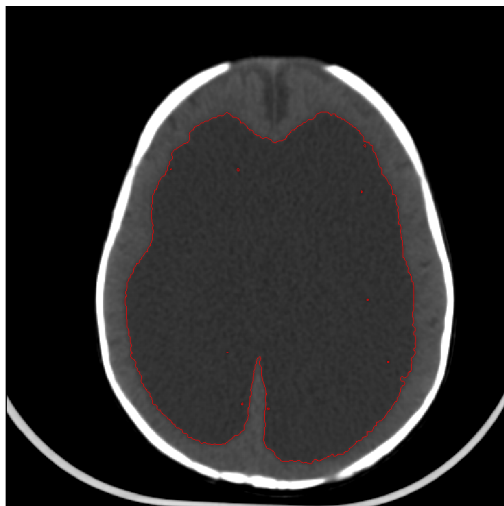
(xlvi) $Z = 17$
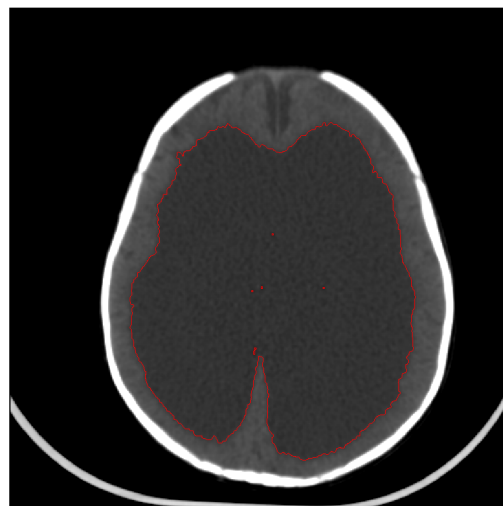
(xlvii) $Z = 18$
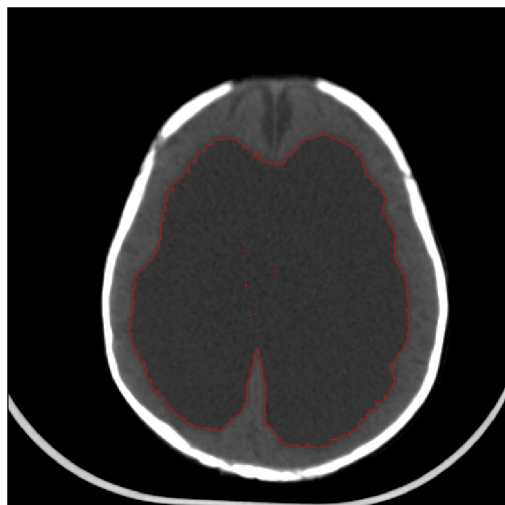
(xlviii) $Z = 19$
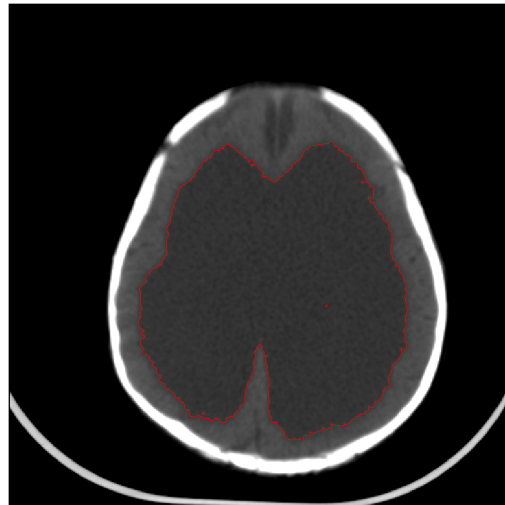
(xlix) $Z = 20$
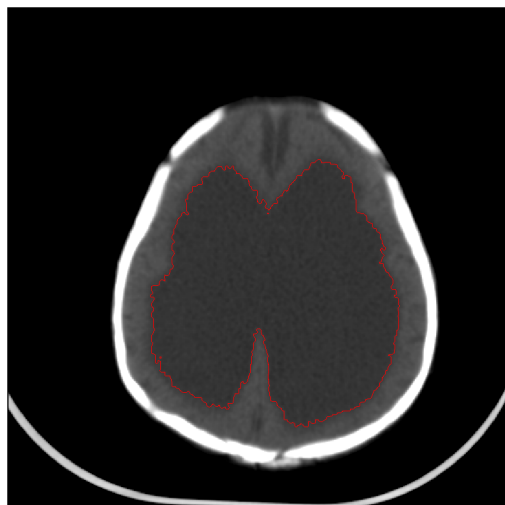
(l) $Z = 21$
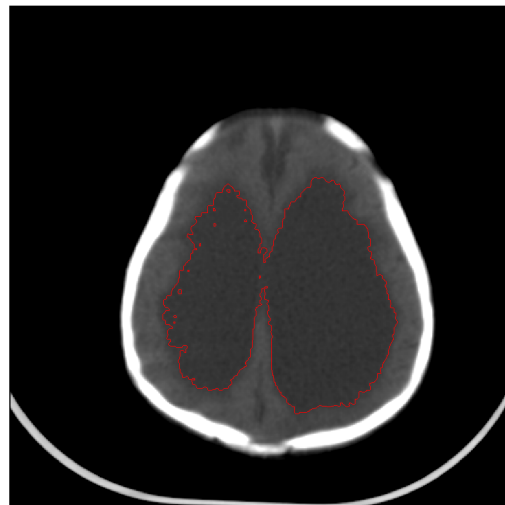
(li) $Z = 22$

(lii) $Z = 23$

(liii) $Z = 24$

(liv) $Z = 25$

(lv) $Z = 26$

(lvi) $Z = 27$
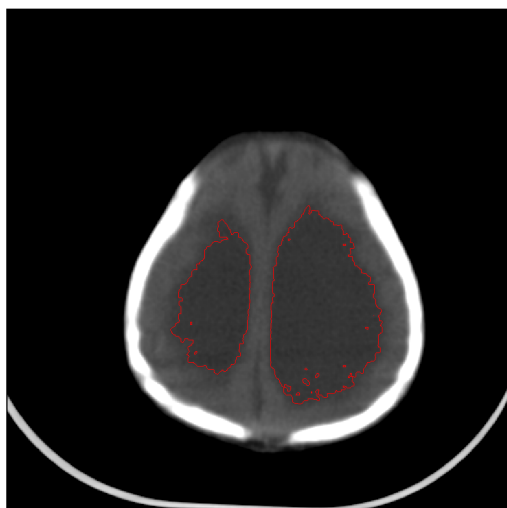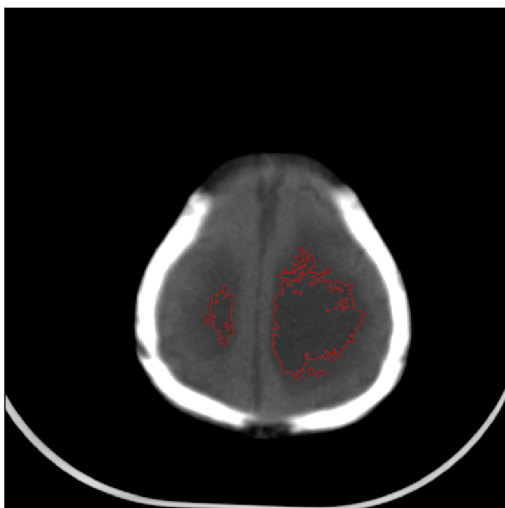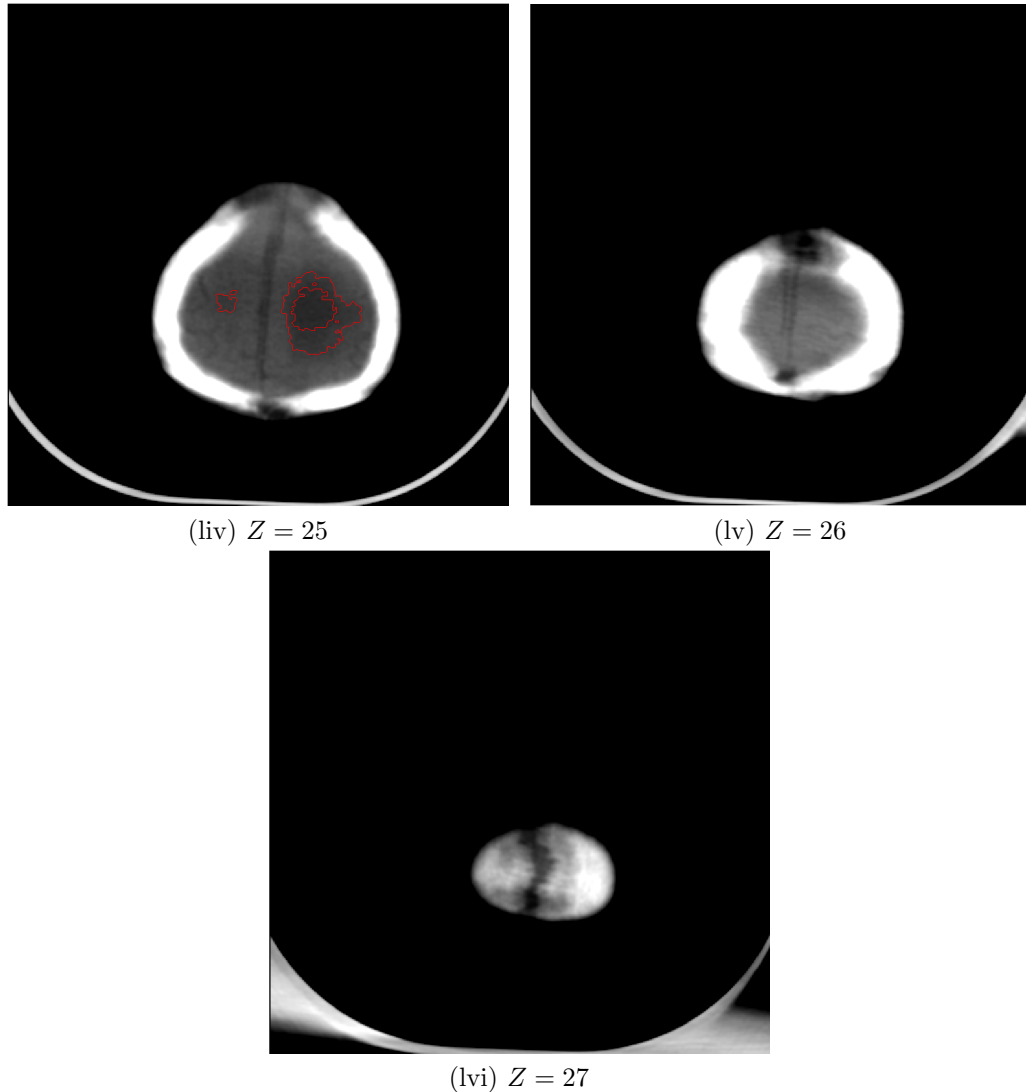
Figure 4.-6: The level set successfully delineated regions of CSF as seen in the images above. The volume was calculated to be 823.41 cm^3 which corresponds to less than 1% error with respect to 830 cm^3 obtained via the stereo investigator. The level set has difficulty with areas near the base of the skull as evidenced previously in the brain tissue segmentation. Again, this is due to the streak effect being present in the scan data as well as area misclassification. Segmented areas of small, archipelago-like regions in 4.-3xl- 4.-4xlvii are due to voxels intensities that are not in $T \pm \epsilon$ range.
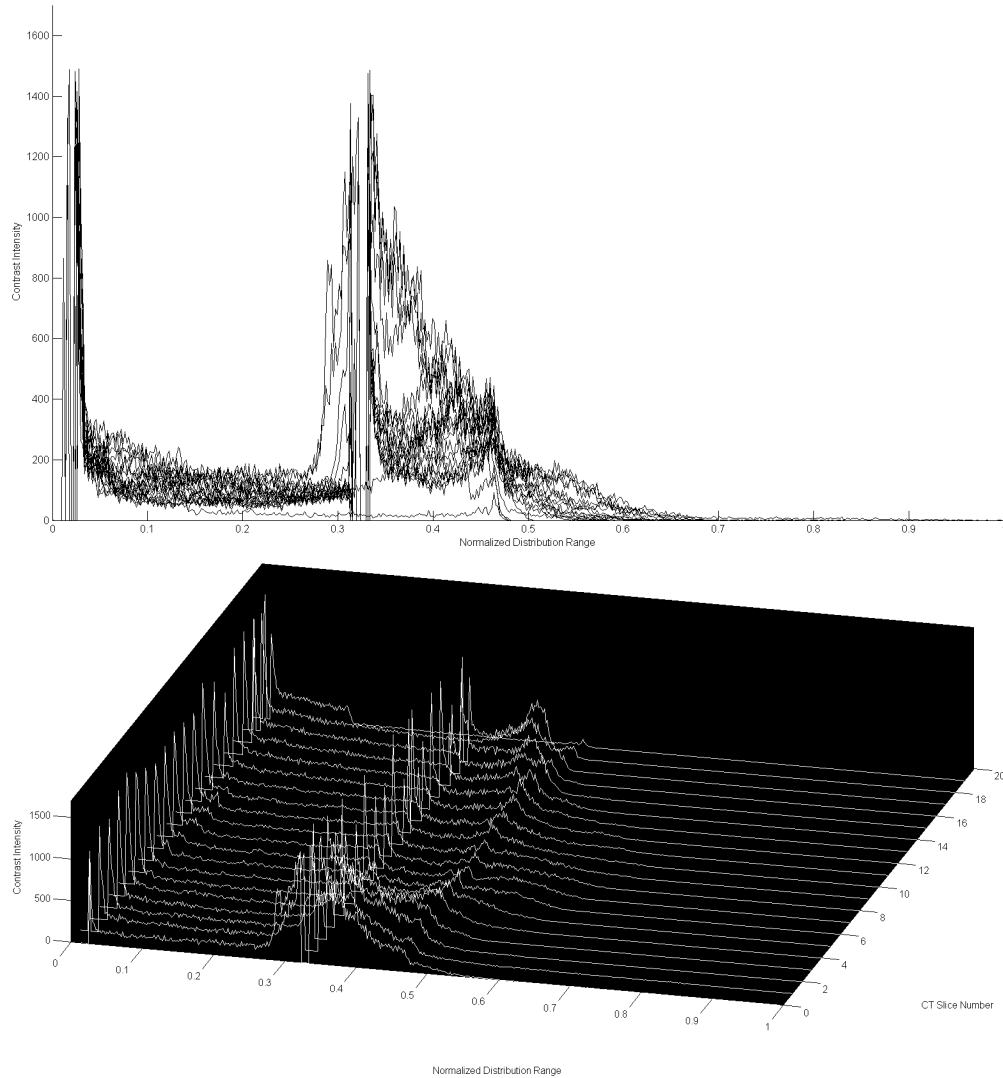
Figure 4.-5: A contrast intensity histogram is shown in the two images above for data set 18. The sensitivity analysis that was done for initial parameters, T, ϵ, in this section was based off the values in the non-normalized distribution range of this plot for each CT slice. The percent perturbations to T and ϵ were determined by examining the distribution range at the quarter, half and three-quarter slice locations in the data set.

Chapter 5

Conclusions

Segmentation of anatomical objects is a critical task in the analysis of medical image data. Furthermore, volume segmentation of medical images has great potential in assisting physicians with making the correct diagnosis and administering proper treatment. Also, accurate segmentation is vital in the planning stages of surgical procedures where it's used as both a quantifier and visualization tool. In this thesis we prioritize segmenting cerebrospinal fluid and brain tissue in patients with hydrocephalus. The data was provided courtesy of Dr. Steven Schiff, Director of Penn Center for Neural Engineering. Because CT scans offer many advantages over MRI machines, 1.2.1, and the general lack of availability of MRI technology in developing countries, we focus our efforts on delineating CT images 1.2. This thesis describes a method for segmenting medical image data via three dimensional level set algorithm. The complex nature, i.e. topological changes due to loculated regions, associated with segmenting in 3D make this an especially difficult problem. The approach is based on the popular level set method which is a subset of geometric deformable model techniques in image analysis. The structure of this approach, i.e. an Eulerian formulation, solves many of the encountered problems that other methods are unable to overcome. Additionally, the algorithm of choice is propagated forward in time in such a manner so that both stability and convergence are guaranteed from sections 3.5 and 3.7. The level set algorithm was developed in Matlab and the computations were performed on the Penn State Lino-X Series Clusters due to limited processing power and available physical memory. The algorithm was tested on five data sets and the segmented

CSF and brain tissue volumes were compared to the ground truth data obtained via stereo investigator. Errors of less than 1% were observed for CSF and 1.5% for brain tissue. A complete set of segmented images, CSF and brain tissue, is provided in section 4.3.1. Robustness of the initial parameters was demonstrated using a sensitivity analysis in section 4.4. Graceful behavior was observed for the CSF volume segmentation: 4% error with a 1.5% disturbance in T, 2.27% error with a 15% disturbance in ϵ. Brain tissue segmentations were more error prone to disturbances in both parameters: 15.79% error with a 1.5% disturbance in T, 16.34% error with a 15% disturbance in ϵ. This showed that the algorithm was highly reliable in reporting CSF volumes while brain tissue segmentations could be made more consistent with future research into the initialization phase.

5.1 Summary of Contributions

5.1.1 Method for Segmenting CSF and Brain Tissue in 3D

The level set architecture was selected due to its advantages over other methods that were reviewed in sections 1.4 and 1.2.4. Mainly, the level set was chosen based on its ability to handle topological changes such as splitting and merging of surfaces, the ease of performing stable numerical computations on a Cartesian grid without the need to parametrize surface contours and the trivial extension of the 2-D problem to n-D. This method was further automated by only requiring two parameters and a seed surface for initialization. The parameters are chosen by examining contrast intensity histograms for each data sets and choosing groups of voxels that represent the desired target region at three different locations as describe in section 3.10.

5.1.2 Results Verification

Five different data sets were segmented for both CSF and brain tissue. Volume calculations obtained from the segmented results were compare to the ground truth values. It was demonstrated that the algorithm was highly successful in delineating both regions within the CT scans for all of the data sets. These results further

validate our choice of the level set method and demonstrate its vast capabilities in image segmentation for a variety of applications both in and outside of medicine.

5.1.3 Demonstration of Parameter Robustness

An automated level set algorithm is of limited usefulness if initialization parameters do not demonstrate robustness to image artifacts such as noise, shading and partial volume effect. There are also many other factors that affect the end result of which user induced error in choosing initial parameters is of most significance. For this reason, we performed a sensitivity study in which perturbations to initial parameters were made to view the effect on the segmented volumes. It is shown that even relatively large changes in both parameters do not noticeably affect the CSF volume segmentation; however, any change in either parameter significantly alters the brain tissue segmentation.

5.2 Recommendations for Future Research

5.2.1 Speed Function

The speed function, D, we use in this thesis is adopted from the work of Lefohn, Whitaker and Cates in [79]. The model is based on a central voxel intensity and intensity deviation. We choose this based on the simplicity of the scalar speed function and did not expermient with other models from literature. Future work could examine the effect of changing the speed function formulation using previously established models, [86], [78], [87], [88], [89], [38], or by defining a new approach. Caselles in [86] and Mallad et al. in [78] proposed a model which couples curve evolution with image data and has shown promise in segmenting images with good contrast. This was improved in [87], [88] with the use of an energy minimization in the definition of the speed function which allowed the contour to "pull" back if a segmentation boundary had been crossed. Siddiqi further expanded on their formulation in [89] which addressed the problem of passing through boundary gaps. Elsa et al., [31], describe use of speed functions with regularizers which add prior information during the segmentation and aid in preventing errors when the speed function is defined solely in terms of intensity.

5.2.2 Discretization

In this thesis we use a first-order forward Euler method with upwind differencing to propagate the level set. This can be improved by using a more accurate approximation for derivatives of ϕ. The idea of upwinding still remains a critical part in deciding which derivative will be used; however, we focus our effort to improving the derivative itself. In [90], Harten et al. introduced the notion of essentially non-oscillatory (ENO) polynomial interpolation of data for the numerical solution of hyperbolic conservation laws. The basis of the theory was to compute numerical flux functions using smooth polynomial interpolation [60]. Shu and Osher later improved on the numerical implementation in [91] and [92], in which numerical flux functions were created from a divided difference table of the pointwise data [60]. This method was extended to Hamilton-Jacobi equations by Osher and Sethian in [57] which allows for extension of the first-order accurate upwind differencing to higher-order spatial accuracy. This Hamilton-Jacobi ENO provides us the the ability to discretize spatial terms in Equation 3.1 to fifth-order accuracy as opposed to the forward Euler method we use that is only first-order accurate. Temporal discretization can most of the time be satisfied using the forward Euler method because temporal truncation errors induce less instability in the solution than spatial errors. In [93] Min compares the forward Euler, second order Runge-Kutta and a Gauss-Seidel iteration of the forward Euler as temporal discretization methods. In [91] Shu and Osher proposed total variation diminishing Runge-Kutta methods to decrease temporal truncation errors via *method of lines* which assumes that spatial and temporal discretization are independent.

5.2.3 Accuracy Metrics and Sensitivity Analysis

Segmentation algorithms, moreover algorithms in general, require a systematic evaluation to fully understand its strengths, limitations and potential applications [80]. In this thesis we analyze the performance of the level set algorithm by comparing its results to the ground truth volume segmentations performed via stereo investigator. In general, performance evaluation is a difficult task because a predefined, standard set of metrics does not exist for all algorithms and applications. In [94], Udupa et al. argue for a performance metric based on accuracy, precision and

computational efficiency. A comparison of the segmented region's and the ground truth region's overlap via distance metric, e.g. Hausdorff or root mean square, could provide further insight into the accuracy of the algorithm. Other means of characterizing overlap include similarity measures such as *cardinality of the intersection* and the *total correct fraction* [80]. In this thesis we tested the sensitivity of the two initialization parameters on the segmented volumes. More complex studies could be performed to determine the most efficient method of selecting initial parameters and whether the process can be fully automated. In [95], Liasis and Stavrou present a method for optimizing the initialization in segmenting satellite images via k-mean classifier.

5.2.4 GPU-based Level Set

Choosing the method for implementing the level set algorithm can be a difficult process. As with most computer programing challenges, there are many trade offs one has to consider. These include the programing complexity, computational efficiency and visualization capabilities. We chose the Matlab environment in this thesis because of its ease of implementation for the level set and extensive graphics options. The level set architecture also allows for parallelization which increases processing capabilities. Future work could focus on rewriting the algorithm to take advantage of Matlab's parallel processing toolbox. Furthermore, using general purpose computation on graphics processing units (GPU) instead of the central processing unit would drastically reduce the segmentation time [79], [70]. Lefohn et al. in [79] present a GPU based algorithm for solving and visualizing level set solutions at interactive rates and report a reduction in computation time of more than an order of magnitude when compared to a CPU architecture. In [70], Mostofi developed a 3D shared memory optimization of the level set algorithm programmed using the compute unified device architecture on a NVIDIA GPU. Segmentations obtained using this implementation were achieved at least two orders of magnitude faster than with a Matlab environment. Cates et al. also have shown that implementing a 3D level set via GPU has significant advantages over a CPU environment using an innovative mapping for GPU memory management [80]. Also, they describe how the interactive rates level set algorithm allows for user

immediate feedback which provides for free parameter tunning and shape control of the model in real time.

Supplemental Materials

A.1 2D Level Set Equations

$$\frac{\partial \phi}{\partial t} = -|\nabla \phi| \left[\alpha D(I) + (1 - \alpha) \nabla \cdot \frac{\nabla \phi}{|\nabla \phi|} \right] \tag{A.1}$$

$$
\begin{aligned}
D_x &= (\phi_{i+1,j} - \phi_{i-1,j})/2 & D_x^+ &= \phi_{i+1,j} - \phi_{i,j} & D_x^- &= \phi_{i,j} - \phi_{i-1,j} \\
D_y &= (\phi_{i,j+1} - \phi_{i,j-1})/2 & D_y^+ &= \phi_{i,j+1} - \phi_{i,j} & D_y^- &= \phi_{i,j} - \phi_{i,j-1}
\end{aligned}
$$
$$\tag{A.2}$$

$$\nabla \phi_{\max} = \begin{bmatrix} \sqrt{\max(D_x^+, 0)^2 + \max(-D_x^-, 0)^2} \\[2em] \sqrt{\max(D_y^+, 0)^2 + \max(-D_y^-, 0)^2} \end{bmatrix} \tag{A.3}$$

$$\nabla \phi_{\min} = \begin{bmatrix} \sqrt{\min(D_x^+, 0)^2 + \min(-D_x^-, 0)^2} \\[2em] \sqrt{\min(D_y^+, 0)^2 + \min(-D_y^-, 0)^2} \end{bmatrix} \tag{A.4}$$

$$\nabla\phi = \begin{cases} ||\nabla\phi_{\max}||_2 & \text{if } F_{i,j} > 0 \\ ||\nabla\phi_{\min}||_2 & \text{if } F_{i,j} < 0 \end{cases} \tag{A.5}$$

$$D_x^{+y} = (\phi_{i+1,j+1,k} - \phi_{i-1,j+1,k})/2 \qquad D_x^{-y} = (\phi_{i+1,j-1,k} - \phi_{i-1,j-1,k})/2$$
$$D_y^{+x} = (\phi_{i+1,j+1,k} - \phi_{i+1,j-1,k})/2 \qquad D_y^{-x} = (\phi_{i-1,j+1,k} - \phi_{i-1,j-1,k})/2$$

$$\tag{A.6}$$

$$\mathbf{n}^+ = \begin{bmatrix} \dfrac{D_x^+}{\sqrt{(D_x^+)^2 + \left(\frac{D_y^{+x} + D_y}{2}\right)^2}} \\[4mm] \dfrac{D_y^+}{\sqrt{(D_y^+)^2 + \left(\frac{D_x^{+y} + D_x}{2}\right)^2}} \end{bmatrix} \tag{A.7}$$

$$\mathbf{n}^- = \begin{bmatrix} \dfrac{D_x^-}{\sqrt{(D_x^-)^2 + \left(\frac{D_y^{-x} + D_y}{2}\right)^2}} \\[4mm] \dfrac{D_y^-}{\sqrt{(D_y^-)^2 + \left(\frac{D_x^{-y} + D_x}{2}\right)^2}} \end{bmatrix} \tag{A.8}$$

$$H = \frac{1}{2}\nabla \cdot \frac{\nabla\phi}{|\nabla\phi|} = \frac{1}{2}((\mathbf{n}_x^+ - \mathbf{n}_x^-) + (\mathbf{n}_y^+ - \mathbf{n}_y^-))) \tag{A.9}$$

Bibliography

[1] RAIC, Z. (2011) "On Surface Estimation of a 2D Analytic Topological Manifold via Sequential Monte Carlo Method," Penn State Course - AERSP 597E: Estimation Theory.

[2] MANDELL, J. G., J. W. LANGELAAN, A. G. WEBB, and S. J. SCHIFF (2011) "Volumetric Brain Analysis in Neurosurgery: I. Particle Filter Segmentation of Brain and Cerebrospinal Fluid Growth Dynamics from MRI and CT Images," *Journal of Neurosurgery: Pediatrics.*

[3] (2006) *International Society for Magnetic Resonance in Medicine (ISMRM, Seattle, Washington, USA May 2006)*, Global Healthcare Challenges.
URL http://cds.ismrm.org/ismrm-2006/files/00002.pdf

[4] WORLD HEALTH ORGANIZATION (2010) *Medical Devices: Managing the Mismatch : An Outcome of the Priority Medical Devices project.*, World Health Organization Geneva.
URL http://whqlibdoc.who.int/publications/2010/9789241564045_eng.pdf

[5] HESS, C. and D. PURCELL (2012) "Exploring the Brain: Is CT or MRI Better for Brain Imaging?" .
URL http://blog.radiology.ucsf.edu/neuroradiology/exploring-the-brain-is-ct-or-mri-better-for-brain-imaging

[6] AGGARWAL, L. and N. SHARMA (2010) "Automated medical image segmentation techniques," *Journal of Medical Physics*, **35**(1), pp. 3–14, http://www.jmp.org.in/article.asp?issn=0971-6203;year=2010;volume=35;issue=1;spage=3;epage=14;aulast=Sharma;t=6.
URL http://www.jmp.org.in/article.asp?issn=0971-6203;year=2010;volume=35;issue=1;spage=3;epage=14;aulast=Sharma;t=6

[7] NATIONAL INSTITUTE OF NEUROLOGICAL DISORDERS AND STROKE (2008) *Hydrocephalus Fact Sheet, Tech. Rep. 08-385*, National Institute of Health.

URL `http://www.ninds.nih.gov/disorders/hydrocephalus/detail_hydrocephalus.htm`

[8] MANDELL, J. G., A. V. KULKARNI, B. C. WARF, and S. J. SCHIFF (2011) "Volumetric Brain Analysis in Neurosurgery: II. Brain and CSF Volumes Discriminate Neurocognitive Outcomes in Hydrocephalus," *Journal of Neurosurgery: Pediatrics*.

[9] FLETCHER, E., B. SINGH, D. HARVEY, O. CARMICHAEL, and C. DE-CARLI (2012) "Adaptive image segmentation for robust measurement of longitudinal brain tissue change," in *Engineering in Medicine and Biology Society (EMBC), 2012 Annual International Conference of the IEEE*, pp. 5319–5322.

[10] MANDELL, J. G., T. NEUBERGER, C. S. DRAPACA, A. G. WEBB, and S. J. SCHIFF (2010) "The dynamics of brain and cerebrospinal fluid growth in normal versus hydrocephalic mice," *Journal of Neurosurgery: Pediatrics*, **6**(1), pp. 1–10, pMID: 20593980, `http://thejns.org/doi/pdf/10.3171/2010.4.PEDS1014`.
URL `http://thejns.org/doi/abs/10.3171/2010.4.PEDS1014`

[11] SINGER, O., J. MELBER, E. HATTINGEN, A. JURCOANE, F. KEIL, T. NEUMANN-HAEFELIN, and J. KLEIN (2012) "MR volumetric changes after diagnostic CSF removal in normal pressure hydrocephalus," *Journal of Neurology*, **259**(11), pp. 2440–2446.
URL `http://dx.doi.org/10.1007/s00415-012-6525-3`

[12] KULKARNI, A. (2010) "Quality of life in childhood hydrocephalus: a review," *Child's Nervous System*, **26**(6), pp. 737–743.
URL `http://dx.doi.org/10.1007/s00381-010-1131-0`

[13] WEESE, J., M. KAUS, C. LORENZ, S. LOBREGT, R. TRUYEN, and V. PEKAR (2001) "Shape Constrained Deformable Models for 3D Medical Image Segmentation," in *Information Processing in Medical Imaging* (M. Insana and R. Leahy, eds.), vol. 2082 of *Lecture Notes in Computer Science*, Springer Berlin Heidelberg, pp. 380–387.
URL `http://dx.doi.org/10.1007/3-540-45729-1-38`

[14] STRAPP, A. (2010) *The Feasibility of Utilizing Sonographic Image Segmentation to Evaluate Axillary Lymph Nodes: Automated Computer Software vs. Manual Segmentation*, Master's thesis, The Ohio State University.

[15] McINERNEY, T. and D. TERZOPOULOS (1996) "Deformable models in medical image analysis," in *Mathematical Methods in Biomedical Image Analysis, 1996., Proceedings of the Workshop on*, pp. 171–180.

[16] Seong, W., E.-J. Kim, and J.-W. Park (2005) "Automatic Segmentation Technique Without User Modification for 3D Visualization in Medical Images," in *Computational and Information Science* (J. Zhang, J.-H. He, and Y. Fu, eds.), vol. 3314 of *Lecture Notes in Computer Science*, Springer Berlin Heidelberg, pp. 595–600.
URL http://dx.doi.org/10.1007/978-3-540-30497-5-93

[17] Lakare, S. (2000) "3D Segmentation Techniques for Medical Volumes," .
URL http://cs.sunysb.edu/mueller/teaching/cse616/sarangRPE.pdf

[18] Toennies, K. (2012) "Feature Detection," in *Guide to Medical Image Analysis*, Advances in Computer Vision and Pattern Recognition, Springer London, pp. 147–169.
URL http://dx.doi.org/10.1007/978-1-4471-2751-2_5

[19] Nakhjavanlo, B., T. Ellis, P. H. Soan, and J. Dehmeshki (2011) "3D Medical Image Segmentation Using Level Set Models and Anisotropic Diffusion," in *Signal-Image Technology and Internet-Based Systems (SITIS), 2011 Seventh International Conference on*, pp. 403–408.

[20] Chen, Y.-T. (2012) "Brain tumor detection using three-dimensional Bayesian level set method with volume rendering," in *Wavelet Analysis and Pattern Recognition (ICWAPR), 2012 International Conference on*, pp. 158–163.

[21] Ukwatta, E., J. Awad, A. Ward, D. Buchanan, G. Parraga, and A. Fenster (2011) "Coupled level set approach to segment carotid arteries from 3D ultrasound images," in *Biomedical Imaging: From Nano to Macro, 2011 IEEE International Symposium on*, pp. 37–40.

[22] Whitaker, R. T. (1994), "Volumetric deformable models: active blobs," .
URL http://dx.doi.org/10.1117/12.185173

[23] McInerney, T. and D. Terzopoulos (1996) "Deformable models in medical image analysis: a survey," *Med Image Anal*, **1**(2), pp. 1–108.

[24] Angelini, E., Y. Jin, and A. Laine (2005) "State of the Art of Level Set Methods in Segmentation and Registration of Medical Imaging Modalities," in *Handbook of Biomedical Image Analysis* (J. Suri, D. Wilson, and S. Laxminarayan, eds.), Topics in Biomedical Engineering International Book Series, Springer US, pp. 47–101.
URL http://dx.doi.org/10.1007/0-306-48608-3-2

[25] Sethian, J. A. (1990) "Numerical algorithms for propagating interfaces: Hamilton-Jacobi equations and conservation laws," *Journal of Differential Geometry*, **31**(1), pp. 131–161.

[26] PHAM, D. L., C. XU, and J. L. PRINCE (2000) "A Survey of Current Methods in Medical Image Segmentation," *Annual Review of Biomedical Engineering*, **2**(1), pp. 315–337, pMID: 11701515.
URL http://www.annualreviews.org/doi/abs/10.1146/annurev.bioeng.2.1.315

[27] PAL, N. and S. PAL (1993) "A review on image segmentation techniques," *Pattern Recognition*, **26**(9), pp. 1277–1294.
URL http://www.isical.ac.in/~sankar/paper/PR_93_NRP_SKP.PDF

[28] BANIK, S., R. M. RANGAYYAN, and G. S. BOAG (2009) "Landmarking and Segmentation of 3D CT Images," *Synthesis Lectures on Biomedical Engineering*, **4**(1), pp. 1–170.

[29] ERDT, M., S. STEGER, and G. SAKAS (required) "Regmentation: A New View of Image Segmentation and Registration," *Journal of Radiation Oncology Informatics*, **4**(1), pp. 1–23.

[30] WITHEY, D. J. and Z. J. KOLES (2008) "A Review of Medical Image Segmentation: Methods and Available Software," *International Journal of Bioelectromagnetism*, **10**(3), pp. 125–148.

[31] ANGELINI, E., Y. JIN, and A. LAINE (2005) "State of the Art of Level Set Methods in Segmentation and Registration of Medical Imaging Modalities," in *Handbook of Biomedical Image Analysis* (J. Suri, D. Wilson, and S. Laxminarayan, eds.), Topics in Biomedical Engineering International Book Series, Springer US, pp. 47–101.
URL http://dx.doi.org/10.1007/0-306-48608-3_2

[32] CANNY, J. (1986) "A Computational Approach to Edge Detection," *Pattern Analysis and Machine Intelligence, IEEE Transactions on*, **PAMI-8**(6), pp. 679–698.

[33] BÄHNISCH, C., P. STELLDINGER, and U. KÖTHE (2009) "Fast and Accurate 3D Edge Detection for Surface Reconstruction," in *Pattern Recognition* (J. Denzler, G. Notni, and H. Se, eds.), vol. 5748 of *Lecture Notes in Computer Science*, Springer Berlin Heidelberg, pp. 111–120.
URL http://hci.iwr.uni-heidelberg.de/publications/mip/techrep/baehnisch_09_fast.pdf

[34] YAGE-FABRA, J., S. ONTIVEROS, R. JIMNEZ, S. CHITCHIAN, G. TOSELLO, and S. CARMIGNATO (2013) "A 3D edge detection technique for surface extraction in computed tomography for dimensional metrology applications," *CIRP Annals - Manufacturing Technology*, **62**(1), pp. 531 – 534.

URL http://www.sciencedirect.com/science/article/pii/S0007850613000176

[35] Yu-qian, Z., G. Wei-hua, C. Zhen-cheng, T. Jing-tian, and L. Ling-yun (2005) "Medical Images Edge Detection Based on Mathematical Morphology," in *Engineering in Medicine and Biology Society, 2005. IEEE-EMBS 2005. 27th Annual International Conference of the*, pp. 6492–6495.

[36] Jian, C., T. Li, J. Hua, Z. Wumei, Z. Ying, and Y. Bin (2012) "Volume morphology and its application in 3-D image speckle noise suppressing," in *Fuzzy Systems and Knowledge Discovery (FSKD), 2012 9th International Conference on*, pp. 2023–2026.

[37] Yamashita, F., M. Sasaki, S. Takahashi, H. Matsuda, K. Kudo, S. Narumi, Y. Terayama, and T. Asada (2010) "Detection of changes in cerebrospinal fluid space in idiopathic normal pressure hydrocephalus using voxel-based morphometry," *Neuroradiology*, **52**(5), pp. 381–386.
URL http://dx.doi.org/10.1007/s00234-009-0610-z

[38] Xu, C., D. Pham, and J. Prince (2000) "Medical Image Segmentation Using Deformable Models," in *Handbook of Medical Imaging - Volume 2: Medical Image Processing and Analysis* (J. Fitzpatrick and M.Sonka, eds.), SPIE Press, pp. 129–174.

[39] Alfiansyah, A. (2011) "Deformable Models and Level Sets in Image Segmentation," in *Medical Image Processing* (G. Dougherty, ed.), Biological and Medical Physics, Biomedical Engineering, Springer New York, pp. 59–87.
URL http://dx.doi.org/10.1007/978-1-4419-9779-1_4

[40] Chan, T. F. and J. Shen (2005) *Image Processing and Analysis*, Society for Industrial and Applied Mathematics, http://epubs.siam.org/doi/pdf/10.1137/1.9780898717877.
URL http://epubs.siam.org/doi/abs/10.1137/1.9780898717877

[41] Li, Z. and J. Fan (2009) "Stochastic contour approach for automatic image segmentation." *Journal of Electronic Imaging*, **18**(4).
URL http://coitweb.uncc.edu/~jfan/JEI2009.pdf

[42] Besbes, O., N. Boujemaa, and Z. Belhadj (2008) "Stochastic image segmentation by combining region and edge cues," in *Image Processing, 2008. ICIP 2008. 15th IEEE International Conference on*, pp. 2288–2291.

[43] Lauric, A. and S. Frisken (2007) *Soft Segmentation of CT Brain Data*, Tech. Rep. TR-2007-3, Tufts University.

[44] Bezdek, J. C., L. O. Hall, and L. P. Clarke (1993) "Review of MR image segmentation techniques using pattern recognition," *Med Phys*, **20**(4), pp. 1033–1048.

[45] Park, J., S. M. Shontz, and C. S. Drapaca (2013) "A Combined Level Set/Mesh Warping Algorithm for Tracking Brain and Cerebrospinal Fluid Evolution in Hydrocephalic Patients," in *Image-Based Geometric Modeling and Mesh Generation* (Y. Zhang, ed.), vol. 3 of *Lecture Notes in Computational Vision and Biomechanics*, Springer Netherlands, pp. 107–141.
URL http://dx.doi.org/10.1007/978-94-007-4255-0_7

[46] Lemieux, L., A. Hammers, T. Mackinnon, and R. S. Liu (2003) "Automatic segmentation of the brain and intracranial cerebrospinal fluid in T1-weighted volume MRI scans of the head, and its application to serial cerebral and intracranial volumetry," *Magnetic Resonance in Medicine*, **49**(5), pp. 872–884.
URL http://dx.doi.org/10.1002/mrm.10436

[47] Tsunoda, A., H. Mitsuoka, H. Bandai, H. Arai, K. Sato, and J. Makita (2001) "Intracranial Cerebrospinal Fluid Distribution and its Postoperative Changes in Normal Pressure Hydrocephalus," *Acta Neurochirurgica*, **143**(5), pp. 493–499.
URL http://dx.doi.org/10.1007/s007010170079

[48] Hodel, J., A. Lebret, E. Petit, X. Leclerc, M. Zins, A. Vignaud, P. Decq, and A. Rahmouni (2013) "Imaging of the entire cerebrospinal fluid volume with a multistation 3D SPACE MR sequence: feasibility study in patients with hydrocephalus," *European Radiology*, **23**(6), pp. 1450–1458.
URL http://dx.doi.org/10.1007/s00330-012-2732-7

[49] Hodel, J., P. Besson, A. Rahmouni, E. Petit, A. Lebret, B. Grandjacques, O. Outteryck, M. Benadjaoud, A. Maraval, A. Luciani, J.-P. Pruvo, P. Decq, and X. Leclerc (2013) "3D mapping of cerebrospinal fluid local volume changes in patients with hydrocephalus treated by surgery: preliminary study," *European Radiology*, pp. 1–7.
URL http://dx.doi.org/10.1007/s00330-013-2990-z

[50] Poh, L., V. Gupta, A. Johnson, R. Kazmierski, and W. Nowinski (2012) "Automatic Segmentation of Ventricular Cerebrospinal Fluid from Ischemic Stroke CT Images," *Neuroinformatics*, **10**(2), pp. 159–172.
URL http://dx.doi.org/10.1007/s12021-011-9135-9

[51] Abdullah, A., A. Hirayama, S. Yatsushiro, M. Matsumae, and K. Kuroda (2013) "Cerebrospinal fluid image segmentation using spatial

fuzzy clustering method with improved evolutionary Expectation Maximization," in *Engineering in Medicine and Biology Society (EMBC), 2013 35th Annual International Conference of the IEEE*, pp. 3359–3362.

[52] ITO, M., K. SATO, M. FUKUMI, and I. NAMURA (2011) "Brain tissues segmentation for diagnosis of Alzheimer-type Dementia," in *Nuclear Science Symposium and Medical Imaging Conference (NSS/MIC), 2011 IEEE*, pp. 3847–3849.

[53] TSANG, O., A. GHOLIPOUR, N. KEHTARNAVAZ, K. GOPINATH, R. BRIGGS, and I. PANAHI (2008) "Comparison of tissue segmentation algorithms in neuroimage analysis software tools," in *Engineering in Medicine and Biology Society, 2008. EMBS 2008. 30th Annual International Conference of the IEEE*, pp. 3924–3928.

[54] GORTHI, S., J. THIRAN, and M. CUADRA (2011) "Comparison of energy minimization methods for 3-D brain tissue classification," in *Image Processing (ICIP), 2011 18th IEEE International Conference on*, pp. 57–60.

[55] KALAISELVI, T. and K. SOMASUNDARAM (2011) "Fuzzy c-means technique with histogram based centroid initialization for brain tissue segmentation in MRI of head scans," in *Humanities, Science Engineering Research (SHUSER), 2011 International Symposium on*, pp. 149–154.

[56] XIA, Y., J. WANG, S. EBERL, M. FULHAM, and D. FENG (2011) "Brain tissue segmentation in PET-CT images using probabilistic atlas and variational Bayes inference," in *Engineering in Medicine and Biology Society,EMBC, 2011 Annual International Conference of the IEEE*, pp. 7969–7972.

[57] OSHER, S. and J. A. SETHIAN (1988) "Fronts propagating with curvature dependent speed: algorithms based on Hamilton-Jacobi formulations," *Journal of Computational Physics*, **79**, pp. 12–49.

[58] SETHIAN, J. A. (1982) *An Analysis of Flame Propagation*, Ph.D. thesis, Dept. of Mathematics, University of California, Berkeley.

[59] SETHIAN, J. (1985) "Curvature and the evolution of fronts," *Communications in Mathematical Physics*, **101**(4), pp. 487–499.
URL http://dx.doi.org/10.1007/BF01210742

[60] OSHER, S. and R. P. FEDKIW (2003) *Level set methods and dynamic implicit surfaces*, Applied mathematical science, Springer, New York, N.Y.

[61] SETHIAN, J. A. (1999) "Fast Marching Methods," *SIAM Review*, **41**(2), pp. 199–235, http://epubs.siam.org/doi/pdf/10.1137/S0036144598347059.
URL http://epubs.siam.org/doi/abs/10.1137/S0036144598347059

[62] ——— (1999) "Advancing Interfaces: Level Set and Fast Marching Methods," in *Proceedings of the International Conference on Industrial and Applied Mathematics: Plenary Lectures.*

[63] POPOVICI, A. M. and J. A. SETHIAN (1998), "Three-dimensional travel-time computation using the Fast marching method," .
URL http://dx.doi.org/10.1117/12.323280

[64] SETHIAN, J. (1999) *Level Set Methods and Fast Marching Methods: Evolving Interfaces in Computational Geometry, Fluid Mechanics, Computer Vision, and Materials Science*, vol. 3 of *Cambridge Monographs on Applied and Computational Mathematics*, Cambridge University Press.

[65] SETHIAN, J. A. (1996) "Theory, Algorithms, and Applications of Level Set Methods for Propagating Interfaces," *Acta Numerica*, **5**, pp. 309–395.
URL http://journals.cambridge.org/article_S0962492900002671

[66] ——— (1996) "A Fast Marching Level Set Method for Monotonically Advancing Fronts," *Proc. Natl. Acad. Sci.*, **93**(4), pp. 1591–1595.

[67] TORNAI, G. and G. CSEREY (2010) "2D and 3D level-set algorithms on GPU," in *Cellular Nanoscale Networks and Their Applications (CNNA), 2010 12th International Workshop on*, pp. 1–5.

[68] YIN, G., Y. LIN, and Y. WANG (2009) "3D level set model for medical image segmentation," in *BioMedical Information Engineering, 2009. FBIE 2009. International Conference on Future*, pp. 268–271.

[69] DONG, J. and C. HAO (2009) "3D Fast Level Set Image Segmentation Based on Chan-Vese Model," in *Bioinformatics and Biomedical Engineering , 2009. ICBBE 2009. 3rd International Conference on*, pp. 1–4.

[70] MOSTOFI, H. (2009) *Fast Level Set Segmentation of Biomedical Images using Graphics Processing Unit, Tech. rep.*, Department of Engineering Science, University of Oxford.

[71] STOCKMAN, G. and L. G. SHAPIRO (2001) *Computer Vision*, 1st ed., Prentice Hall PTR, Upper Saddle River, NJ, USA.

[72] WU, P., H. LV, and S. SHEN (2011) "Research Based on Edge Feature Detection in Computer Image Processing," in *Information and Automation* (L. Qi, ed.), vol. 86 of *Communications in Computer and Information Science*, Springer Berlin Heidelberg, pp. 58–62.
URL http://dx.doi.org/10.1007/978-3-642-19853-3_8

[73] Feeman, T. G. (2010) *The Mathematics of Medical Imaging : A Beginner's Guide*, Springer Undergraduate Texts in Mathematics and Technology, Springer, New York.
URL http://opac.inria.fr/record=b1130577

[74] Hsieh, J. (2009) *Computed Tomography Principles, Design, Artifacts, and Recent Advances*, 2nd ed., Wiley Interscience SPIE Press, Hoboken, N.J. Bellingham, Wash.

[75] Barrett, J. F. and N. Keat (2004) "Artifacts in CT: Recognition and Avoidance1," *Radiographics*, **24**(6), pp. 1679–1691, http://radiographics.rsna.org/content/24/6/1679.full.pdf+html.
URL http://radiographics.rsna.org/content/24/6/1679.abstract

[76] Dougherty, G. (2011) *Medical Image Processing: Techniques and Applications*, Biological and Medical Physics, Springer New York.
URL http://link.springer.com.ezaccess.libraries.psu.edu/content/pdf/10.1007/2F978-1-4419-9779-1.pdf

[77] Sonka, M. and M. J. Fitzpatrick (eds.) (2000) *Handbook of Medical Imaging Volume 2. Medical Image Processing and Analysis*, SPIE Press.

[78] Malladi, R., J. Sethian, and B. Vemuri (1995) "Shape modeling with front propagation: a level set approach," *Pattern Analysis and Machine Intelligence, IEEE Transactions on*, **17**(2), pp. 158–175.

[79] Lefohn, A. E., J. M. Kniss, C. D. Hansen, and R. T. Whitaker (2004) "A streaming narrow-band algorithm: Interactive computation and visualization of level sets," *IEEE Transactions on Visualization and Computer Graphics*, **10**, pp. 422–433.

[80] Cates, J., A. Lefohn, and R. Whitaker (2004) "GIST: an interactive, GPU-based level set segmentation tool for 3D medical images," *Medical Image Analysis*, **8**(3), pp. 217–231.

[81] Rouy, E. and A. Tourin (1992) "A Viscosity Solutions Approach to Shape-From-Shading," *SIAM Journal on Numerical Analysis*, **29**(3), pp. 867–884, http://epubs.siam.org/doi/pdf/10.1137/0729053.
URL http://epubs.siam.org/doi/abs/10.1137/0729053

[82] T., R. and X. Xue (2001) "Variable-conductance, level-set curvature for image denoising." in *ICIP (3)*, pp. 142–145.
URL http://dblp.uni-trier.de/db/conf/icip/icip2001-3.html#WhitakerX01

[83] FAULKNER, K. and B. M. MOORES (1985) "Variations in measured computed tomography number values," *Radiography*, **51**(597), pp. 163–167.

[84] YOO, S., J. KEY, and K. CHOI (2006) "3D Visualization for Tele-medical Diagnosis," in *Computational Science and Its Applications - ICCSA 2006* (M. Gavrilova, O. Gervasi, V. Kumar, C. Tan, D. Taniar, A. Lagan, Y. Mun, and H. Choo, eds.), vol. 3980 of *Lecture Notes in Computer Science*, Springer Berlin Heidelberg, pp. 335–343.
URL http://dx.doi.org/10.1007/11751540_36

[85] KÖNIG, A. H. and E. GRÖLLER (2001) "3D Medical Visualization: Breaking the Limits of Diagnostics and Treatment," *European Research Consortium for Informatics and Mathematics*, (44).

[86] CASELLES, V., F. CATT, T. COLL, and F. DIBOS (1993) "A geometric model for active contours in image processing," *Numerische Mathematik*, **66**(1), pp. 1–31.
URL http://dx.doi.org/10.1007/BF01385685

[87] CASELLES, V., R. KIMMEL, and G. SAPIRO (1997) "Geodesic Active Contours," *International Journal of Computer Vision*, **22**(1), pp. 61–79.
URL http://dx.doi.org/10.1023/A\%3A1007979827043

[88] KICHENASSAMY, S., A. KUMAR, P. OLVER, A. TANNENBAUM, and J. YEZZI, ANTHONY (1996) "Conformal curvature flows: From phase transitions to active vision," *Archive for Rational Mechanics and Analysis*, **134**(3), pp. 275–301.
URL http://dx.doi.org/10.1007/BF00379537

[89] SIDDIQI, K., Y. LAUZIERE, A. TANNENBAUM, and S. ZUCKER (1998) "Area and length minimizing flows for shape segmentation," *Image Processing, IEEE Transactions on*, **7**(3), pp. 433–443.

[90] HARTEN, A., B. ENGQUIST, S. OSHER, and S. R. CHAKRAVARTHY (1997) "Uniformly High Order Accurate Essentially Non-oscillatory Schemes, {III}," *Journal of Computational Physics*, **131**(1), pp. 3 – 47.
URL http://www.sciencedirect.com/science/article/pii/S0021999196956326

[91] SHU, C.-W. and S. OSHER (1988) "Efficient implementation of essentially non-oscillatory shock-capturing schemes," *Journal of Computational Physics*, **77**(2), pp. 439 – 471.
URL http://www.sciencedirect.com/science/article/pii/0021999188901775

[92] ——— (1989) "Efficient implementation of essentially non-oscillatory shock-capturing schemes, {II}," *Journal of Computational Physics*, **83**(1), pp. 32 – 78.
URL http://www.sciencedirect.com/science/article/pii/0021999189902222

[93] MIN, C. (2010) "On reinitializing level set functions," *Journal of Computational Physics*, **229**(8), pp. 2764 – 2772.
URL http://www.sciencedirect.com/science/article/pii/S0021999109007189

[94] UDUPA, J. K., V. R. LABLANC, H. SCHMIDT, C. IMIELINSKA, P. K. SAHA, G. J. GREVERA, Y. ZHUGE, L. M. CURRIE, P. MOLHOLT, and Y. JIN (2002), "Methodology for evaluating image-segmentation algorithms," .
URL http://dx.doi.org/10.1117/12.467166

[95] LIASIS, G. and S. STAVROU (2013) "Optimizing level set initialization for satellite image segmentation," in *Telecommunications (ICT), 2013 20th International Conference on*, pp. 1–5.